Photo-response of ferroelectric oxides

Halyna Volkova

université PARIS-SACLAY

NNT : 2018SACLC094

CentraleSupélec

Photo-response of ferroelectric oxides

Thèse de doctorat de l'Université Paris-Saclay
préparée à CentraleSupélec

École doctorale n°573 Interfaces : approches interdisciplinaires, fondements, applications et innovation (Interfaces)
Spécialité de doctorat : Physique

Thèse présentée et soutenue à Gif-sur-Yvette, 19 Novembre 2018, par

Halyna Volkova

Composition du Jury :

M. Doru C. Lupascu, Professeur, Universität Duisburg-Essen (Institut für Materialwissenschaft)	Président
M. Maël Guennou Dr., HdR, Luxembourg Institute of Science and Technology (Materials Research and Technology Department)	Rapporteur
Mme Florence Porcher Maître de conférences, HdR, Université Paris-Saclay (Laboratoire Léon Brillouin)	Rapporteur
M. Nicolas Chauvin Chargé de recherche, HdR, CNRS (Institut des Nanotechnologies de Lyon)	Examinateur
M. Pierre-Eymeric Janolin Professeur, CentraleSupélec (Laboratoire Structures Propriétés et Modélisation des Solides)	Directeur de thèse
Mme. Ingrid Canero-Infante Chargé de recherche, CNRS (Institut des Nanotechnologies de Lyon)	Co-Directeur de thèse
M. Brahim Dkhil Maitre de Conférences, CentraleSupélec (Laboratoire Structures Propriétés et Modélisation des Solides)	Co-Directeur de thèse

Thèse de doctorat

université PARIS-SACLAY
ÉCOLE DOCTORALE
INTERFACES
Approches Interdisciplinaires : Fondements, Applications et Innovation

Titre : Photo-réponses d'oxydes ferroélectriques

Mots clés : ferroélectriques, effets photo-induits, énergie propre

Résumé : Il y a un besoin de nouvelles technologies photovoltaïques avec une efficacité de conversion lumière-électricité augmentée, qui puissent être des alternatives aux dispositifs plus traditionnels d'efficacité limitée et couteux à base de jonctions p-n. Dans ce contexte, la recherche sur les pérovskites ferroélectriques inorganiques ouvre des possibilités pour le développement de nouvelles approches pour augmenter l'efficacité, par exemple grâce à leur aptitude à séparer les charges électriques photoexcitées par le champ électrique intrinsèque (associé à leur polarisation) qui existe dans chaque maille élémentaire de ces matériaux. Pour profiter de cet avantage, un matériau doit posséder plusieurs propriétés comme la ferroélectricité, une bande interdite d'énergie relativement petite pour pouvoir absorber la lumière et une mobilité des porteurs de charges élevée. Ici, on a synthétisé et étudié des solutions solides $Ba(Sn,Ti)O_3$, qui ont comme composants parents un ferroélectrique $BaTiO_3$ et un paraélectrique $BaSnO_3$. Les transitions de phases cristallographiques et la modification des états des dipôles sont caractérisées par les méthodes de diffraction et la spectroscopie diélectrique. La spectrométrie des photoélectrons X montre une corrélation entre l'évolution non-linéaire de la bande interdite pour les différentes compositions et entre l'évolution des charges locales dynamiques. Les propriétés optiques en température sont dominées par l'arrangement des dipôles dans les compositions ferroélectriques. Pour les autres compositions les propriétés sont plutôt guidées par les défauts. Il a été possible de déterminer les températures critiques des différents mécanismes à partir des caractérisations optiques. Dans ce système $Ba(Sn,Ti)O_3$, les propriétés optiques et le photocourant sont fortement reliés à la structure locale particulière et la nature de la liaison chimique, comme nous avons mis en évidence par la spectroscopie Raman et la spectrophotométrie photoélectronique X.

Université Paris-Saclay
Espace Technologique / Immeuble Discovery
Route de l'Orme aux Merisiers RD 128 / 91190 Saint-Aubin, France

université PARIS-SACLAY | ÉCOLE DOCTORALE INTERFACES Approches Interdisciplinaires : Fondements, Applications et Innovation

Title : Photo-response of ferroelectric oxides

Keywords : ferroelectrics, photo-induced effects, optical properties

Abstract : There is an active search for new photovoltaic technologies with improved efficiency, since the traditional p-n junctions have either the limited efficiency or the increased cost. The research on inorganic ferroelectric perovskites offers opportunities to develop new approaches and increase photovoltaic efficiency, for instance due to capability of these materials to more efficiently separate the photoexcited charges due to the existence of an internal electric field within their unit cell. To profit from this advantage, the material must combine properties like ferroelectricity, relatively small band gap and high charge mobility. In this work, we have synthesized and studied compounds from $Ba(Sn,Ti)O_3$ solid solution, having as end members ferroelectric $BaTiO_3$ and paraelectric $BaSnO_3$. Crystallographic phase transitions and changes of the polar states were characterized by diffraction techniques and dielectric spectroscopy. The non-linear evolution of the band gap for different compounds has been correlated to arise from evolution of the local dynamic charge existing in these compounds, as deduced from X-ray photoelectron spectroscopy. The temperature-dependent optical properties are dominated by polar order in ferroelectric compositions, while for the other compositions the defect-related mechanisms prevail. The critical temperatures for different mechanisms can be determined from optical characterization. In these compounds, the optical properties and photocurrent are strongly related to particularities of the local structure and chemical bonding deduced from Raman and X-ray photoelectron spectroscopies.

Université Paris-Saclay
Espace Technologique / Immeuble Discovery
Route de l'Orme aux Merisiers RD 128 / 91190 Saint-Aubin, France

Acknowledgements

I want to thank very much the members of the jury committee Doru Lupascu, Maël Guennou, Florence Porcher, et Nicolas Chauvin who agreed to come to my defence and spent time reading and correcting this manuscript, as well as for their inspiring questions which might help in the future development of this work.

I feel grateful to my thesis supervisors Brahim Dkhil and Ingrid Canero-Infante, who made me discover multiple topics and methods, and to move my scientific interests to the field of ferroelectrics, by helping me in discussions and giving me the possibility to go to multiple conferences and workshops to meet new people and learn new things. I am especially happy that I could spend two short-time visits of other laboratories, in Lyon and Barcelona, for photoluminescence and photovoltaic measurements, and I am happy that my work seems to be the beginning of several collaborative projects.

I want to thank a lot to Nicolas Chauvin from INL, Lyon for all the help with equipment and fruitful discussions, and the team of ICMAB, Barcelona (Ignasi Fina and Florencio Sanchez for project supervision, and Mateusz Scigaj for showing me the experimental details). Also I am grateful for collaboration to Jerome Guillot, Damien Lenoble from Luxembourg and Gregory Geneste from CEA, and to Carlos Frontera from ICMAB, Spain and Florence Porcher from LLB.

I thank very much to my official thesis supervisor, Pierre-Eymeric Janolin, for helping me in solving the administrative questions and except everything for his kind words which inspired me a lot in writing process.

Great thanks to all the members of SPMS laboratory, and especially to Pascale Gemeiner, Fabienne Karolak, Pavan Noukala, Christine Bogicevic, Charles Paillard, Xavier Bril, and Nicolas Guiblin for introducing me to measurements and performing a part of them. I am grateful to Christine Vinée-Jacquin, Pascale Salvini, and SPMS director Guilhem Dezanneau for nice advices, for their kind attitude to me and for being always ready to help. Finally, I thank a lot to everybody from my home laboratory SPMS for help and for creating the nice atmosphere to be here during all the time of my thesis, and for the nice moments I had in the laboratory, for instance learning plenty of new French expressions (I owe you actually starting actively speaking French!). Thanks for nice time together to Charles, Arij, Vitoria, Chen Yi, Henri, Pavan, Leo,

Rossen, who were in SPMS at the same time as me. Also thanks to everybody in ICMAB, Spain and INL Lyon, France for nice time I spent there.

Contents

Chapter 1

Introduction

1.1 Motivation: photovoltaics and ferroelectric perovskite oxides

Commercially used solar cells are based on p-n junction technology. In a single p-n junction, the efficiency of generating the current cannot reach above $\sim 30\%$. This is due to the Shockley-Queisser efficiency limit [1], which stems from the fact that the potential difference which separates the electron-hole pairs is active only close to the interface, the space charge region. In detail, the efficiency of the solar cell is the ratio of incoming light intensity to the one converted to electrical current, the numerator proportional to the product of the short-circuit current and open-circuit voltage of the p-n junction. The former factor contributes to generate more current for small band gaps, since in this case a larger portion of solar spectrum (fig. 1.1) is absorbed.

However, when the light shines in the open circuit regime, on either side from the space charge region, the separated charges produce a potential buildup (fig. 1.2) which tends to partially cancel out the effect of band bending at the space charge region and to drive the efficiency lower.

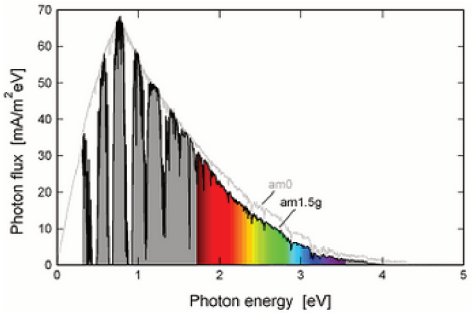

Figure 1.1: The photon flux of the AM1.5 solar spectrum

For future development of improved photovoltaic devices multiple approaches were proposed. The possibilities lie in changing the device design, for instance making multilayer solar cells, using nanowires or pyramid shape, absorber-emitter design etc. [2, 3]. To overcome the Shottky-Queisser limit, approaches to intrinsic material design were proposed, such as hot carrier generation and impact

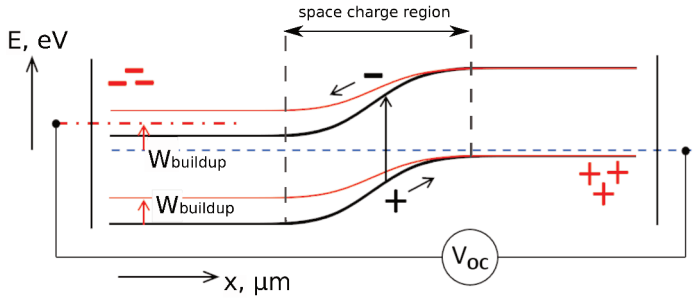

Figure 1.2: The scheme of p-n junction in open-circuit conditions under illumination, with charge buildup partially cancelling the band bending.

ionization in nanoparticles under light of above-bandgap energy [4, 5, 6, 7]. In this concept, the excess energy of the photon should be used for creation of the second exciton. Another intrinsic way to increase the efficiency in the bulk could be provided by ferroelectric materials [8]. These materials have ae non-centrosymmetric unit cell, where differently charged ions create a charge dipole and result in intrinsic polarization. In a bulk ferroelectric material under the absorbed light the charge dipole results in an intrinsic shift current, which is exhaustively explained by quantum mechanisms [9]. Despite the fact that shift current values are small ($\sim nA$), the open-circuit photovoltages should not anymore be the limiting factor for efficiency, since in this case they can exceed the bandgap multiple times [10, 11].

Organic perovskite solar cells are widely developed and can reach up to 21% efficiency (see Figure 1.3), however they have disadvantages like low stability under atmospheric conditions, or their fabrication process being harmful for the environment, as they contain halide ions (Cl, I or Br).

This PhD thesis concentrates on studying $BaTiO_3$-based inorganic ferroelectric perovskites, which are environmentally friendly, cheap to produce, and support much higher temperatures than organic compounds. The disadvantage of inorganic perovskites is their large band gaps 2.7-3.4 eV, meaning that the largest part of solar spectrum is not absorbed. The current challenge is to bring inorganic perovskites closer to applications by engineering their properties like band gap, charge conductivity and mobility, and polarization through means of chemical substitution. In this work, we concentrate on optical (light absorption) properties and the band gap modification.

In most of perovskites ABO_3, the valence band (VB) is formed by three non-bonding (valence) orbitals of the O atom (O 2p), and the conduction band (CB) is composed of non-bonding or weakly anti-bonding orbitals of the B atom (typically, B 3d). Certain hybridization is possible between B and A-site atoms in conduction band minimum (CBM), or between O and A-site in the valence band maximum (VBM), but it is normally as small as to be

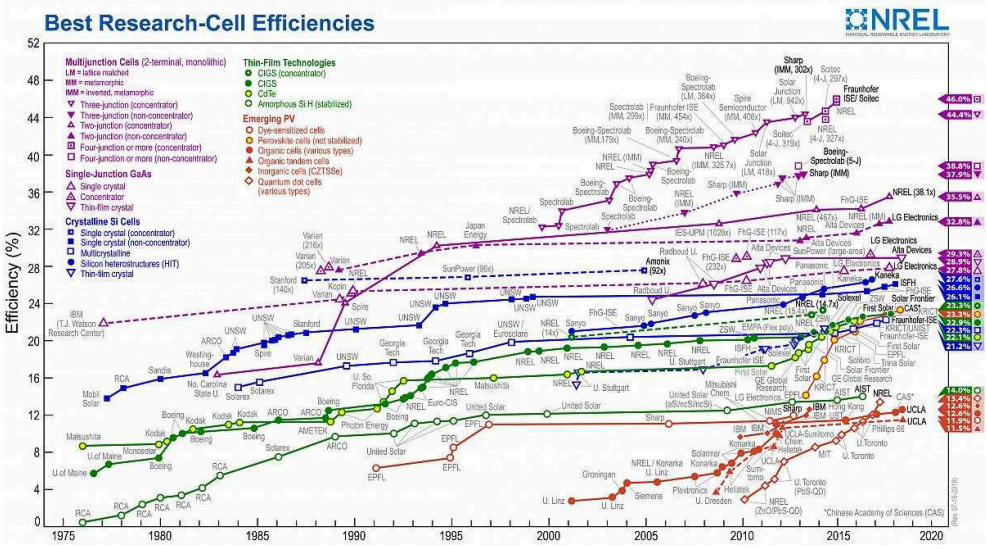

Figure 1.3: The efficiency chart of commercially patented solar cell technologies. Credits to NREL (https://www.nrel.gov/pv/national-center-for-photovoltaics.html)

neglected. Thus, the band gap is mostly determined by the qualities of the bond B-O. Based on this, it is interesting to substitute the B-site cation.

Unlike some transparent oxide double compounds (HfO_2 - ZrO_2) [12], band gap value of perovskite solid solutions often evolves strongly non-linearly. There are multiple examples of such B-site substitution. First approach is to choose the transition metal atom so that it's electronic levels will be situated inside the band gap of the parent compound. The examples are $Sr(Cr,Ti)O_{3-\delta}$ [13] where Cr^{-}_{Ti} t_2g orbitals are situated just above the valence band maximum, or $Ba(Pd,Ce,Ti)O_{3-\delta}$, where the orbitals of Pd lie both above the VBM and below CBM which is formed by Ce [14, 15], or $(K,Ba)(Ni,Nb)O_{3-\delta}$, where the band gap was reduced from 4 eV to <1.5 eV. Calculations show that significant reduction in the band gap happens due to the formation of complexes from oxygen vacancy $V_O^{\cdot\cdot}$ and adjacent Ni'''_{Nb} defects. Despite being efficient in band gap reduction, defects act as trapping and recombination centers for the photoconduction electrons, and the final photovoltaic efficiency is low (around 3%). In further works by Rappe, he calculated that charge redistribution in layered compounds with certain ordering of atoms, like $Bi(Zn_{0.5}Ti_{0.5})O_3$ [16, 17, 18] must lower the band gap without creating defects, but the synthesis of this material in pure shape is complicated, and the solid solution $0.88 \cdot BaTiO_3$ - $0.12 \cdot Bi(Zn_{0.5}Ti_{0.5})O_3$ does not show the band gap decrease for some reason [19].

The layered compounds like thin film multilayers, or Aurivillius phase materials, or Ruddlesden-Popper phases are actively studied [20, 18]. From all

the works with an accent on atomic ordering, the most successful was on Bi_2FeCrO_6 thin films [21]. There are regions of ordered superstructure inside the disordered matrix, former ones showing the decrease of band gap from 2.7 eV to 1.5 eV (by 1.2 eV), and the latter one – only by 0.5 eV. Superstructure leads to certain Jahn-Teller distortions, under which the valence of atoms changes from (Fe^{3+}, Cr $^{3+}$) towards (Fe^{2+}, Cr^{4+}). Calculations explained the drastic decrease of the band gap by effect of stress in thin films which causes the reordering of orbital directions [22]. By making a trial multilayer solar cell from Bi_2FeCrO_6 layers with different properties of ordered regions, 8% efficiency is reached, which is the highest ever made with inorganic ferroelectric and is a very promising result.

In our work, we study pure perovskite compounds $Ba^{2+}Ti^{4+}O_3^{2-}$, $Ba^{2+}Sn^{4+}O_3^{2-}$ and their solid solutions.

1.2 Crystallographic studies of Ba(Sn,Ti)O_3 phase diagram

1.2.1 $BaTiO_3$

Barium titanate, $BaTiO_3$, is a perovskite ferroelectric. Perovskites is the class of chemical compounds which have the general formula ABO_3 fig. 1.4. In the cubic unit cell the A-site atoms are located in the edges of a cube, the B atoms are in the center, and the O atoms are on the face centers and form the octahedron around the B-site atom. In $BaTiO_3$ the cubic phase is in equilibrium at high temperatures (above the Curie temperature Tc). The full phase sequence from high to low temperature is cubic (C) $Pm\bar{3}m$, tetragonal (T) $P4mm$, orthorhombic (O) $Amm2$, rhombohedral (R) $R3m$ as shown in the top panel of fig. 1.5 [23]. In T, O and R phases the Ti atom is displaced from the center of unit cell towards the crystallographic directions <001>, <110>, and <111> [24]. On cooling, the unit cell parameters a and c decrease stepwise during phase transitions. There is a phase transition hysteresis at the different temperatures at each phase transition: during cooling the phase transition starts at lower temperatures in comparison to heating. This is characteristic to first order phase transitions, like those of $BaTiO_3$. As the displacement of central Ti ion changes, the polarization varies in the way shown in the second panel of fig. 1.5. Relative permittivity also peaks at phase transitions.

The nature of the T-C phase transition is a lot discussed in the literature. Originally, it is possible to picture it as a displacive phase transition controlled by certain phonon soft mode whose frequency tends to zero at the phase transition (basically, phase transition happens in one step). However it was shown by Raman spectroscopy that the soft mode does not reach zero frequency. It turns out that there is a significant order-disorder component (different unit cells are non-equivalent). It was shown by Itoh and coworkers [26] fig. 1.6, at

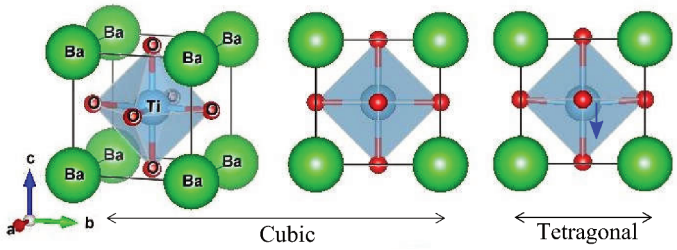

Figure 1.4: Unit cell of $BaTiO_3$ in cubic paraelectric and tetragonal ferroelectric phases

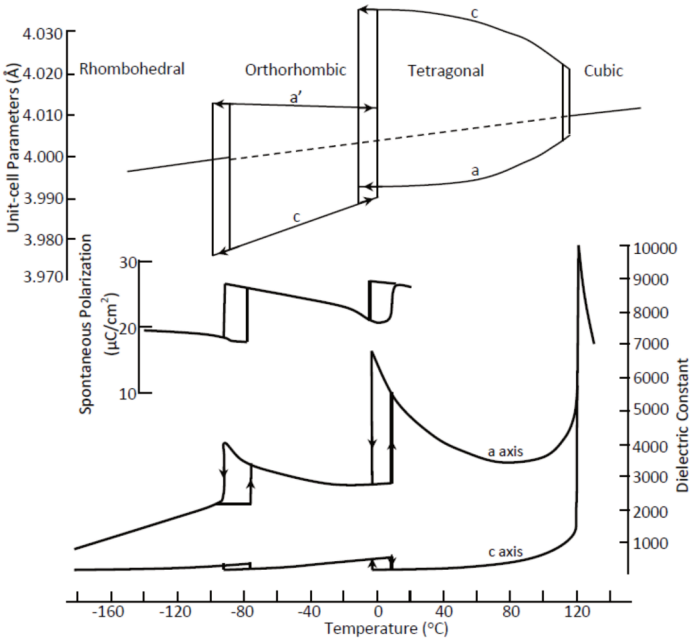

Figure 1.5: The phase transitions of $BaTiO_3$: unit cell parameters, spontaneous polarization and dielectric constant as a function of temperature, from top to bottom [25]

399 K which is 3 K above the Tc, there is a tendency to average displacement of Ti atoms towards <111>, despite normally the atoms should occupy either the displaced positions <001> or the unit cell center. Same for oxygen atoms, they form circles around the face centers. Barium is also on average displaced, and the most suitable fitting model places it in the position with twelve-fold symmetry. The displacements vanish above 450 K. This data is recorded on laboratory diffractometer with Cu Kα source of x-rays. It is probably not as reliable as synchrotron data, nevertheless it for sure comes from the bulk (micrometric probing depth) of the sample as the absorption coefficient of $BaTiO_3$ is relatively low this X-ray wavelength.

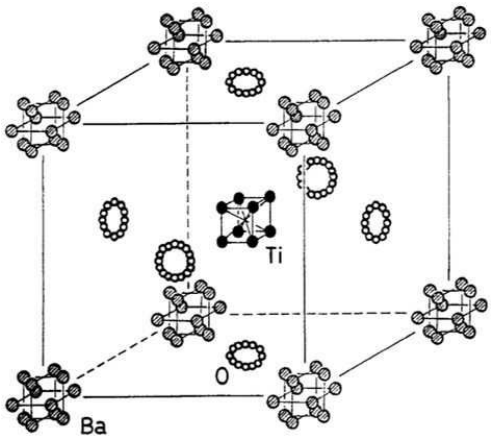

Figure 1.6: Average displacements of atoms in cubic $BaTiO_3$ 3 K above Tc deduced from refinement of XRD data [26]

The nature of other two transitions has lately been questioned. In [23] under very slow cooling the XRD peak appears which does not belong either to O or T phase fig. 1.7a. This phase is most probably monoclinic. Monoclinic phase was before discovered in PZT [27], despite according to theoretical sixths-order expansion of free energy it should not occur [24]. However, after 8-order expansion monoclinic phase appears to exist. It is suggested that in classical ferroelectrics like $BaTiO_3$ and $KNbO_3$ a different sequence of phases is possible than the one usually found. Either the order R-O-M_A-T-C or R-M_B-O-M_A-T-C is possible. In addition, even the sixth-order expansion is close to predicting M_C phase [24].

1.2.2 $BaSnO_3$

$BaSnO_3$ end compound of $Ba(Sn,Ti)O_3$ solid solutions is cubic (C) $Pm\bar{3}m$ at all temperatures fig. 1.8. The slight change of slope at low temperatures (100-125 K) is caused by freezing out of atomic movements.

1.2.3 $Ba(Sn,Ti)O_3$

The Sn cation has the Shannon radius R(Sn)=0,69 in comparison to one of Ti which is smaller R(Ti)=0,605 [30]. According to this, the volume of the unit cell of $Ba(Sn,Ti)O_3$ solid solution increases on Sn substitution. There is full solubility throughout the phase diagram [31]. First two compositions, x(Sn)=0.02 and x(Sn)=0.06 preserve all the phase sequence of $BaTiO_3$, while the Ti off-centering is decreased. It is explained by Sn atoms breaking the space continuity of long-term correlations in Ti-O chains [32]. Already for x(Sn)=0.11, the phase sequence changes and there is a rhombohedral phase changing to quasi-cubic, passing close to quadruple point and then turning to

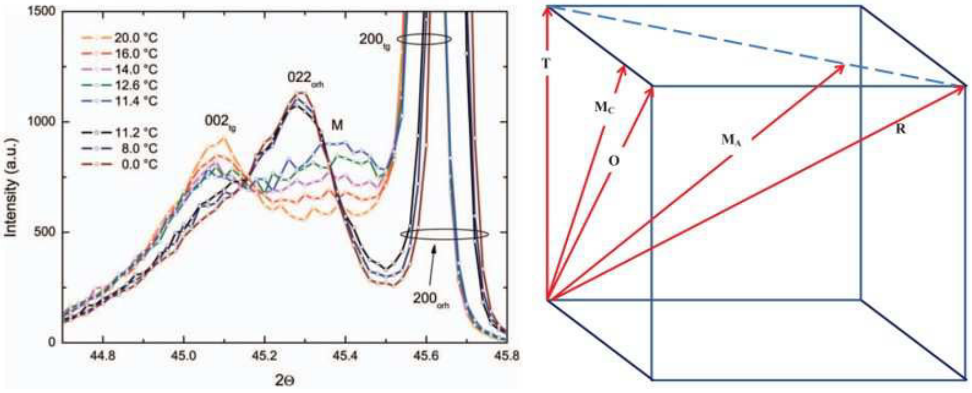

(a) (b)

Figure 1.7: Possible intermediate monoclinic phase formation at O-T phase transformation: (a) XRD diagram of $BaTiO_3$ single crystal at cooling through T-O phase transition (293-273 K, -0.05 K/min) [23] (b) possible directions of polarization inside the $BaTiO_3$ unit cell [28]

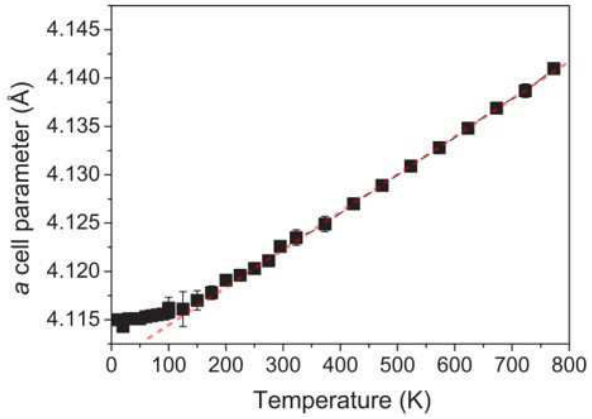

Figure 1.8: Temperature dependence of the unit cell parameter of $BaSnO_3$ [29]

cubic at much lower temperatures in comparison to $BaTiO_3$ [33]. The distortions in the quasi-cubic phase are very low and it is difficult to determine their true nature as the XRD was performed on laboratory diffractometer where the resolution is not sufficient. Because of this, the refinements of laboratory XRD data with tetragonal or cubic symmetry also give satisfactory agreement factors [34]. As the Sn ratio increases further x(Sn)>0.11, the temperature of transition between the rhombohedral phase and cubic one decreases fig. 1.9 [33].

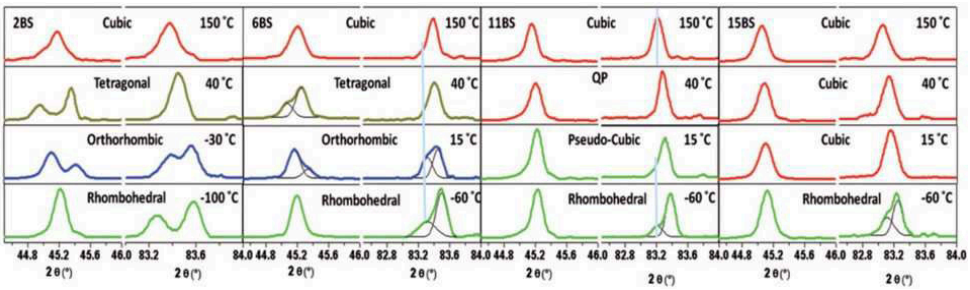

Figure 1.9: XRD patterns of Sn-rich compositions of $Ba(Sn,Ti)O_3$ at different temperatures, x(Sn)=0.02; 0.06; 0.11; 0.15 [33]

1.3 Visualizing chemical homogeneity on atomic level

The TEM allows to check the homogeneity of chemical composition. Moreover, in the High Resolution mode (HRTEM) the individual atomic displacements can be visible, averaged in each atomic column over the thickness of the sample.

Figure 1.10 shows that on the atomic scale the material is not homogeneous. The regions rich in either Ti or Sn are visible in the right panel. The Ti polar displacements in the left panel of fig. 1.10 are larger for Ti-rich regions. These regions can be called polar nanoregions (PNR). The different reaction (relaxation) of PNR impedance to AC electric field of different frequencies will be discussed in next section and is the basic property of relaxor systems.

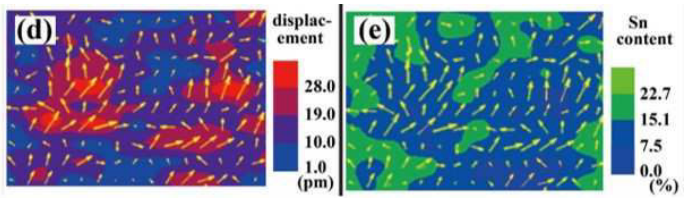

Figure 1.10: Correlation of Ti polar displacement in polar nanoregions (PNR) with Sn concentration for x(Sn)=0.2 (HAADF TEM image) in $< 001 >$ polar axis [35]

In fig. 1.11 one can see that regions with different Ti displacement start forming already in x(Sn)=0.16, despite the average Ti off-centering is very small. In x(Sn)=0.2, the difference in Ti off-centering becomes larger, but it stays similar in x(Sn)=0.25. Nevertheless, the proportion and size of PNR with larger Ti off-centering increases. The summary of approximate PNR characteristics can be seen in table 1.1. To conclude, on the local scale the Ti displacement decreases from pure $BaTiO_3$ towards x(Sn)=0.16, but it is larger for further compositions. To our knowledge, no such HRTEM studies

have been performed for x(Sn) > 0.25, for Sn-rich compositions which show well-marked relaxor behaviour.

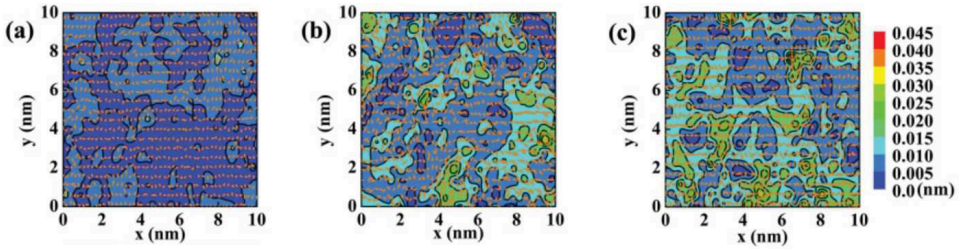

Figure 1.11: Ti displacement in compositional serie x(Sn) = 0.16; 0.2; 0.25 (HRTEM image) in <120> polar axis [36]

Table 1.1: Ti displacement in PNR and the average size of displaced regions

x(Sn)	average Ti displacement, pm	PNR average size, Å
0.16 [36]	0 - 5	40-60
0.2 [35]	10-28	16
0.2 [37]	8-22	16-24
0.2 [36]	10-20	20-30
0.25 [36]	10-20	30-40

The PNR size and shape can be analysed from the diffuse electron scattering around the diffraction points in TEM. The advantage of diffraction over imaging is that in the latter it is difficult to get the 3D information. The detailed analysis from [38] shows that the diffuse scattering in the series x(Sn)=0.10, 0.20, 0.225, 0.25, 0.30 and 0.50 comes from chains of polarized unit cells in $< 001 >$ direction, with the characteristic length of chains at least 5 nm for all these compositions. With increase in Sn ratio the diffuse component becomes weaker, which is consistent with a decrease in the number of Ti off-centered atoms as well as reduction of dielectric constant.

Other work [37] suggests that the diffuse scattering is coming from very thin ($<$ 1 nm) elliptic zones with long axis ($\sim$ 2nm) parallel to the $< 001 >$ direction.

1.4 Dipole ordering and dielectric spectroscopy

To study the transitions between different dipole orderings, dielectric spectroscopy is used. The dielectric constant $\varepsilon(\omega) = \varepsilon'(\omega) + i\varepsilon"(\omega)$ peaks at every phase transition for a ferroelectric ($1/\varepsilon$ tends to zero at the phase transition). In $BaTiO_3$, the phase transitions are (at least partially) driven by a phonon transverse soft mode, and this causes the ε to peak:

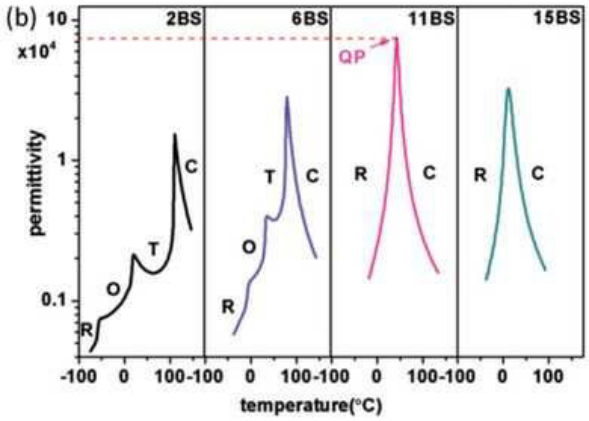

Figure 1.12: Relative permittivity of $BaSn_xTi_{1-x}O_3$ with x(Sn) = 0.02; 0.06; 0.11; 0.15 [33]

$$\frac{\omega_L^2}{\omega_T^2} = \frac{\varepsilon_{st}}{\varepsilon_\infty} \tag{1.1}$$

with ω_L and ω_T - longitudinal and transversal phonon mode frequency, ε_{st} and ε_∞ - dielectric permittivity at electric field frequency f=0 and at optical frequencies.

To our knowledge, only the Ti corner of the phase diagram was studied in dielectric spectroscopy. In fig. 1.12, one can see the ε shown for a compositional series $BaSn_xTi_{1-x}O_3$. The plot for x(Sn)=0.02 has the peaks which are inherent to $BaTiO_3$. On further increase of Sn ratio, the transition temperatures T_1, T_2 and $T_3 = T_m$ (temperature of peak maximum) get closer to each other, so that for x(Sn) = 0.11 there is only one peak with the temperature of maximum Tm. For x(Sn) > 0.11 the Tm is decreasing. In this compositional range the dielectric permittivity value peaks for x(Sn)=0.11. As can be seen from fig. 1.13, this is the composition close to the so-called quadruple point where four different kinds of unit cell distortion are allowed to coexist. The fact that Ti can be easily displaced to multiple directions also causes the anomaly of the piezo-electric [33, 28] and electrocaloric [39, 40, 40, 41] properties, and the mechanical compliance to happen at this temperature. [42].

As shown in fig. 1.13, $BaTiO_3$ the Tm equals the Curie temperature T_{CW}, but for compositions x(Sn)>0.1 dielectric permittivity peaks become wider as characteristic of diffuse phase transition. For diffuse phase transition $1/\varepsilon$ does not tend to zero, so more characteristic temperatures are needed to describe the phase transition. Those parameters are Tm - dielectric peak maximum, T_{CW} - the Curie-Weiss temperature, and T_Q. The T_{CW} is determined from fit of data to equation

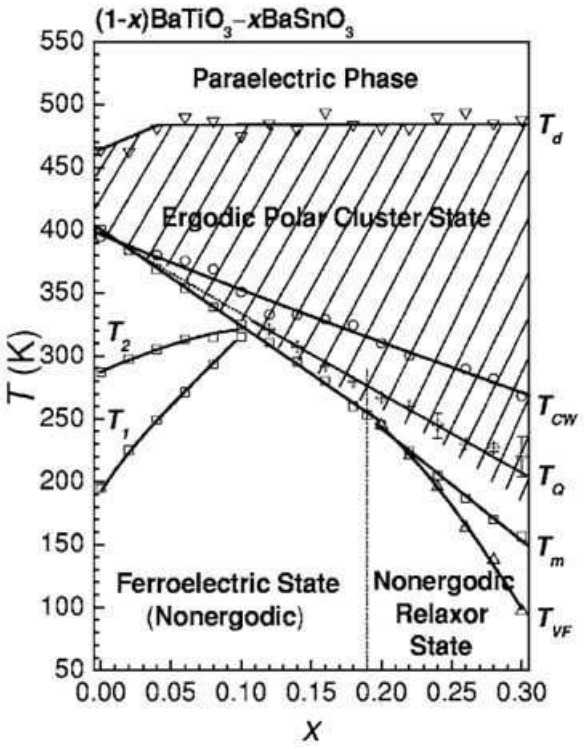

Figure 1.13: Phase diagram of $BaSn_xTi_{1-x}O_3$, x(Sn)=0...0.3 from dielectric spectroscopy [43]

$$\varepsilon' = \varepsilon_0 + \frac{C}{T - T_{CW}} \tag{1.2}$$

with C - Curie constant, ε_0 - frequency-dependent and temperature non-dependent contributions (high-energy phonon modes or electronic polarization).

The Td - temperature where the static polar correlations disappear (same as T_B - Burns temperature) is determined as the temperature below which the data of cubic phase deviates from the Curie-Weiss law. This signifies that on heating through this point the polar correlated regions disappear.

Just above the Tm, the fit can be done with equation

$$\frac{\varepsilon_A}{\varepsilon} = 1 + \frac{(T - T_A)^2}{2\delta^2} \tag{1.3}$$

with ε_A, T_A, δ - the parameters. In fig. 1.13, the temperature T_Q is where the deviation from eq. (1.3) appears and the data begins to change towards the Curie-Weiss law.

The low-temperature phase is rhombohedral ferroelectric for low Sn ratio, and changes to polar glass frozen relaxor state for higher Sn ratio. The freezing temperature T_{VF} is determined from the fit by the Vogel-Fulcher law:

$$f = f_0 \cdot e^{\frac{-E_a}{k(T_m - T_{VF})}} \tag{1.4}$$

with f_0 - the characteristic frequency of PNR dielectric relaxation, and E_a - the activation energy.

Whether the ferroelectric low-temperature phase changes to the relaxor one abruptly in the compositional series was discussed in several references. Authors of ref. [43] found a sharp transition at x(Sn)=0.2 from the analysis of ε' asymmetric peak widths. However, ref. [44] claims that the transition is continuous. Figure 1.14 shows the dependence of an imaginary part of dielectric permittivity ε" on frequency. It shows how the energy of applied electric field is absorbed by the sample (dielectric loss), and is used to analyse processes of dielectric relaxation. For compositions x(Sn)=0.15 and 0.175 there are two relaxation processes, attributed to breathing modes of pinned domain walls and PNRs. In the latter composition, there is at the same time the high-frequency relaxation (10^8-10^9), which is usually attributed to reorientation of PNR [44]. This work claims that the gradual transition towards the classical relaxor regime occurs for x(Sn) = 0.175...0.25, since the dynamics freezing (disappearance of high-frequency peak) occurs much below the characteristic temperature of the diffuse phase transition determined from data fit [44]. The first sample showing truly relaxor behaviour is x(Sn)=0.3.

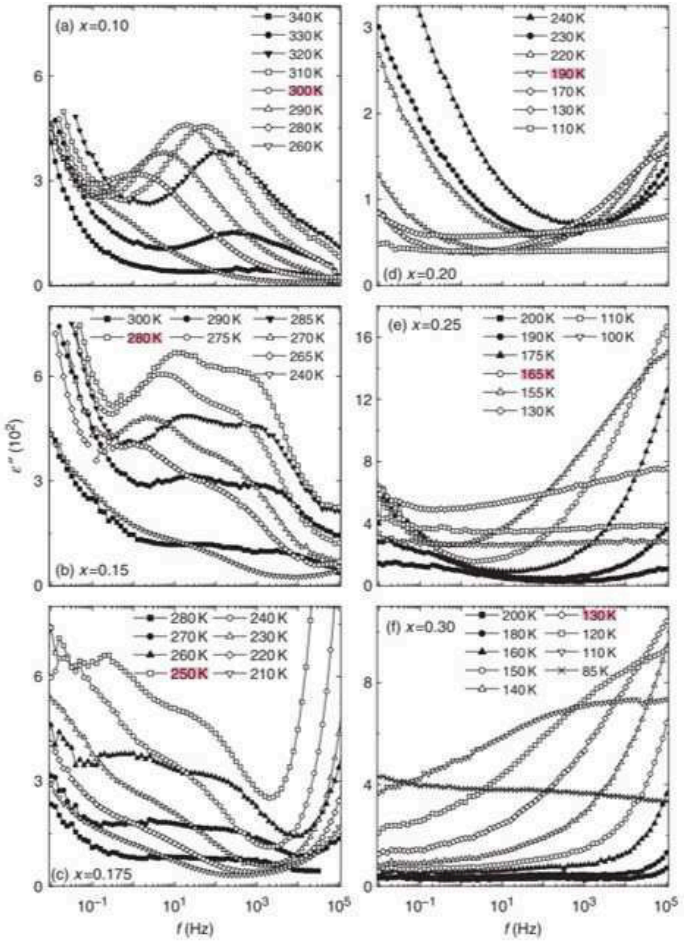

Figure 1.14: Imaginary part of dielectric permittivity of $BaSn_xTi_{1-x}O_3$ with x(Sn) = 0.1; 0.15; 0.75; 0.2; 0.25; 0.3 [44]

1.5 Macroscopic polarization

Since there is a diffuse transition to relaxor regime, it is possible to measure the remanent ferroelectric polarization hysteresis for intermediate compositions x(Sn)=0.1...0.3 fig. 1.15. Under 10 kV/cm, at room temperature there seems to be a polarization of $\sim$ 10, 9, 6, 4 $\mu C/cm^2$ for the corresponding nominal compositions 0.1; 0.12; 0.15; 0.18 [39]. Note that in ref. [39], the maximum value of dielectric permittivity is for composition x(Sn)=0.15 against x(Sn)$\approx$0.11 which is a reproducible value from other articles. So the x(Sn)=0.18 might correspond in reality to a lower Sn ratio.

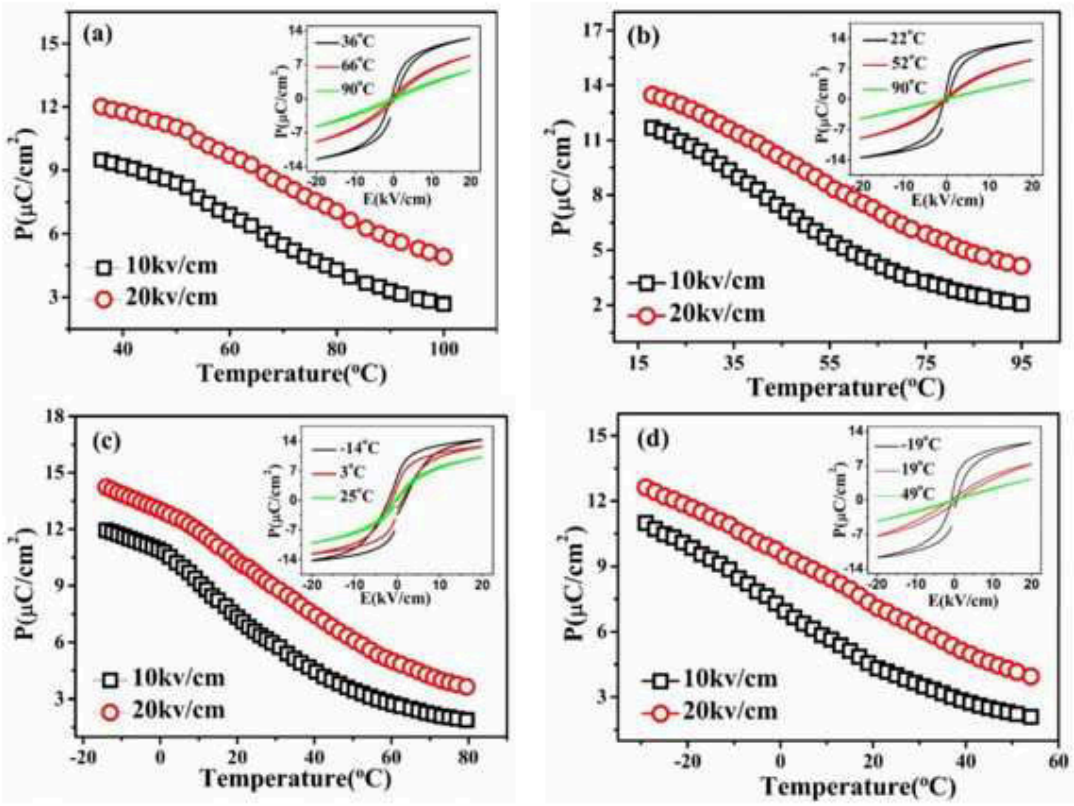

Figure 1.15: Polarization dependence on temperature and (insets) P-E hysteresis loops at different temperatures, x(Sn) = (a) 0.1 (b) 0.12 (c) 0.15 (d) 0.18 [39]

Chapter 2

New phase diagram (structure and dielectric/ferroelectric properties)

In this chapter we will describe the phase transitions of our samples depending on chemical composition and on temperature and compare the solid solutions to the pure compounds $BaTiO_3$ and $BaSnO_3$. The following sections will describe the fabrication of our samples and the study of average unit cell and ferroelectricity by X-ray diffraction, transmission electron microscopy, dielectric spectroscopy, and polarization measurement.

2.1 Methods of characterization used in this chapter

Solid state reaction synthesis implies mixing the initial chemical components in the shape of solid powders, and heating to high temperatures for chemical reaction to occur. In our case, to obtain $BaSn_xTi_{1-x}O_3$ solid solutions, we prepared the mixture according to chemical reaction:

$$BaCO_3 + (1-x)TiO_2 + xSnO_2 = BaSn_xTi_{1-x}O_3 + CO_2(gas) \qquad (2.1)$$

The speed of solid state reaction and the homogenisation of products during solid state reaction are limited by the size of the powder particles and temperature. In fact, it was shown that there are several intermediate steps to the process as shown in fig. 2.1 for pure $BaSnO_3$. First, $BaSnO_3$ crust forms on SnO_2. On second step, the process is diffusion-guided, since the Sn and O atoms should be passing through the $BaSnO_3$ layer which is formed already, and so the Sn deficient phase might be forming on top of the grain. Finally, after sufficient homogenisation at high temperatures and during sufficient time, a $BaSnO_3$ particle is formed.

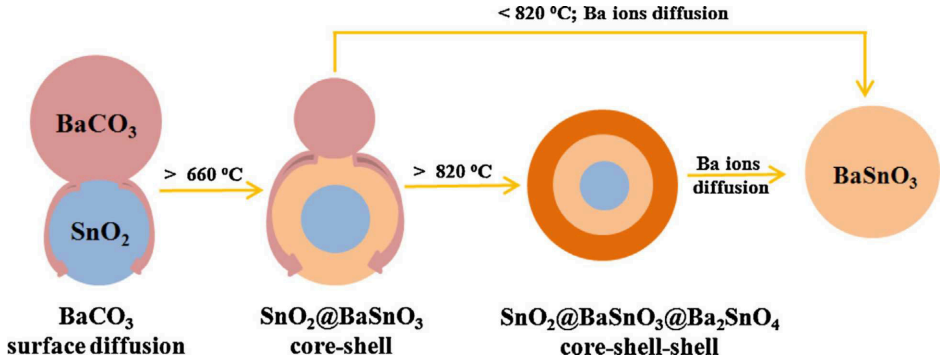

Figure 2.1: Steps of solid state reaction synthesis of $BaSnO_3$

Despite normally the processing conditions favor phase homogeneity, it is important to understand that some small difference in chemical composition or the amount of defects are possible between the grain bulk and the surface. The state of the grain surface can be further changed by annealing at $500°C$, since this is the temperature at which depending on the atmosphere either the loss of oxygen or the oxygen vacancy compensation happens [45].

The compositions of $BaSn_xTi_{1-x}O_3$ chosen throughout the phase diagram were x = 0, 0.1, 0.2, 0.4, 0.5, 0.6, 0.8, 0.9, 1. We took as initial components $BaCO_3$ (STREM 99,9% ref 56-1020 lot 21556500), TiO_2 (99% prolabo 20732,298 lot 80170), SnO_2 (99,9 % alfa products 87779 lot 00090410).

The following procedure was used to use the proper homogeneity:
(a) mixing in a mortar, and then in ethanol with magnetic mixing
(b) drying at 80°C, mixing in a mortar by hand
(c) calcination at 800°C, mixing in a mortar
(d) calcination at 1280°C, mixing in a mortar
Some samples which will be mentioned are studied after this step. For some other methods, however, additional steps of fabrication are needed, as follows:
(e) making pellets with PVA as a binding agent and sintering at 1280-1400°C, polishing the pellets with SiC papers of grade P800 (26 μm) and P1200 (15.3 μm)
(f) grinding the pellets and annealing the powders in order to remove the mechanical stresses at 500°C.

2.1.1 Details of XRD measurement in this study

The X-ray diffraction (XRD) was performed on Bruker D2 phaser diffractometer in Cu $K\alpha_{1,2}$ X-rays on finely ground and annealed powders. For solid solution samples, the acquisition times per step were of 10 seconds for 2Θ=20-35°, 30 seconds for 2Θ=35-60°, 55 seconds for 60-120° with a step of 0.02°. After the normalization of acquisition time and standard deviation, Jana2006

software for Rietveld refinement was used to obtain the composition and lattice parameters.

2.1.2 Dielectric spectroscopy measurement

The measurement was made on two kinds of ceramic pellets, sintered without any binding agent and with PVA. The silver paste contacts were deposited on the former ones, and the Cr/Au sputtering was performed on the second series. Note that for Sn-rich compositions around x(Sn)=0.8-1 the dark-colored layer of Cr-containing solid solution was formed at the contact interface with the sample, which agrees with Cr solubility in the perovskite structure, including the Sn-containing ones [46]. Therefore, x(Sn)=0.8 with golden contacts was not measured. The measurement was performed in the cryofurnace in the temperature range 78-450 K, the temperature controlled with the help of PT100 probe. The impedancemeter HP4294 was used.

2.2 Results

2.2.1 Microstructure from scanning electron microscopy

Scanning electron microscopy was performed on the powders after chemical synthesis fig. 2.2 and on the pellets sintered with PVA binding agent fig. 2.3 using the microscope model Leo Gemini 1530 with field emission gun and in high resolution mode. The grains have faceted shape and even show the growth spirals fig. 2.2d, which in general shows that they are well crystalline. The grain size varies within one composition, but on average the value is 1-2 μm throughout the compositional series. The larger grains occur rarely with longer dimension reaching about 10 μm fig. 2.2c.

When sintered with PVA, high densities ρ_{pellet} are reached (92-95 %) as determined from weighting it in water and in air:

$$\rho_{pellet} = \frac{m_{air}\rho_{water}}{m_{air} - m_{water}} \tag{2.2}$$

Correspondingly, during the sintering process the grain size increases to 5-10 μm in x(Sn)=0 and 0.2, and to 20 μm for x(Sn)=0.5.

2.2.2 Room temperature structure of compositional series

The X-ray diffraction in fig. 2.4 shows characteristic patterns of pure perovskite compounds. No parasitic peaks are found with the laboratory source. The intensity of the peaks evolves gradually throughout all compositions. The XRD peak at 45.5 ° (fig. 2.5a) consists of two components for $BaTiO_3$ in $P4mm$ space group, (200) and (002). For x(Sn)=0.1, the two components merge into one, but the shape of the peak is very wide hinting that the distortion is still present. For the rest of the compositions, the peak is quasicubic. Spectra were

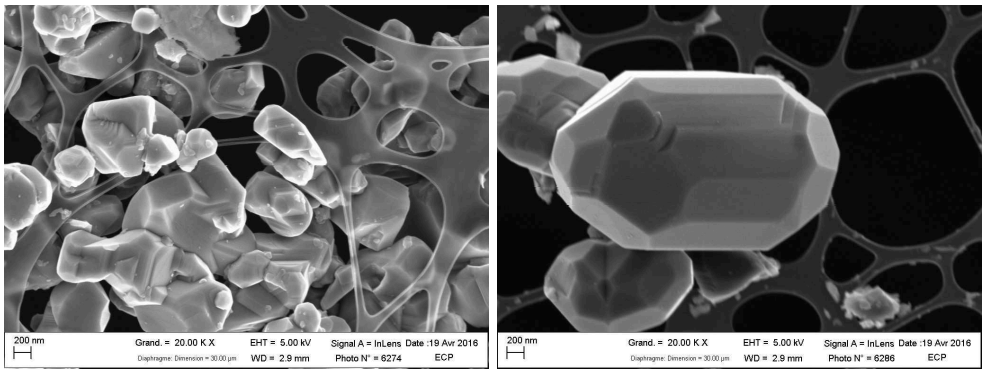

(a) (b)

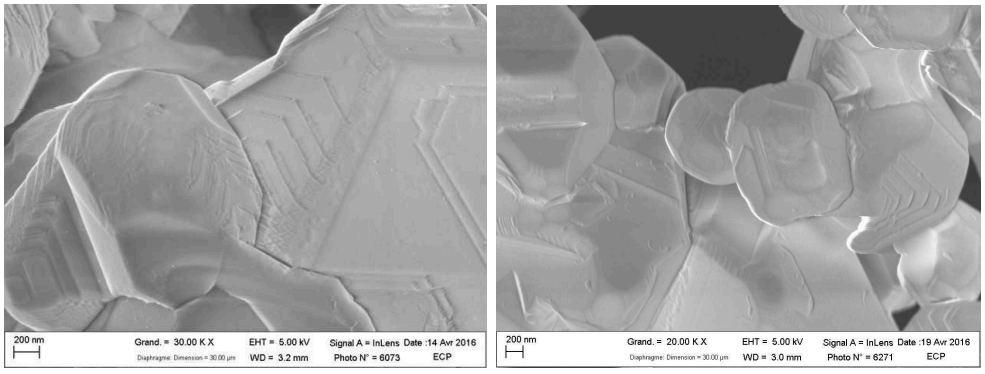

(c) (d)

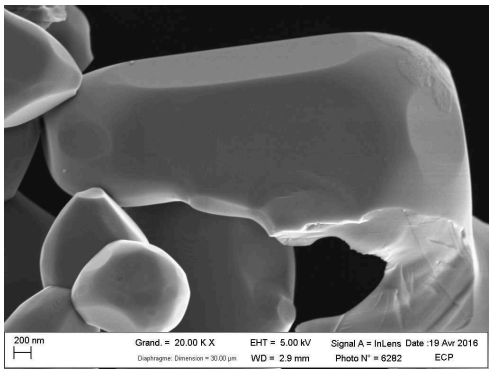

(e)

Figure 2.2: SEM (secondary electrons mode) images of $BaSn_xTi_{1-x}O_3$ powder coming from grinding the pellets of x(Sn) = (a) 0, (b) 0.2, (c) 0.5, (d) 0.8, (e) 1

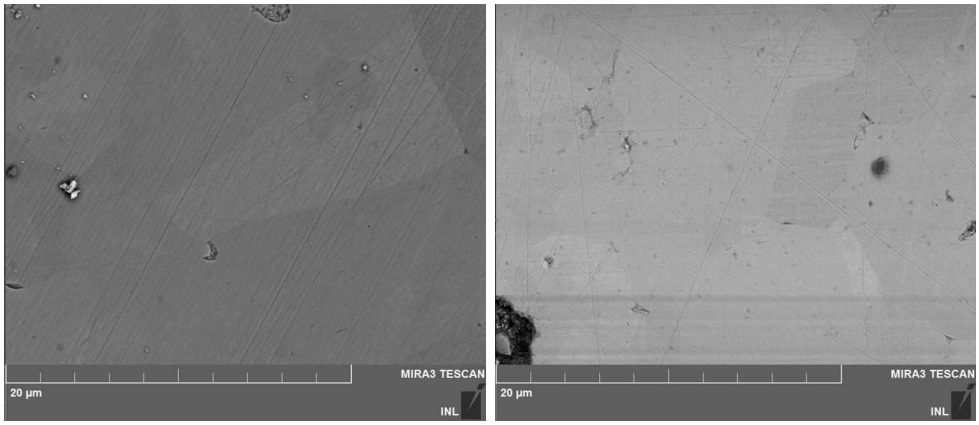

(a) (b)

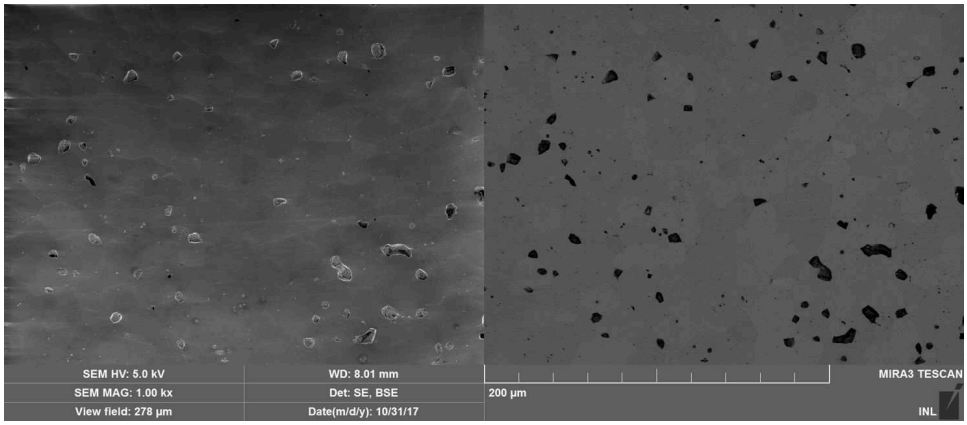

(c)

Figure 2.3: SEM images of $BaSn_xTi_{1-x}O_3$ sintered pellet with x(Sn) = (a) 0, (b) 0.2, (c) 0.5. The individual grains are visible due to the difference electron intensity for different cristalline orientation. Images for x(Sn) = 0 and 0.2 and image on the right for x(Sn)=0.5 are made in backscattered electron mode, and image on the left for x(Sn)=0.5 is made in secondary electron mode.

analysed by LeBail fit to determine the unit cell volume (fig. 2.5b). The details of the fit can be found in Annex D in fig. D1 - fig. D2 and in table D1. The value increases linearly as expected due to the larger size of the Sn ion.

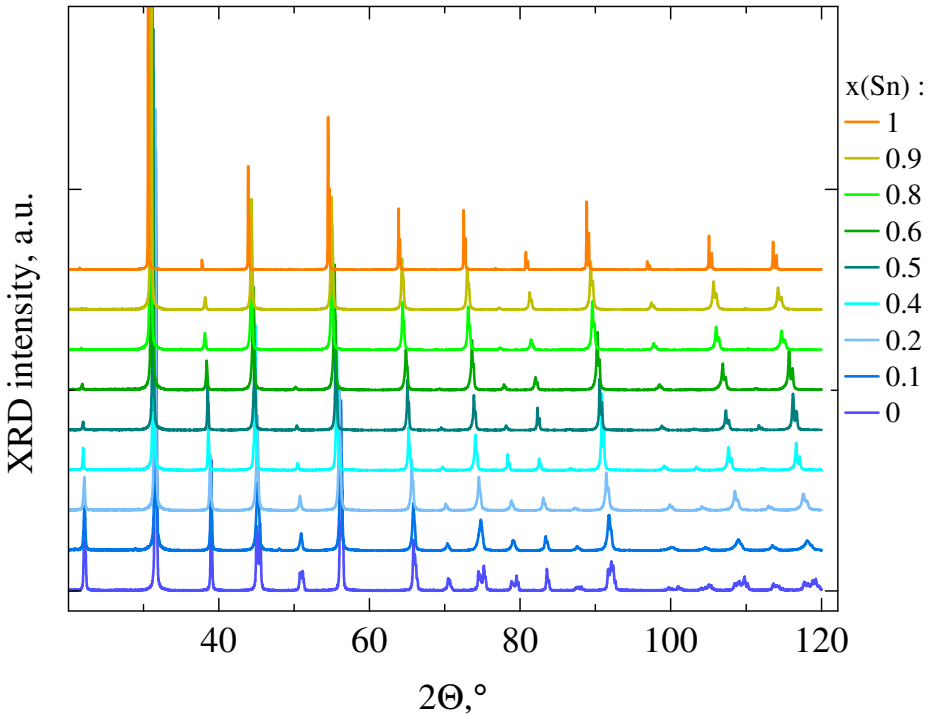

Figure 2.4: XRD patterns for different compositions of $BaSn_xTi_{1-x}O_3$: x(Sn)=0...1 (bottom towards top)

2.2.3 Dielectric spectroscopy

For the analysis of the dielectric spectroscopy data, we have applied the precedently described concepts of Vogel-Fulcher temperature T_{VF}, maximum temperature Tm, temperature of deviation from quadratic law T_Q and shift to Curie-Weiss law, Curie-Weiss temperature T_{CW}, and temperature of deviation from Curie-Weiss law which Td section 1.4.

Here, we analyse the dielectric properties of the relaxor compositions in the $BaSn_xTi_{1-x}O_3$ system for x(Sn)>0.3, as well as verify the properties of x(Sn)<0.3 which have been studied before [43, 44].

For all the compositions in fig. 2.6 we see the single dielectric permittivity peak for single frequency. In x(Sn)=0.1 and 0.2 there in no frequency dependence of the peak, the compositions with higher Sn ratio and up to x(Sn)=0.8 all show the relaxor peak shift. The corresponding Tm of dielectric permittivity at 1 MHz is given in table 2.1 and later recalled in fig. 2.10.

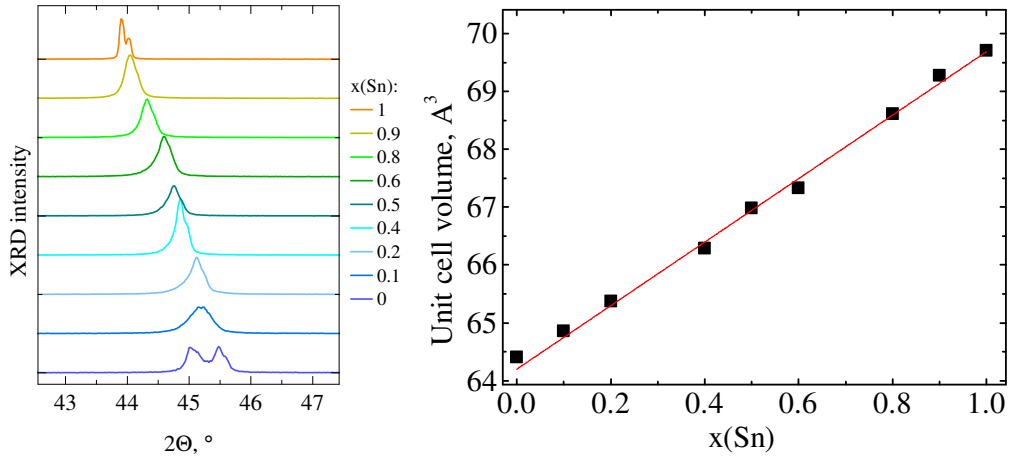

(a) (b)

Figure 2.5: Details of XRD data and results: (a) zoom at the region of (002) and (200) peaks, (b) the extracted unit cell volume (error bars of the Le Bail fit in green are smaller than the symbol size)

Table 2.1: Tm of dielectric permittivity at 1 MHz

x(Sn)	Tm, K
0.1	320
0.2	245
0.4	118
0.5	99
0.8	109

The Tm decreases first linearly for compositions until x(Sn)=0.4, and then for the remaining two compositions stays very close to 100 K. From fig. 2.7 it is visible that on frequency the Tm decreases with approximately similar rate for x(Sn)=0.4 and 0.8 and faster for x(Sn)=0.5. The higher the Sn ratio, the stronger is the shift of the imaginary part ε" to lower temperatures from Tm. According to this, the T_{VF} should be low. The results of fit by Vogel-Fucher law are shown in fig. 2.7, and T_{VF} among other results of fitting can be found in fig. 2.10.

Figure 2.8 illustrates the fit of $1/\varepsilon'$ by Curie-Weiss and quadratic laws for x(Sn)=0.4 and the determination of Td and T_Q correspondingly. Note that for x(Sn)=0.4 the Curie-Weiss law well fits the data to the highest measured temperatures, while for the further compositions x(Sn)=0.5 and 0.8 in fig. 2.8 there is a deviation at high temperatures, which normally should not occur unless some dipoles of non-ferroelectric nature are present [47]. In Sn-rich samples those could be the charged defects. The temperature above which

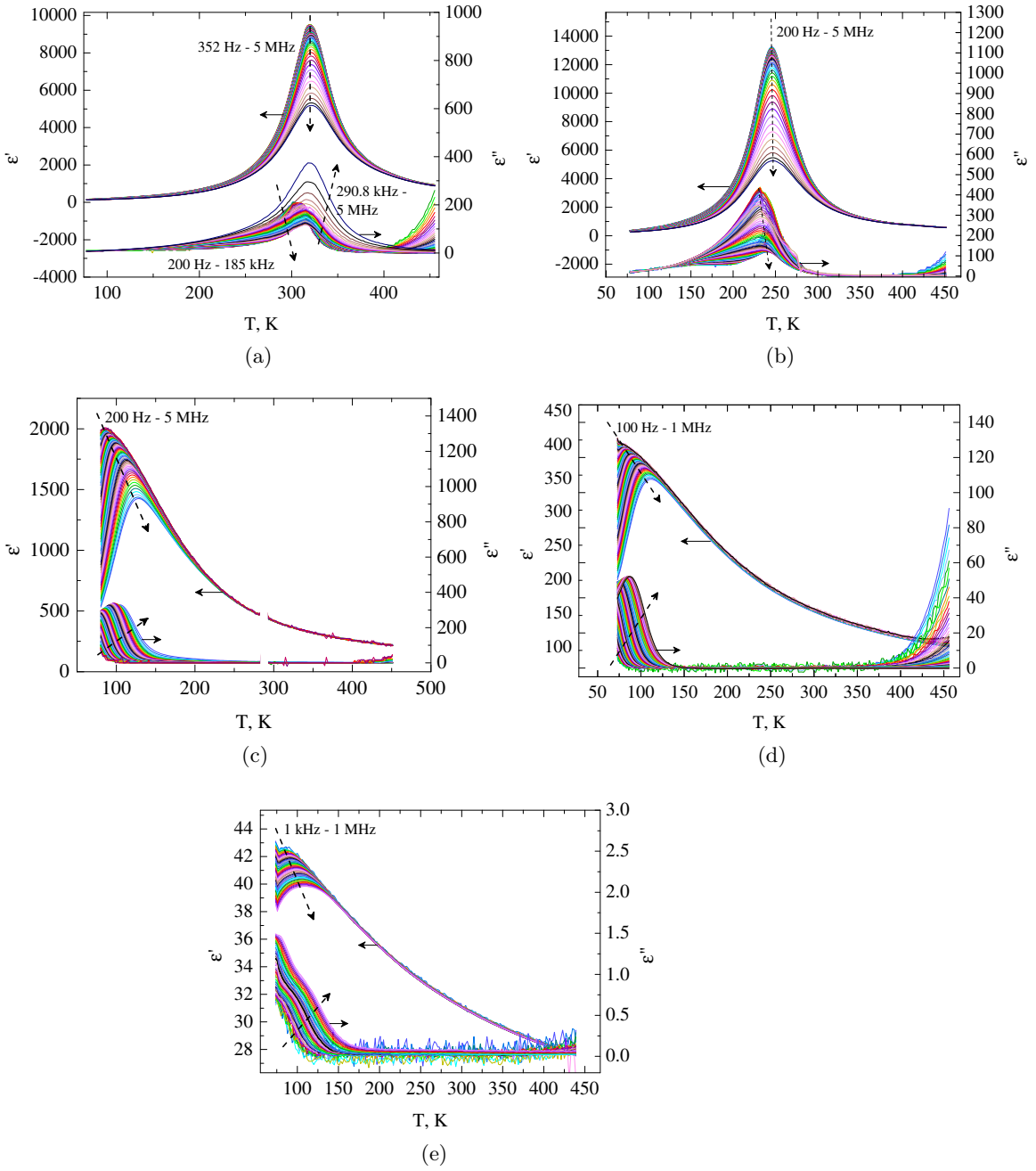

Figure 2.6: Dielectric permittivity and losses for $BaSn_xTi_{1-x}O_3$ with x(Sn): (a) 0.1, (b) 0.2, (c) 0.4, (d) 0.5 (synthesis with PVA) and (e) 0.8 (synthesis without PVA)

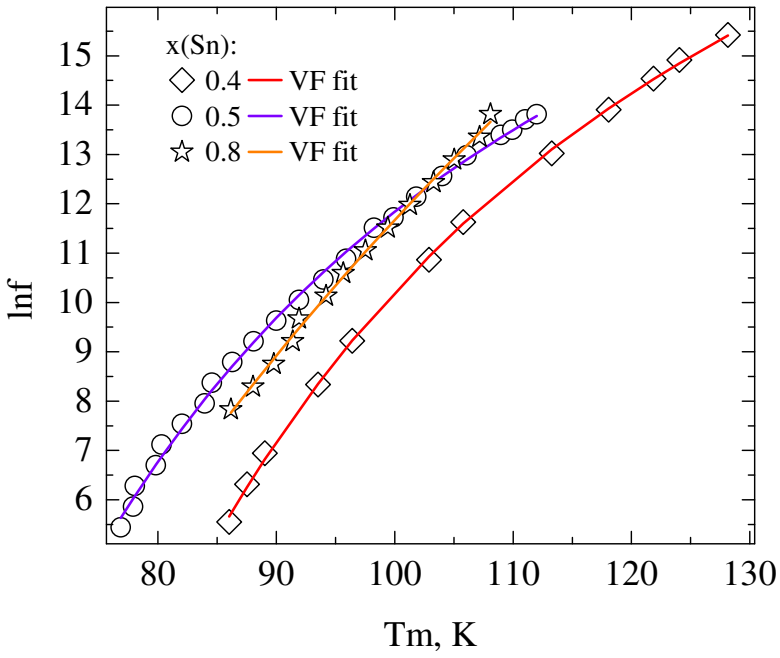

Figure 2.7: Vogel-Fulcher fit of frequency - Tm dependence for relaxor phase

the deviation occurs in fig. 2.8 is marked as Tx. We include in fig. 2.9 the procedure to determine the deviation temperature from the Curie-Weiss law for two relaxor compositions.

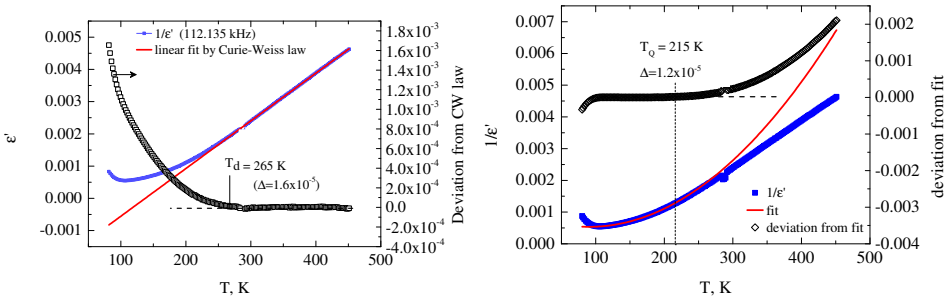

Figure 2.8: The phase transformations of $BaSn_{0.4}Ti_{0.6}O_3$ at the higher-temperature limit: (a) the fit of $1/\varepsilon$ by Curie-Weiss law and the determination of Td (b) fit of $1/\varepsilon$ by quadratic law and the determination of T_Q

Figure 2.10 presents the summary plot with the critical temperatures taken from literature and obtained in this study. Note that Td keeps approximately constant to x(Sn)=0.3 and then decreases exponentially. Similarly, the slope of T_{CW} changes at x(Sn)=0.3: this value is larger for relaxor compositions.

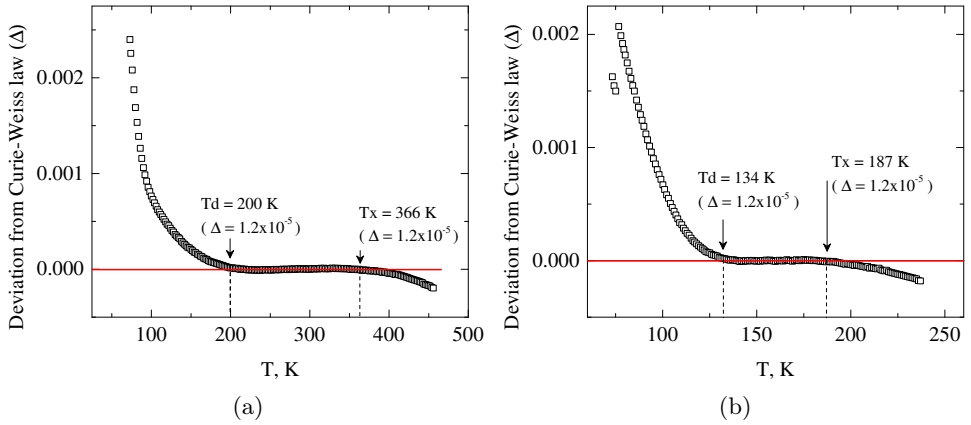

Figure 2.9: Deviation from Curie-Weiss law plotted for x(Sn) = (a) 0.5 (b) 0.8

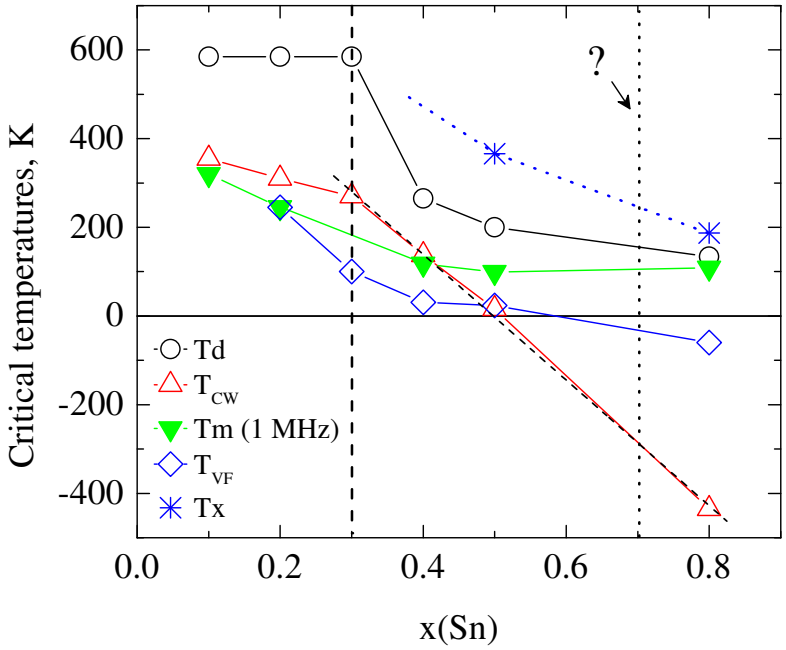

Figure 2.10: The compositional evolution of T_B, T_{CW}, Tm, T_{VF} (the data for x(Sn)<0.3 except the Tm is taken from ref. [43])

The Tm and T_{VF} decrease non-linearly. It is as low as 30.8 K and 23.6 K for x(Sn)=0.4 and 0.5, and it shifts to negative values for x(Sn)=0.8. This means that there is no polar glass state for any temperature in that composition, that the low-temperature behaviour is dominated by quantum fluctuations and is characteristic for chemical compositions in $BaTiO_3$-based relaxors above the percolation point of Ti [47].

Figure 2.11-fig. 2.15 represent the imaginary part of dielectric permittivity, which is responsible for losses, or energy absorbed as a result of some relaxation processes. For x(Sn)=0.1 there are two relaxations in mid-frequency region(fig. 2.11). The low-frequency relaxation in the sample sintered without PVA peaks at f_{max}=10^4 Hz and T=310 K, the high-frequency relaxation peaks at f_{max}=10^5 Hz and T=350 K. The region 310-350 K is where Tm and T_{CW} occurs. For the pellet sintered with PVA the difference in f_{max} between the two peaks is larger (6.9 kHz and $\sim$ 2 MHz), but the difference in temperature is smaller (309 K and 315 K). The presence of two different relaxations is in agreement with [44] and the coexistence of ferroelectric domain wall relaxation and PNR breathing mode. The relaxation characteristics might be changing between two samples because the first one has higher porosity, which is accompanied either by formation of oxygen vacancies or worse homogenisation). Note that the maximum of the loss data shifts to lower temperatures for lower frequencies.

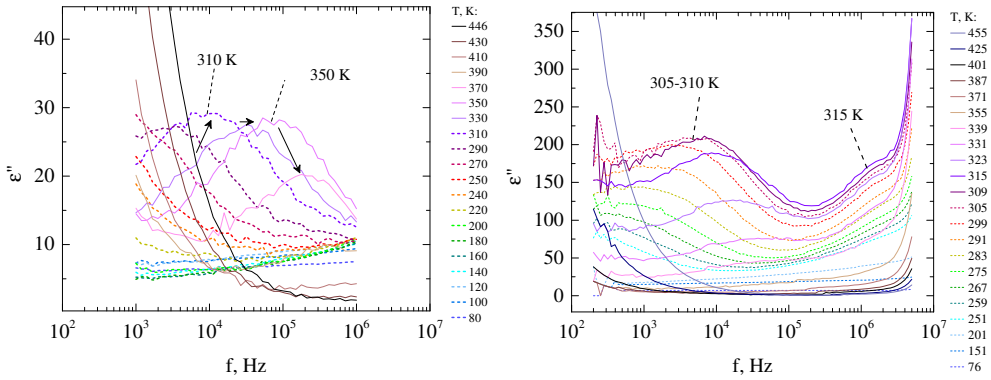

Figure 2.11: The dielectric relaxation frequency dependence for two samples of x(Sn)=0.1: the pellet sintered (a) without PVA (b) with PVA

In composition x(Sn)=0.2 (fig. 2.12), to the contrary from the previous case, the low-temperature relaxation happens at higher frequencies. For the sample without PVA, on heating the first relaxation, with maximum value higher than the frequency range of experiment, is the strongest of all relaxation processes in this sample and happens at 210 K. In the region of temperatures 240-260 K the second relaxation appears with maximum below studied frequency range, and then fades at higher temperatures. In the sample with PVA, there is a similar sequence of relaxations. First one peaks at T=210 K f_{max}=10^6 Hz, slightly larger than in x(Sn)=0.1. Second one peaks at very low frequencies at T=245 K. The second of two peaks seems to correspond to Tm, but the origin of the first one is questionable.

This different behaviour of the dielectric relaxation may be due to phase

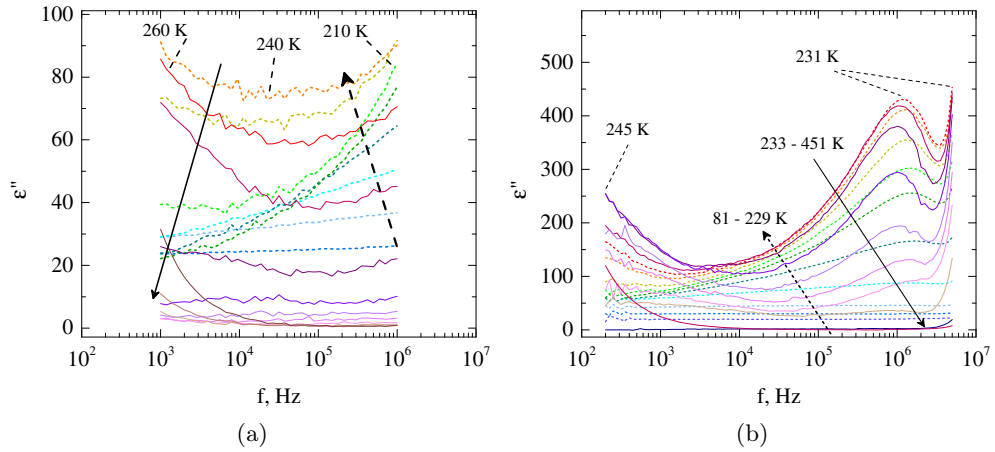

Figure 2.12: The dielectric relaxation frequency dependence for two samples of x(Sn)=0.2: the pellet sintered (a) without PVA (b) with PVA

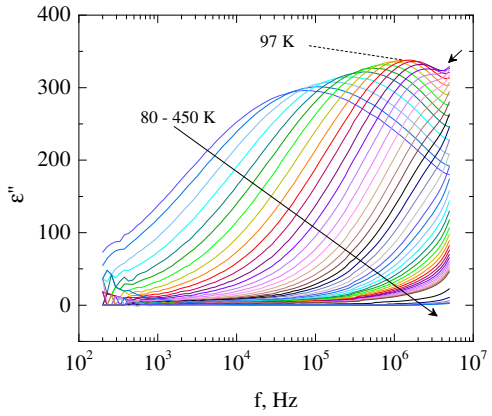

Figure 2.13: The dielectric relaxation frequency dependence for x(Sn)=0.4 sintered with PVA

coexistence, either extrinsic or due to diffuse phase transition. This topic is detailed in section section 2.2.5 and section 4.2.1.3.

In the pellet of x(Sn)=0.4 (fig. 2.13), sintered with PVA, the wide peak appears at 97 K and f_{max}=1.1·10^6 Hz, which is just below the Tm=118 K. It is visible that there is one more peak at even higher frequencies, which probably belongs to reorientation of dipoles in PNRs [44].

Overall, the behaviour of relaxation in x(Sn)=0.4 and 0.5 is very similar, together with that of x(Sn)=0.8. The first difference to notice is that in the latter sample the peak seems to be shifted to large frequencies. In x(Sn)=0.5 for both samples the maximum of relaxation lies at 778.2 kHz and 86 K. For x(Sn)=0.8 the temperature range of measurement with liquid nitrogen is above

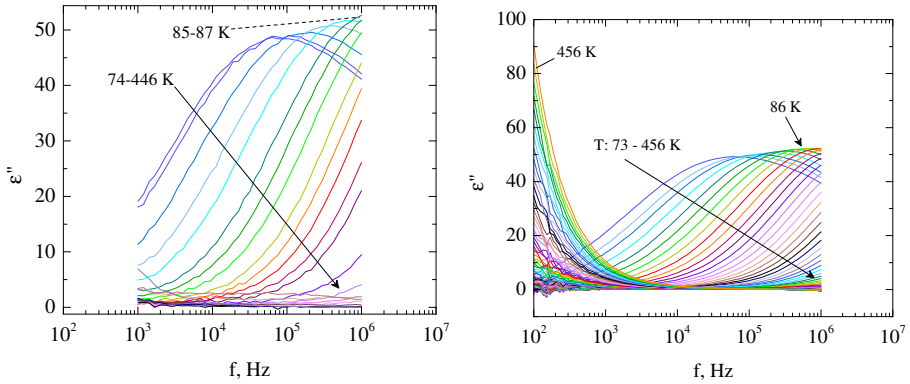

Figure 2.14: The dielectric relaxation frequency dependence for two samples of x(Sn)=0.5: the pellet sintered (a) without PVA (b) with PVA

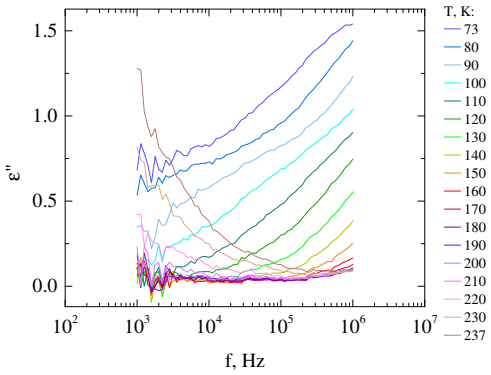

Figure 2.15: The dielectric relaxation frequency dependence for x(Sn)=0.8 sintered without PVA

the maximum of relaxation, so the decrease in intensity of the peak is seen.

In pellets with x(Sn)=0.1, 0.5 with PVA, and 0.8 the large ε" at low temperatures and low frequencies is probably related to conductivity contribution or contact polarization. Further experiments are needed to determine the relaxation behaviour processes of these compositions.

2.2.4 Transmission electron microscopy

A Transmission Electron Microscope FEI Titan operated at 300 keV was used. The sample was prepared by Focused Ion Beam.

All the previous HRTEM studies section 1.3 on $BaSn_xTi_{1-x}O_3$ were performed on compositions from ferroelectric or diffuse phase transition regions. In fig. 2.16 we show our study on x(Sn)=0.4 which is a pure relaxor composi-

tion.

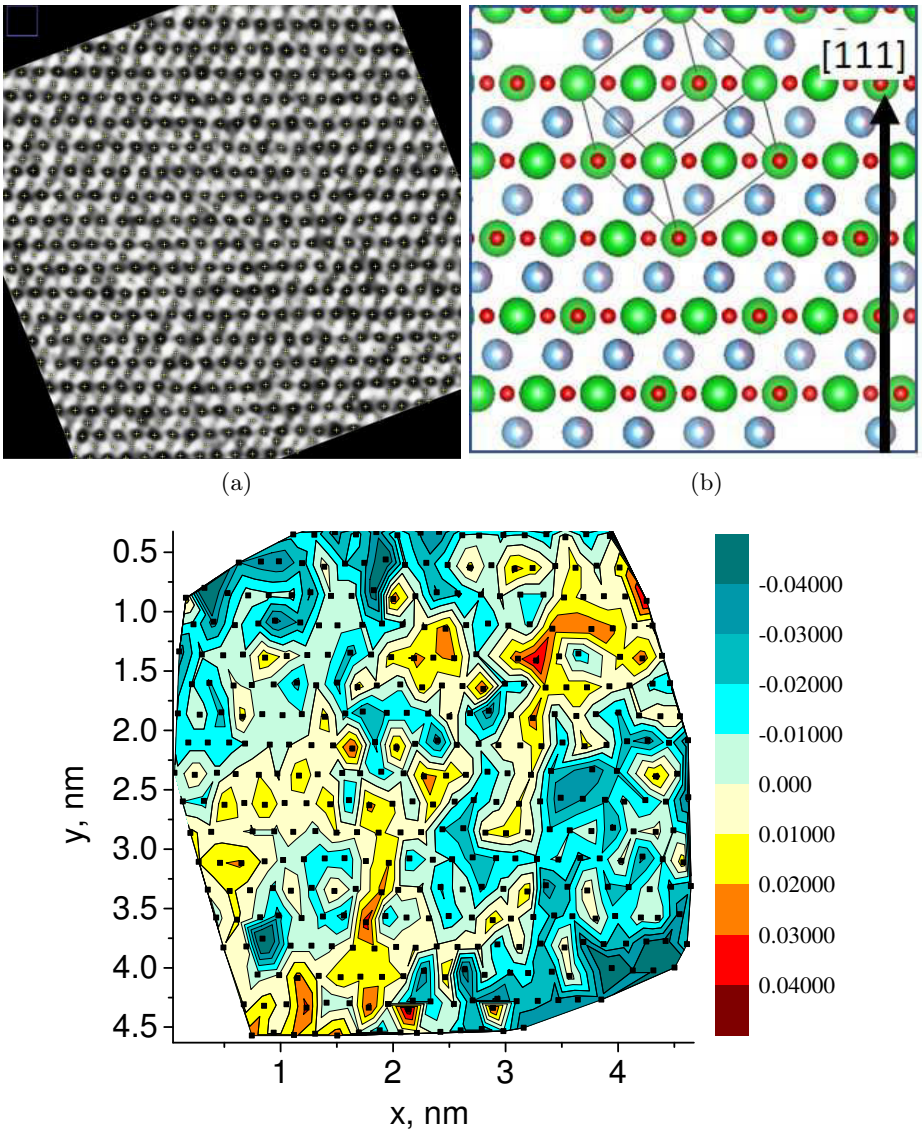

Figure 2.16: HRTEM study of $BaSn_{0.4}Ti_{0.6}O_3$ sintered pellet, (a) the image with atomic resolution, (b) correspondingly oriented structural model, with large green atoms - Ba, small red - O, large grey/blue - Sn/Ti; (c) color map of Ti/Sn displacement along <111>

In fig. 2.16a the TEM image is shown, and in fig. 2.16b - the corresponding crystallographic projection. The darkest regions in the image are related to Ba atoms, and the points in between - to Sn or Ti. The contrast in plane of the

figure comes from a sum of the atomic positions in atomic columns through the depth of the sample (< 30 nm). The indexing by color depth was performed in ImageJ software, so that atomic positions, marked by bright data markers, are taken at the point with the highest probability to find an atom within each column.

According to model of fig. 2.16b, within the plane of the figure Ba atoms are situated in horizontal lines, and Sn/Ti atoms are located in the middle between Ba lines. The displacement of Sn/Ti atoms along <111> crystallographic axis is along the vertical of the figure.

In fig. 2.16a, the atoms of Ba are less displaced than Sn/Ti, so we assume Ba displacement as zero. Based on the model of fig. 2.16b, the displacement of Sn/Ti atoms along the <111> axis is calculated as difference between the positions of corresponding Sn/Ti atom data markers in fig. 2.16a and $0.5d_{Ba-Ba}$.

The B-site atomic positions are plotted in colormap of fig. 2.16c. The atoms are displaced from their standard positions by the groups of 4-5 unit cells with the displacement stronger in the center. The PNRs seem to be of smaller size but with larger distortions. While in Ti-rich compositions of fig. 1.11 the displacements were reaching maximum 20 pm, in this relaxor compositions the $< 111 >$ displacements reach 30-40 pm and even more. According to this, the trend of increasing displacements which was seen in x(Sn)=0.16...0.25 (table 1.1) continues deeper into the phase diagram, and the presence of rhombohedral distortions is confirmed.

It is interesting to note that the distortions with the lifetime sufficiently high to be detected in TEM exist in x(Sn)=0.4 above the Td (for which the deviation from Curie-Weiss law was taken with large precision). We speculate that there could be one more critical temperature $T^* > Td$ corresponding to full disappearance of any kind of static or dynamic polar correlations.

2.2.5 Temperature dependent laboratory X-ray diffraction studies

We studied our samples in temperature by acquisition of three XRD peaks, corresponding to (200), (110), and (111) crystallographic planes. These three peaks correspond to three directions of Ti atom off-centering in T, O, and R phases. The quality of acquisition permits to estimate the phase symmetry and to find the temperatures of possible phase transitions, although the absorption of Cu K_β X-rays is high in $BaSn_xTi_{1-x}O_3$, so that only the surface grains are analysed (90% of intensity is lost at the depth of 6-7 grains).

As a reference, the three peaks for $BaTiO_3$ are shown in fig. 2.17. Phase transitions happen at temperatures roughly corresponding to ones from references. Slight deviations can result from sample history (domain state) or grain size. The phase transition R-O is seen from (110) and (200) peaks at T=195-210 K. Despite the slow heating speed ($\sim$ 0.5 K/min), the phase transition occurs not simultaneously, but within a gap of 10 K. Typically, the

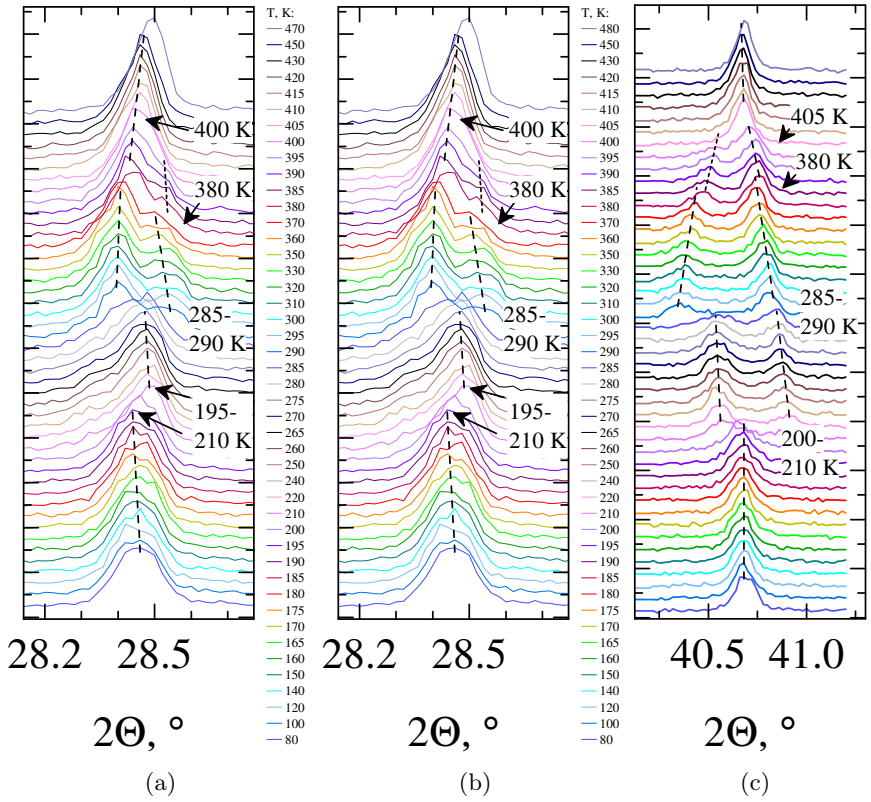

Figure 2.17: XRD peaks of $BaTiO_3$ from crystallographic planes (a) (110), (b) (111), (c) (200)

upper temperature 210 K is higher than in single crystals, but is in agreement with [48]. The next phase transition, O-T, is seen at expected temperature 285-290 K for all peaks. Finally, the T-C phase transition lies in the widest temperature interval of 370-405 K, where the 2Θ of peaks of (110) and especially (200) varies according to different linear dependence than at temperatures below or above. There is also a shift of peak maximum to larger 2Θ values (smaller lattice parameters) at T=470 K, where the static Ti displacements vanish [49], and which is close to depolarization temperature Td, determined from dielectric spectroscopy (see section 1.2.1 and section 1.4).

For x(Sn)=0.2 (fig. 2.18), which corresponds to diffuse phase transition with coexistence of relaxor and ferroelectric phases, all the three crystallographic phase transitions, remanent from from $BaTiO_3$, disappear. However, on heating there is possibly a change of slope from increasing to nearly constant in d_{200} close to 200 K, which is close to T_{VF} in fig. 1.13. Additionally, there is a shift to smaller value in d_{110} peak at the temperature which appears to be the Td=440-460 K. It is possible to speculate that since the (110) peak is most sensitive to Td, the major type of distortions in PNRs are orthorhombic.

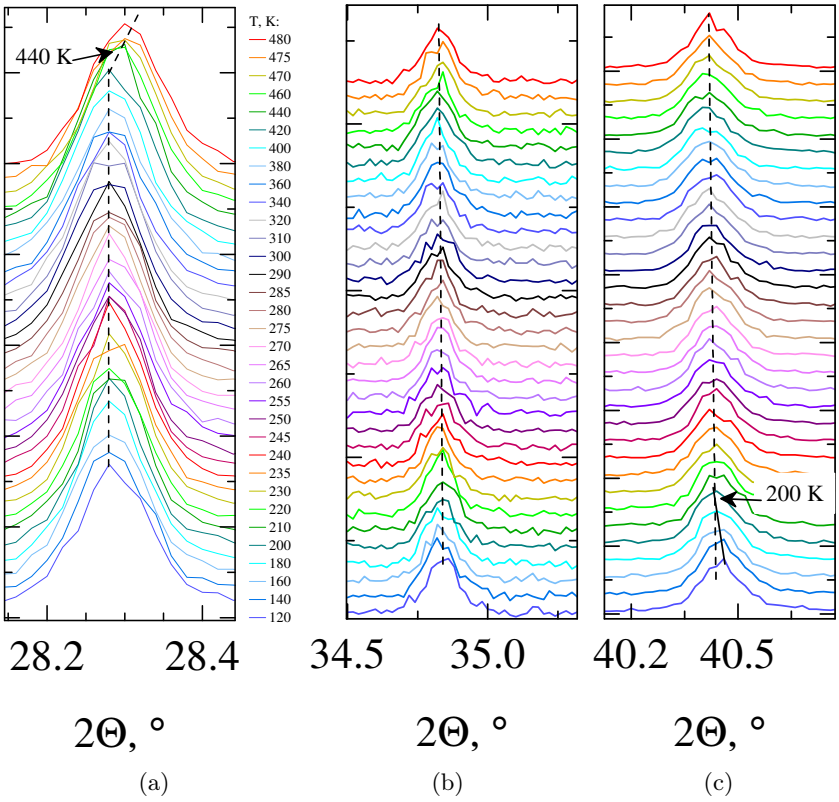

Figure 2.18: XRD peaks of $BaSn_{0.2}Ti_{0.8}O_3$ from crystallographic planes (a) (110), (b) (111), (c) (200)

In x(Sn)=0.5 (fig. 2.19), which is a truly relaxor composition, more changes are visible at 180-200 K, 260-280 K, and 380-400 K. The first region corresponds to Td=200 K as determined from dielectric spectroscopy (fig. 2.9). The d_{111} starts increasing after passing through Td=200K. The further deviation present at 260-280 K, and at even higher temperatures the deviation from Curie-Weiss law happens at 380-400 K. This means that more than one process is involved above Td=200 K. At 260-280 K the d_{110} and d_{200} start to increase similarly to d_{111} at Td=200 K. If several kinds of distortions (or phases) coexist, this temperature could correspond to disappearance of static distortions of the second type. Above T=380-400 K d_{110} and d_{111} start decreasing similarly to $BaTiO_3$, where there is also a sharp decrease in d_{110} and d_{111} at Td. The deviation reaches $1.2 \cdot 10^{-5}$ at Tx =366 K, but appears well visible by eye at 400 K (fig. 2.9a). Why the deviation happens at the temperature above the disappearance of distortions of both types is not fully clear. However, we can consider that this is related to appearance of some factor which is not related to ferroelectricity. This could be for instance the activation of defect sites, typically oxygen vacancies, coming from the $BaSnO_3$ sublattice.

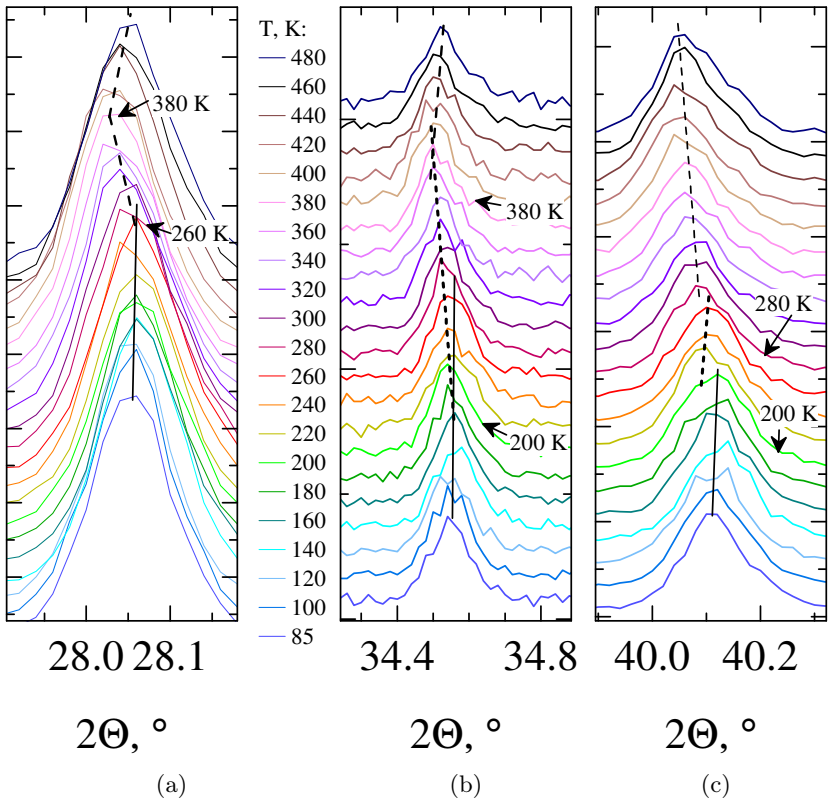

Figure 2.19: XRD peaks of $BaSn_{0.5}Ti_{0.5}O_3$ from crystallographic planes (a) (110), (b) (111), (c) (200)

In x(Sn)=0.8 (fig. 2.20) the changes happening to d_{110} remind very much ones from x(Sn)=0.5, just the temperatures are different. The values of two high-temperature regions in this sample shift 40 K higher to give T_1=300 K and T_2=420 K. These values do not anymore coincide with the Td or Tx which are found at much lower temperatures. The coupling between crystallographic structure and the polar order probably disappears because this composition is above the percolation limit of Ti atoms, and dielectric properties (Ti sublattice) and defect properties (Sn sublattice) are not related.

The changes of unit cell volume which are not related to ferroelectricity are also visible in $BaSnO_3$ (fig. 2.21) at 230-260 K for all the three systems of crystallographic plane (d_{200}, d_{220}, d_{111}).

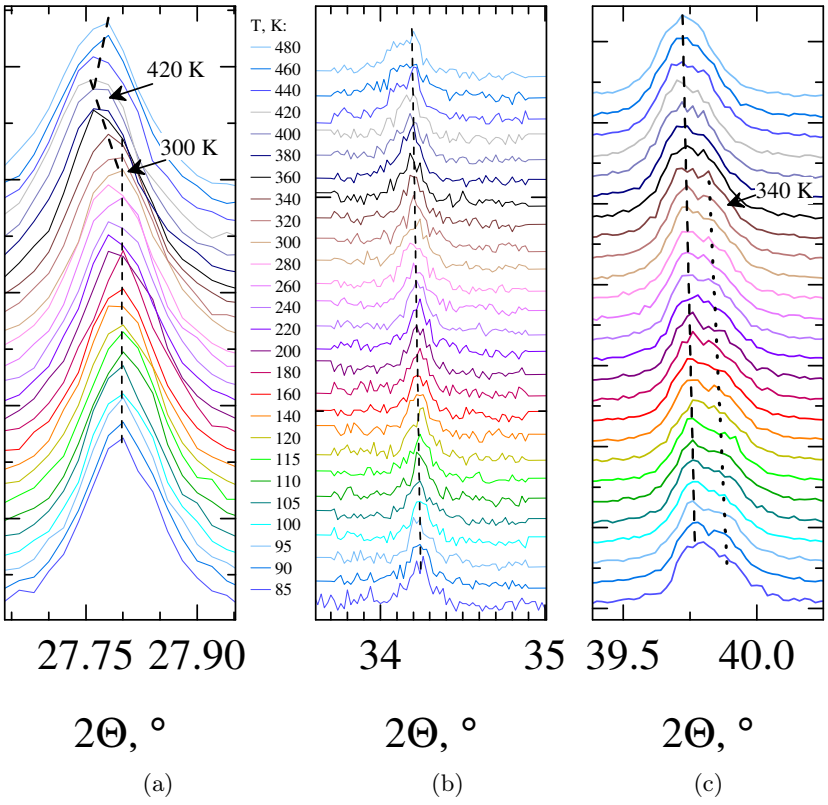

Figure 2.20: XRD peaks of $BaSn_{0.8}Ti_{0.2}O_3$ from crystallographic planes (a) (110), (b) (111), (c) (200)

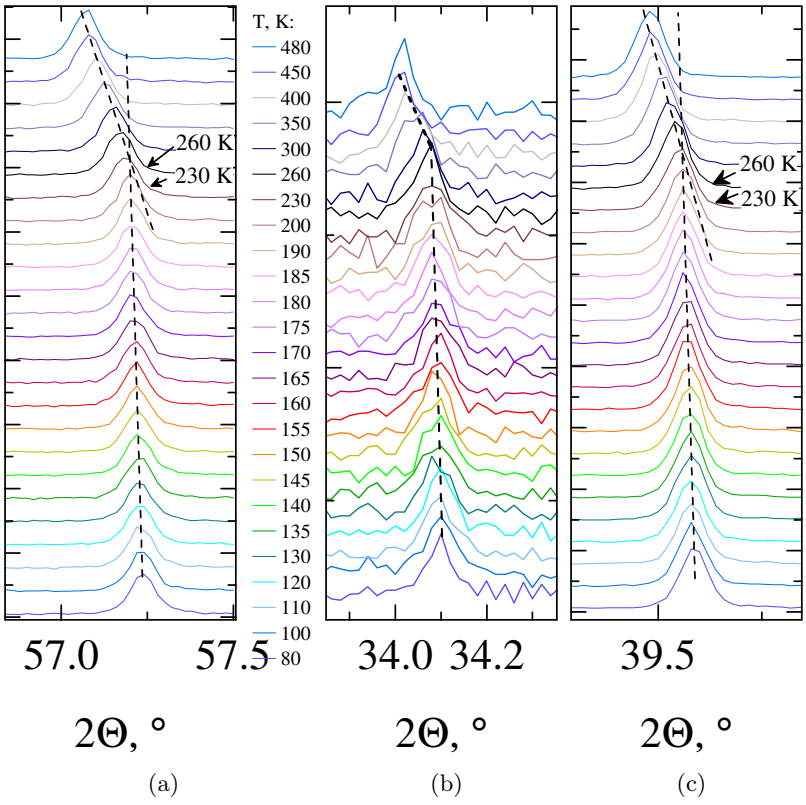

Figure 2.21: XRD peaks of $BaSnO_3$ from crystallographic planes (a) (220); (b) (111); (c) (200)

Conclusions

The samples of $BaSn_xTi_{1-x}O_3$ are synthesized. The laboratory X-ray diffraction does not show the presence of any impurities. At room temperature, the peak shape is quasicubic or cubic for all the compositions except pure $BaTiO_3$. With Sn ratio increase, the unit cell parameter varies linearly.

According to our dielectric spectroscopy data combined with previous research, the phase diagram can be separated into 1) ferroelectric phase (below x(Sn)=∼0.13 %), diffuse phase transition with possible phase coexistence (x(Sn)=0.13-0.3), relaxor phase starting from x(Sn)=0.3 and further compositions until x(Sn)=0.8.

The properties vary non-linearly in relaxor compositions, including the Td, Tm, T_{VF} decreasing exponentially on x(Sn). The compositions with x(Sn)>0.5 never transform to a polar glass since T_{CW} is negative. For Sn-rich compositions there is a high-temperature deviation from the Curie-Weiss law Tx, which we attribute to the activation of some non-ferroelectric mechanisms of interaction with the electric field, such as defect dipoles. The Tx was not discovered for other compositions because of an upper limitation of the measurement range, and whether it exists is an opened question for more experiments.

We evidence through HRTEM in x(Sn)=0.4 the PNRs with Ti displacements along the <111> crystallographic directions, despite this is at room temperature $T > Td$. The full disappearance of polar correlations probably happens at higher temperatures.

The characteristic temperatures from laboratory X-ray diffraction are compared with ones from dielectric spectroscopy in fig. 2.22. With one exception for x(Sn)=0.5, the temperature values from XRD seem to correspond to the ones from dielectric spectroscopy below x(Sn)≈0.7. Above this composition, the temperatures do not coincide, as the ferroelectric (Ti) and defect (Sn) properties are probably not coupled, if this is above the possible percolation limit of Ti atom.

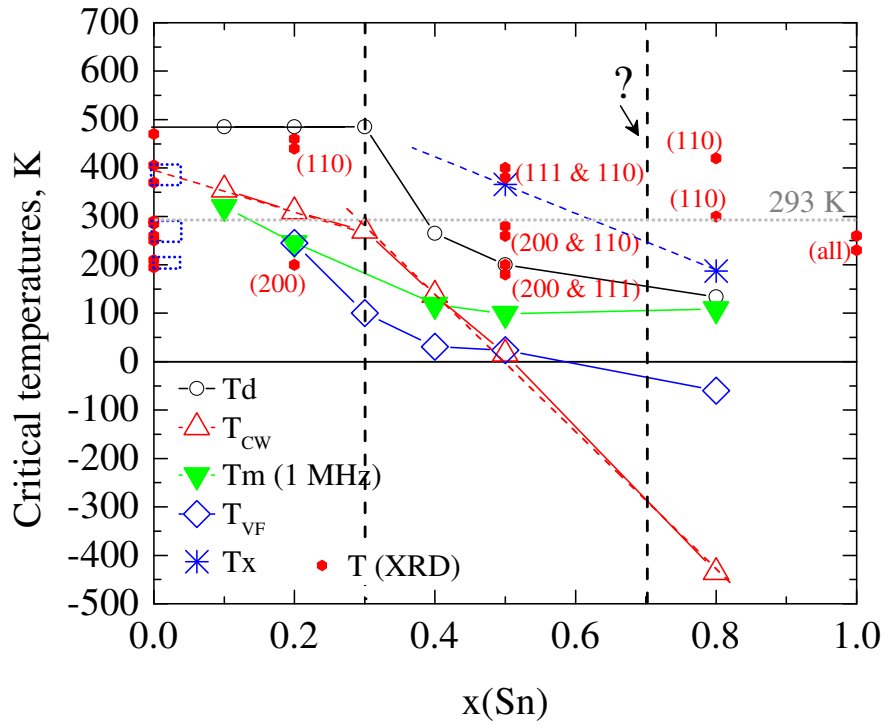

Figure 2.22: The characteristic temperatures united from dielectric spectroscopy and laboratory X-ray diffraction

Chapter 3

Optical properties

3.1 Optical Properties: Introduction

In perovskite compounds $Ba^{2+}Ti^{4+}O_3^{2-}$ and $Ba^{2+}Sn^{4+}O_3^{2-}$ the B-site atoms have the same valence. Due to this we don't expect any significant contents of compensating defects like V_O, which can potentially cause the decrease of efficiency in photovoltaic materials.

One of the parent compounds for this solid solution, Barium stannate $BaSnO_3$ is known as a promising candidate to transparent conductive oxides industry, because the electronic structure of Sn atom assures the increased mobility of electrons in the conduction band compared to $BaTiO_3$. In detail, neutral B-site atoms in the two parent compounds of the solid solution are in configuration Ti $4s^2 3d^2$ and Sn $5s^2 5p^2 4d^{10}$. After forming the chemical bonding, the conduction band minimum is formed by Ti $3d^0$ and Sn $5s^0 5p^0$, correspondingly. The s and p orbitals are known to be less localized in space than d-orbitals, providing wider conduction band with larger energy dispersion. As a result, the electron effective mass is as low as $m^* \approx 0.469 m_0$ in $BaSnO_3$ [50], compared to $m^* \approx 2.8 m_0$ in $BaTiO_3$ [51].

The band gaps of the two compounds are very similar, 3.2 eV for $BaSnO_3$ and 3.27 eV for $BaTiO_3$. Whether the band gap of $BaSnO_3$ is direct or indirect is under discussion. As for $BaTiO_3$, both in tetragonal and cubic phases indirect band gap $R - \Gamma$ is very close in energy to the direct band gap $\Gamma - \Gamma$ so it is impossible to discriminate between the two by experimental techniques [52, 53, 54, 55, 51]. For $BaSnO_3$ there is an agreement in theoretical works, as well, that the indirect band gap has lower energy than the direct one [56, 50]. Nevertheless, few existing experimental works do not reach the same conclusion, whether by UV-visible-NIR absorption spectroscopy or by Angular resolved photoelectron emission spectroscopy (ARPES) [57]. Most probably, the ambiguous results of ARPES are caused by the participation of defect levels in chemical binding [57]. Moreover, local structure imperfections or defects could be the reason why in Raman spectroscopy the modes of orthorhombic phase

Pbnm (*Pnma*) [58, 59] are detected while no signal should exist for the cubic $Pm\bar{3}m$ phase. It was shown that $Pm\bar{3}m$ has only slightly lower energy than the orthorhombic phase *Pbnm* (*Pnma*) [59].

3.2 Band gap

3.2.1 Methodology: Diffuse reflectance theory, Kubelka Munk approximation and Urbach tail

To measure the optical absorption, $Ba(Sn,Ti)O_3$ pellets were crashed into fine powders and annealed at 500°C to relax the possible stresses generated by mechanical grinding. Their optical properties were measured by UV-visible-NIR spectroscopy, spectrometer model Perkin Elmer Lambda 850. Powders cannot be measured by a standard transmission technique due to phenomena of reflection and refraction taking place at the multiple interfaces, and strong absorbance above the band gap energy value. Hence, we used the adapted measurement technique with the commercial accessory for diffuse reflection (fig. 3.1).

In such case, the diffuse component of reflection (not the specular one) is selectively collected by the specially optimized hemispherical mirrors. Assuming that the collected component is first absorbed, and then reemitted into space, and that particle size is much larger than the light wavelength $d \gg \lambda$, for the sample surrounded by air it is possible to analyse the collected data using the Kubelka-Munk formula [60]:

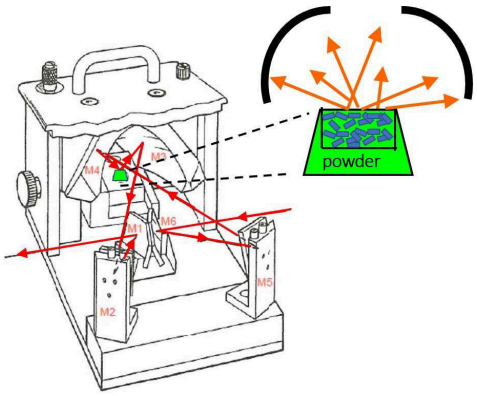

Figure 3.1: The commercial accessory for diffuse reflection UV-visible-NIR spectroscopy

$$F_{KM} = K/S = (1-R)^2/2R^2 \quad (3.1)$$

with F_{KM} – Kubelka-Munk function, which is the analogy of absorption coefficient K corrected for scattering S, R – unity fraction of diffusely reflected light.

Having F_{KM}, we recalculate it according to Tauc formula for determining the band gap Eg from the fit of the linear region close to the absorption edge [61]:

$$(h\nu F_{KM})^2 = A(h\nu - Eg) \quad (3.2)$$

with h - Planck constant, ν - frequency, E - energy.

It is possible to choose different assumption on the nature of the band gap, including direct allowed (n=1/2), direct forbidden (n=3/2), indirect allowed(n=2), indirect forbidden (n=3) band gaps [61].

Since for solid solutions the nature of the absorption edge is not known, we checked all the four possible assumptions.

3.2.2 Results of UV-Visible-NIR spectroscopy

Diffuse reflectance raw data in fig. 3.2a point out the large absorption differences of the parent compounds. Optical absorption features are seen in the Kubelka-Munk functions F_{KM} depending of the solid solution. A large increase of F_{KM} is characteristic of the optical absorption edge at a given photon energy, being the Zr-compounds (fig. 3.2c) those presenting the larger variation of the photon energy onset. No remarkable onset change is seen for Sr-compounds (fig. 3.2b), and weak and non-monotonic ones for Sn-compounds (fig. 3.2d).

The absorption coefficient of $BaSn_xTi_{1-x}O_3$ at room temperature (F_{KM}) is plotted in fig. 3.3 for a range of chemical compositions. No anomalies at the absorption edge are visible. At the same time, the onset shifts to higher energy for intermediate compositions. Overall, three peaks (possibly, groups of peaks) are visible in the spectrum of $BaTiO_3$ – at around 3.6 eV, 4.3 eV and 5.7 eV.

In solid solutions, there is a second peak appearing at 5.25 eV, which is growing with increase in Sn content. In x(Sn) $\geqslant$ 0.8 it dominates the spectrum and is the only peak in the high-energy part of the spectrum in pure $BaSnO_3$. Hence, it seems that energy levels, corresponding to high-energy absorption, do not hybridize or mix in between them. To the contrary, the lower-energy levels cannot be separated into Ti- and Sn-related contributions, probably consisting of multiple widened components, and possibly with some hybridization happening in between them. This group of peaks evolves in three steps, x(Sn) $<$ 0.2, 0.2 $\leqslant$ x(Sn) $\leqslant$ 0.6, and x(Sn) $>$ 0.8, corresponding to room-temperature regions of ferroelectricity, relaxor behavior, and the region dominated by $BaSnO_3$ matrix as will be shown in Chapter 4.

The Tauc plot was performed under different assumptions of the band gap nature to verify the presence of any additional absorption edges. There are no additional absorption features appearing, thus we consider the band gap as a direct allowed one, fig. 3.4a. The rest three plots are available in fig. A1 of the Annex. Band gap values in fig. 3.4 evolve non-linearly, increasing by around 0.35 eV until x(Sn)=0.8, and then decreasing towards pure $BaSnO_3$.

Existence of two distinct trends must be related to domination of Ti or Sn levels, as seen in the high-energy region of the absorption coefficient. One possibility of why the band gap increases where Ti atoms dominate (according to the high-energy absorption region) is that the chemical stress is imposed by Sn atoms on Ti matrix. It was shown in calculations that Sn-containing

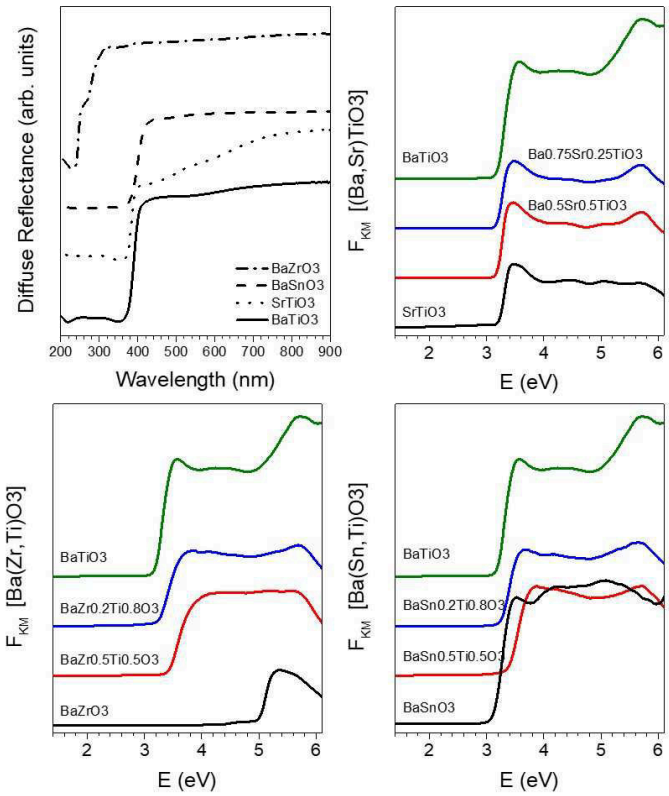

Figure 3.2: Optical properties from $BaTiO_3$-solid solutions (a) Diffuse reflectance spectra from parent compounds ($BaTiO_3$, $SrTiO_3$, $BaSnO_3$ and $BaZrO_3$, bottom to top), and (b)-(d) Kubelka-Munk F_{KM} functions vs photon energy E determined for (b) $Ba_{1-x}Sr_xTiO_3$ with x(Sr)=0, 0.25, 0.5, 1 (top to bottom), (c) $BaZr_xTi_{1-x}O_3$ with x(Zr)=0, 0.2, 0.5, 1 (top to bottom), and (d) $BaSn_xTi_{1-x}O_3$ with x(Sn)=0, 0.2, 0.5, 1 (top to bottom).

perovskites are more sensitive to strain than titanates [62]. We also evidence faster evolution of the band gap on the Sn-rich side of the diagram. In [62], the band gap of stannates increases on hydrostatic compressive strain, however the band gap of $BaTiO_3$ is supposed to decrease also. Therefore, other factors probably contribute, such as the presence of polar nano-regions in the relaxor phase and the nature of the distortion inside them.

From TEM studies of x(Sn)=0.2 in the relaxor phase [35], and multiple experimental and theoretical studies of similar relaxor system $Ba(Zr,Ti)O_3$ [63, 64, 65], one can suppose that a complicated pattern of local distortions can occur in relaxor polar nanoregions (PNR), combining local distortions of tetragonal, orthorhombic, or rhombohedral types [63]. As well, monoclinic local distortions are possible, since it was claimed to exist in pure $BaTiO_3$ at the phase transition between the orthorhombic and tetragonal phases [23]. Off-

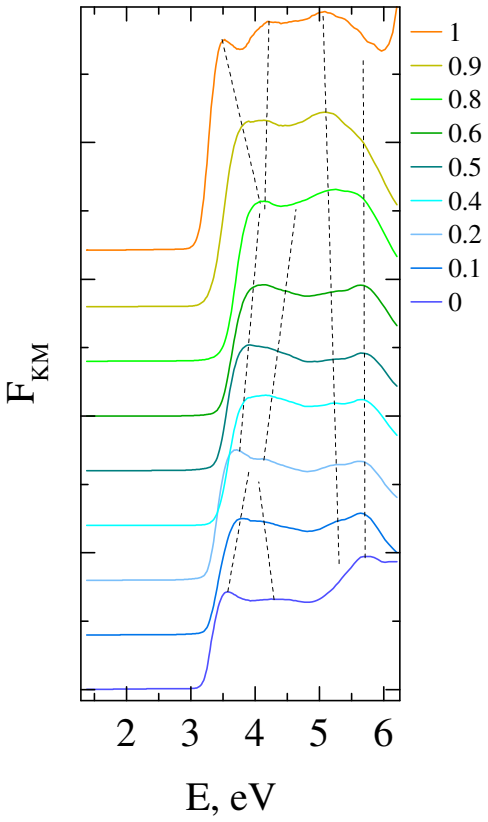

Figure 3.3: Absorption coefficient F_{KM} of $BaSn_xTi_{1-x}O_3$: compositional dependence

centering of the B-site cation of any kind leads to a deviation of the octahedral angle O-B-O from 180°, which is known to decrease the overlap of the O 2p and B-site (Ti 3d or Sn 5s 5p) orbitals. This decreases the width of conduction band, mainly making its lower region more anti-bonding and less non-bonding, which results in an increase in the energy of the CBM and the band gap [66, 67]. Moreover, PNRs, at least in x(Sn)=0.2, correspond to Ti-rich regions distributed inside a Sn-rich matrix [35]. It can be thought as coherent particles incorporated into a matrix with slightly larger lattice parameter, thus there would be tensile stress applied on the PNRs. For rhombohedral distortions, tensile stress can add up to the effect of band gap increase [68]. Finally, it is under question if the nanoscopic size of PNR ($\leqslant 2nm$) can contribute with effects of quantum confinement like it happens in nanoparticles of $BaTiO_3$ or $SrTiO_3$ powders [69, 70]. It is always possible to assume that the band gap can increase due to so-called Burstein-Moss effect. Essentially, in this case Sn substitution for Ti would create the donor defects which would result in filling of the CB, so that the measured band gap would be $Eg' = Eg + E_{filled}$. However, in this case the conductivity is supposed to increase, which is not the

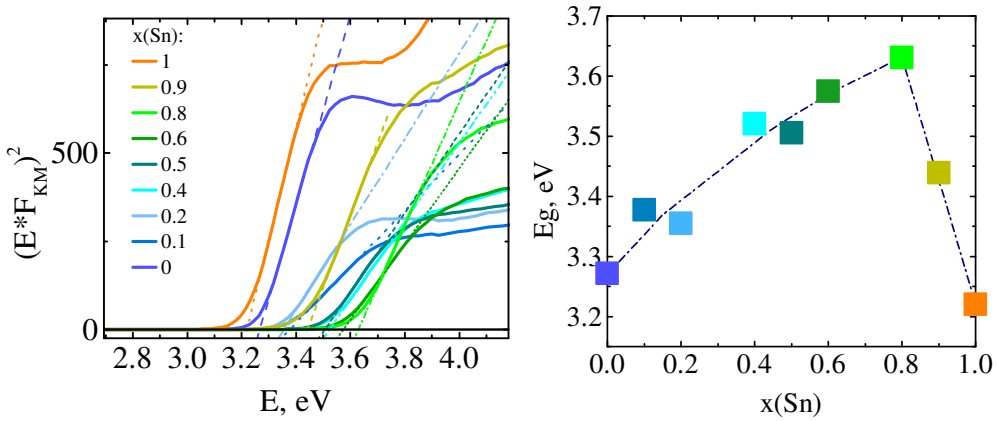

(a) (b)

Figure 3.4: Band gap of $BaSn_xTi_{1-x}O_3$: compositional dependence at room temperature (a) Tauc plot under direct Eg assumption for different compositions (b) the extracted Eg values (error bar is smaller than the symbol size)

case for our ceramics fig. 3.5. In further chapters, we will discuss the origins of band gap behavior based on experimental data from other techniques.

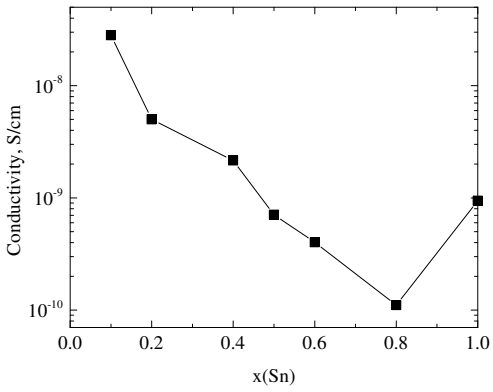

Figure 3.5: Conductivity of $BaSn_xTi_{1-x}O_3$: compositional dependence

3.3 Chemical disorder-driven absorption edge

3.3.1 Types of disorder

As can be seen in fig. 3.3, at the low-energy limit the absorption does not start abruptly, but has a non-linear shape. Such an absorption tail most often has an exponential shape, in this case it is called an *Urbach tail*. Its shape and width depend a lot on imperfections of the crystalline lattice. In relaxor

systems, this is a particularly important parameter to be analysed, since it is straightly connected to physical properties.

Studies of absorption tail started as early as 1953, when F. Urbach studied the sensitivity of photographic emulsions of multiple semiconductors (including the wide-gap ones). He noticed that low-energy part could be described closely by $e^{1/kT}$ [71]. Later studies, for instance on amorphous hydrogen-doped silicon [72] concluded that any kind of disorder contributes to widen, or blur, the allowed density of states ρ of the band gap edges according to the law $ln\rho = E^n$, where n can be different depending on the kind of disorder.

In general, there can be structural static type of disorder Eu_S (due to immobile defects), or the compositional disorder Eu_{Comp} in solid solutions due to distribution of chemically substituted atoms, and temperature-related disorder Eu_T [73]:

$$Eu = Eu_T + Eu_S + Eu_{Comp} \tag{3.3}$$

The latter one Eu_T most often results from thermal lattice vibrations (phonons), but is also affected by disorder phase transformations characterized by different dynamics of ions or defects:

$$Eu_T = Eu_{ph} + Eu_{dyn} \tag{3.4}$$

The thermal disorder is described by the formula

$$Eu_{ph} = Eu_0 + Eu_1 \frac{1}{e^{(\Theta_E/T)} - 1}, \tag{3.5}$$

with Eu_0, Eu_1, Θ_E - constants. It is suggested that the thermal mechanism occurs mainly due to valence band electron coupling to phonons [74]. Another approach tells that the exciton at light absorption is momentarily trapped at the vibrational levels created by phonons [73] (self-trapped ST exciton). This point of view is supported by the fact that the Urbach tail also appears in photoluminescence spectra which represent the recombination of ST exciton [75]. The phonons participating in the process are mainly those involving the electric field change, the longitudinal optical LO branch, where the Ti-O bond vibrates parallel to the polarization direction, so that overlap of O $2p$ and Ti $3d$ orbitals of π type is modulated [74]. Note, same effect of electric field modulation can be caused by fast transverse acoustic phonons, which result in a so-called piezoelectric absorption edge [76]. Moreover, if this effect of changing the polarization becomes static, for instance in the phase transition from cubic (paraelectric) to tetragonal (ferroelectric) $BaTiO_3$, then the band gap itself is modified [74]. The fact that the band gap varies according to similar law as the Raman shift was pointed out by [77].

The second factor in temperature changes of Eu is the possibility of disorder phase transformations. Those are characteristic to materials with high defect concentrations, so that there are unique favorable defect positions and/or

defect mobility in the lattice of each phase. The different favorable states are separated at a critical temperature Tc. The state above Tc is called superionic state and is distinguished by high ionic conductivity, as for example in $Cu_6P(S,Se)_5(I,Br)$ [78]. The characteristic large changes of Eu happen also at paraelectric to ferroelectric phase transitions, as well as at low temperature when the dynamics of the system becomes frozen, as shown in ferroelectric SbSI (fig. 3.6) [79]. Similar shapes of $E_U(T)$ dependences were observed [80] in perovskite relaxor solid solutions $[Pb(Ni_{1/3}Nb_{2/3})O_3]_{1-x}$ - $[PbTiO_3]_x$ (PNN-PT).

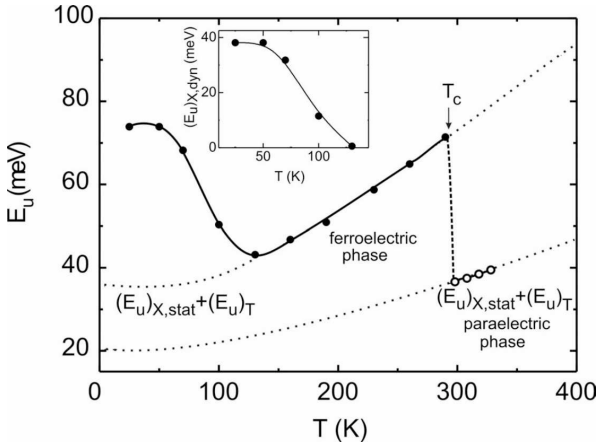

Figure 3.6: Temperature dependence of Urbach tail in ferroelectric SbSI, showing tree regimes of disorder: frozen dynamics, ferroelectric, and paraelectric phases

Structural disorder is illustrated in the simplest way by the fact that Urbach energy decreases from amorphous to polycrystalline thin films to single crystals of semiconductors. In SnO_2, the corresponding values are 440 meV, 230 meV, 37 meV [81]. Similarly, there is a trend of Eu decrease for amorphous thin films under annealing, since ordering of the structure happens. This trend was demonstrated in amorphous silicon [82], as well as in SnO_2 [81]. It is interesting that for amorphous semiconductors, there is a linear dependence of band gap Eg on Urbach energy Eu, and correspondingly on the structural disorder [82, 81].

The compositional contribution to the overall disorder parameter is known to follow in many materials the equation:

$$Eu_{Comp} = Ax(1-x), \tag{3.6}$$

where x is the amount of chemical substitution [73].

All the three contributions to disorder were disentangled one from each other and analysed quantitatively in $Cu_6P(S,Se)_5(I,Br)$ solid solutions fig. 3.7.

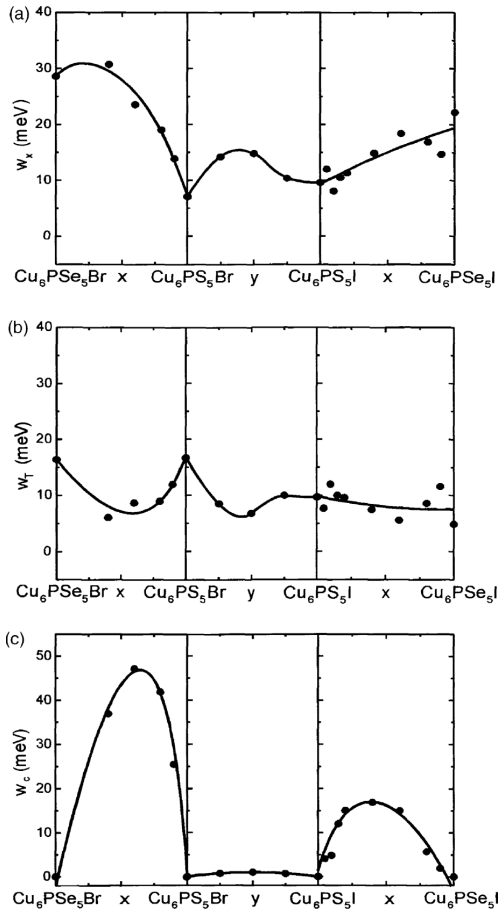

Figure 3.7: Compositional dependence of disentangled components of disorder parameter Eu ($w_T = Eu_T$, w_X=Eu_S, w_C=Eu_{Comp}) [73]

For intermediate compositions of solid solutions, Eu_{Comp} contributes to increase Eu, Eu_T decreases or stays constant, w_X=Eu_S due to the possibility of defect formation.

Without knowing the predominant reason for disorder, one can find the Eu value according to equations

$$\alpha = \alpha_0 e^{\frac{E}{Eu}} \tag{3.7}$$

$$ln\alpha = \frac{1}{Eu}E + ln\alpha_0 \tag{3.8}$$

with α - F_{KM} in our case.

In case of structural defects, the Urbach energy Eu can be understood in terms of trapped defect states in the band gap below the conduction band minimum or above the valence band maximum [83]. In $BiFeO_3$ nanoparticles

[83] Eu describes the properties of the particle skin layer. As the size varies, the surface strain and the polarization state changes, the defect energy is shifted, so the Eu value is size-dependent. In addition, it should reflect the sample history, such as processing and annealing atmosphere which influence the defect states.

3.3.2 Urbach tail width in Ba(Sn,Ti)O_3 at 293 K

Figure 3.8 shows the Urbach plots. For both pure parent compounds, there is a single linear region of the plot, with no absorption below. For intermediate compositions, there is an additional shoulder at the lower-energy side. This shoulder is present for x(Sn)=0.1 to 0.6, and seems to disappear in x(Sn)$\geqslant$0.8. It is known that the presence of the second linear part of the Urbach plot can point at the coexistence of different phases or different types of disorder, at least in $BaTiO_3$ close to Tc [84]. However, here there is no clearly defined linear region.

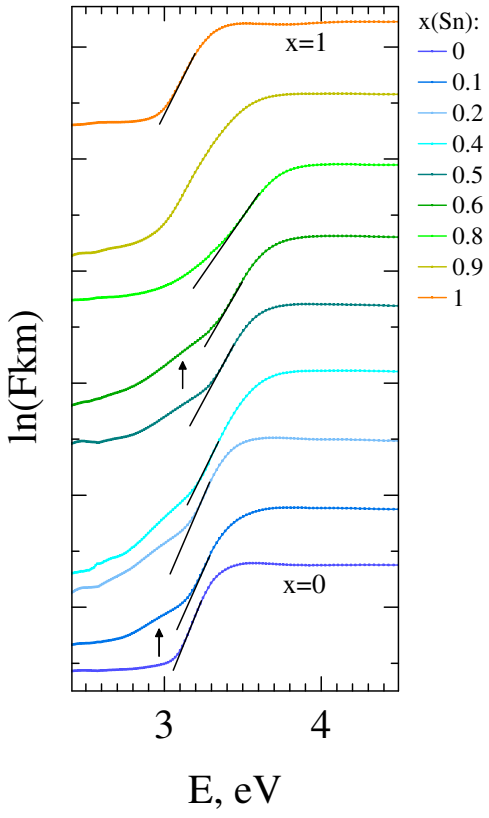

Figure 3.8: Urbach-type plots for different Ba(Sn, Ti)O_3 compositions

Whether this absorption comes from defect levels inside the band gap, or from coupling to more than one phonon due to multiple kinds of distortions

in PNRs, needs more experimental proofs and discussion.

In fig. 3.9a the fitted Eu values definitely fall into two regimes of disorder. Inside both of them, the data can be fitted with eq. (3.6). The boundary composition between the two regimes, x(Sn)=0.8, is also separating the two regimes for the band gap compositional dependence. Based on this,the band gap evolution is definitely connected to different local environments of the B-site atoms. To stress this, we plot Eg against Eu in fig. 3.9b. As in case with amorphous SnO_2 and Si in the process of annealing, there is a linear correlation of the band gap to disorder within each of the two regimes separated by x(Sn)=0.8.

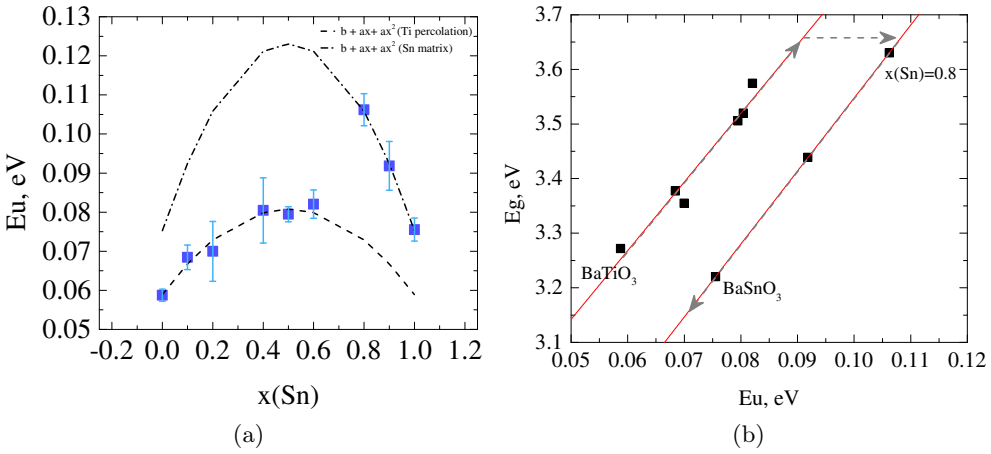

Figure 3.9: Urbach tail width Eu in $Ba(Sn,Ti)O_3$: (a) compositional dependence (b) coupling between disorder Eu and the bandgap Eg

Remarkably, the tangent is approximately the same for both regions (12.58 and 13.37), and the Sn-rich region seems to be parallelly shifted towards the higher disorder side. The reason is probably that the Sn matrix promotes the formation of structures with a lot of defects, which is specific for $BaSnO_3$ and which makes it a good protonic conductor at relatively low temperatures $T \geqslant 300\ ^\circ$ C [45, 85]. For both regions, the tangent is of opposite sign than in the temperature-dependent plot on amorphous semiconductors. In that case, lower values of Eu correspond to higher annealing temperatures, less disorder and defects, so larger band gap. In our case, larger disorder Eu corresponds to larger band gap Eg, demonstrating the clear connection between the two. The reason is probably connected to the nature of the PNR and will be explained later on.

3.4 Temperature evolution of band gap and disorder-related absorption tail

3.4.1 $BaTiO_3$

For $BaTiO_3$, we are capable to deduce the non-linear temperature dependence the Tc for T-C phase transformation from Eg, and the correlation of Eu with the different structural transitions and dependence on powder sample preparation.

The band gap of $BaTiO_3$ (fig. 3.10a) has two linear regions, below 398 K and above 550 K, which correspond to the pure tetragonal and cubic phases. In between, there is a non-linear region where the band gap decreases fast close to Tc and slowly closer to 550 K.

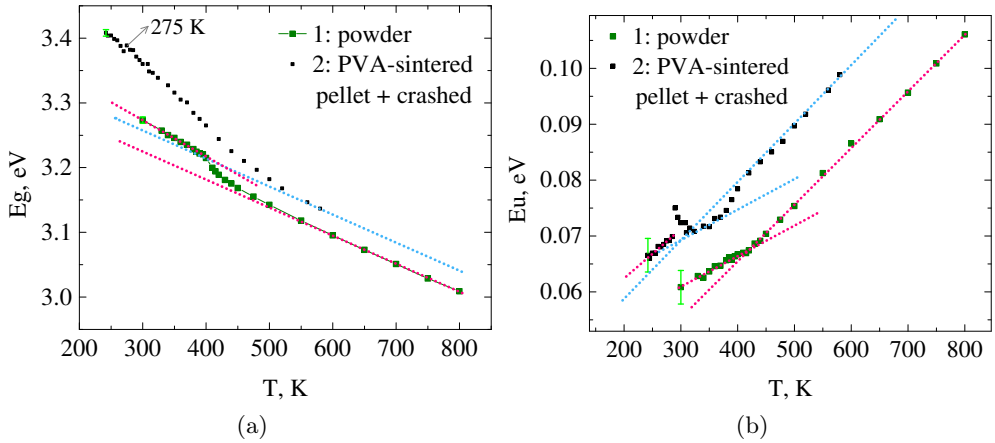

Figure 3.10: Optical properties of $BaTiO_3$ powders (straightly after solid state synthesis and after sintering as a pellet with PVA and crashing: temperature dependence of (a) band gap Eg (b) Urbach tail energy Eu (typical error bar values are shown at lowest temperatures)

There is a difference between the curves for sample 1 and sample 2. The linear regions are more visible in sample 1, since sample 2 is obtained by crashing the pellet and without the annealing to relax the possible mechanical strains. In sample 1, the change of Eg is ≈0.05 eV if taken in between the value at 300 K and the continuation of the linear fit of high-temperature data.

Because of different processing of sample 1 and 2, the curve for sample 2 is not the same as the one for sample 1. Both Eg and the disorder Eu are higher. Sample 2 was pressed into the pellet with the binding agent PVA and sintered at 1280°C. As a result, the grain size could increase, the presence of PVA could change the structure of the grain boundaries, the pressure could introduce the mechanical strain so that the domain structure and twin pattern would alternate. In addition, sample 2 was measured starting from lower

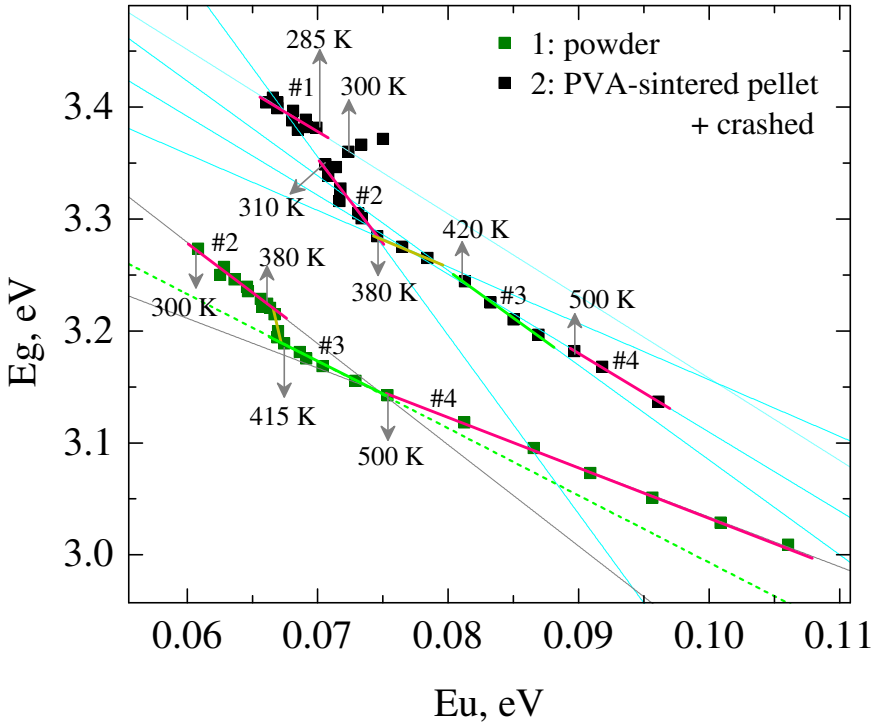

Figure 3.11: Band gap Eg dependence on disorder Eu in $BaTiO_3$

temperature T=240 K and heated afterwards. It means that also cooling the sample down to the orthorhombic phase could have altered the twinning state and changed the state of disorder [48]. It also is important to note that the UV-visible absorption process is happening close to the surface of grains, so that properties of grain boundaries may contribute significantly.

The Urbach tail width Eu for sample 1 (fig. 3.10b) is separated into two linear regions by the T = 420 K just above the T→C phase transition. The linear fit quality is good at 420-500K, but seems worse above 500 K. For sample 2, anomaly is visible at O→T phase transition (285 K), and the curve is non-linear for temperature of tetragonal phase. The transition to new linear region is visible at 400 K.

As we showed before on example of compositional disorder in $Ba(Sn,Ti)O_3$ series, the plot Eg=f(Eu) helps to distinguish more clearly the different regimes of disorder. In fig. 3.11, data points for sample 2 in Eg-Eu coordinates are shifted along the x=y diagonal according to increase of both Eg and Eu.

3.4.1.1 Sample 1

Three regimes can be seen for sample 1 (fig. 3.11): #2 linear evolution for tetragonal $BaTiO_3$, non-linear phase transition region at 380-415 K, #3 low-temperature cubic phase at 415-500 K, #4 high-temperature cubic phase.

Between regions #2 and #3, the band gap non-linear variation at the tetragonal to cubic phase transition was observed for $BaTiO_3$ [86, 54, 74] and for $PbTiO_3$ [87]. The origin of non-linearity is not exhaustively explained. First possibility is that it is caused by the coexistence of multiple local energetically favorable states at the same energy, the proportion of one and another being time-dependent close to Tc [84]. A second possible reason is that the band gap change is related to a non-linear polarization change [87]. More in detail, there is a coupling between the polarization, phonon modes, and the band gap. Their relationship was studied in ref. [74], where the absorption was measured on single crystals under polarized light, with $Eg_{\parallel}$ (band gap measured with light polarization parallel to the crystal polarization axis) being higher than $Eg_{\perp}$ (measured with light polarization perpendicular to the crystal polarization axis). The separation between the two band gaps plotted against P^2 was shown not to disappear fully at the phase transition, but to gradually linearly decrease above Tc [74]. It is proposed according to parallel study of Eu and Eg that both the valence band electrons and the conduction band empty states can be possibly coupled both to crystal polarization and polarization fluctuations in the cubic phase. Several works agree that the phonon participating in the process is most probably not the soft mode Slater $A_1(TO_1)$, but rather one of the LO phonons [74, 86], which have the wavevectors parallel to the polarization axis. Such phonons can change the chemical bonding by modifying the dynamic hybridization between Ti and O orbitals [88].

The very important question is why we are able to detect two regimes (#3 and #4) by optical methods for a range of temperatures where there is a cubic phase. From studies by multiple methods it is well-known that even above Tc ≈400K in $BaTiO_3$ there are some local polar correlations [89, 90]. These correlations appear as chain-like tetragonal displacements in the column of Ti-O-Ti [90]. The size of these correlation regions were determined by different techniques as several unit cells (∼ 30 Å) [74]. Such regions should be in principle similar by their dielectric response to relaxors. Despite the temperature-dependent dielectric response of $BaTiO_3$ showing no frequency dependence in Hz-MHz range, it was shown that a relaxation in THz range is frequency-dependent [91, 92, 84]. The frequency values are close to the ones of Ti site hopping between eight rhombohedral directions, which is energetically favorable for very short times in all $BaTiO_3$ phases, including the cubic one [89].

Acoustic spectroscopy and resonant ultrasonic spectroscopy both showed that in $BaTiO_3$ there is a temperature above which the polar correlations disappear letting place to a purely cubic phase (T^* ≈550 K) [49, 48]. Moreover, in the range of temperatures between T^* and Tc one more critical temperature T'=500 K can be defined, which is limiting the dynamic polar correlations for $T' < T < T^*$ and static polar chains for $Tc < T < T'$. Most probably, T' can be compared to Td from ref. [43].

The same value of the critical temperature was found for the dielectric response of cubic $BaTiO_3$. In detail, there is a shoulder in the THz range, whose behaviour changes above 550 K. This shoulder is modelled below 500 K by the oscillator responsible for short-range correlations along the <100> direction, and at higher temperatures it becomes progressively smaller and cannot be described anymore by the same model [93]. Also from Raman spectroscopy, the low-wavenumber mode is seen to be saturating in frequency (oscillator strength) when the temperature falls below 500-550 K [94]. Similar, a T^* seen by different techniques is related to the behaviour of the oscillator which appears due to coupling between the Slater $A_1(TO_1)$ soft phonon mode and the Debye-like central mode (or order-disorder mode) which is due to eight-site Ti hopping. This mode is found at 100-135 cm^{-1} (3-4 THz) [92, 95, 96, 93] and was also claimed to be related to a width of the disorder-related Urbach tail (0.025-0.075 eV) which is found in titanates.

Above T^*=550 K the band gap is linear in our measurement and in agreement with ref. [74].

3.4.1.2 Sample 2

For sample 2 (fig. 3.11), region #1 corresponds to the O phase, followed by the Eu anomaly at the phase transition, region #2 for T phase, phase transition 380-420 K, region #3 for cubic phase with polar correlations (420-500 K), and region #4 for cubic phase without polar correlations. Overall, same temperature intervals are kept for corresponding phases as in sample 1. However, the slopes of the corresponding regions differ very much, for reasons which are mentioned before.

The Eu non-continuity at the phase transitions, specifically at Tc, was also seen in $BaTiO_3$ ref. [84]. Similar to our case, Eu increases during heating, and decreases during cooling [84].

3.4.2 $BaSn_{0.1}Ti_{0.9}O_3$

For $BaSn_{0.1}Ti_{0.9}O_3$ the analysis of Eg and Eu enables us to determine the temperature of the phase transition between the rhombohedral and the cubic phases as seen in synchrotron diffraction. In addition, we discover the correlation between Eu and peaks of dipole dynamics in dielectric spectroscopy, these peaks being related to ferroelectric and PNR coexistence.

The band gap of $BaSn_{0.1}Ti_{0.9}O_3$ behaves non-linearly but without any anomalies fig. 3.12a. The fit can be done using the Bose-Einstein formula:

$$Eg(T) = Eg(0) + A(n_{BE}(T) + \frac{1}{2}) \tag{3.9}$$

$$n_{BE}(T) = \frac{1}{e^{\frac{Tph}{T}} - 1} \tag{3.10}$$

where $n_{BE}(T)$ is the Bose-Einstein factor which characterizes intensity (occupation of allowed vibrational levels) of the phonon mode with characteristic temperature Tph.

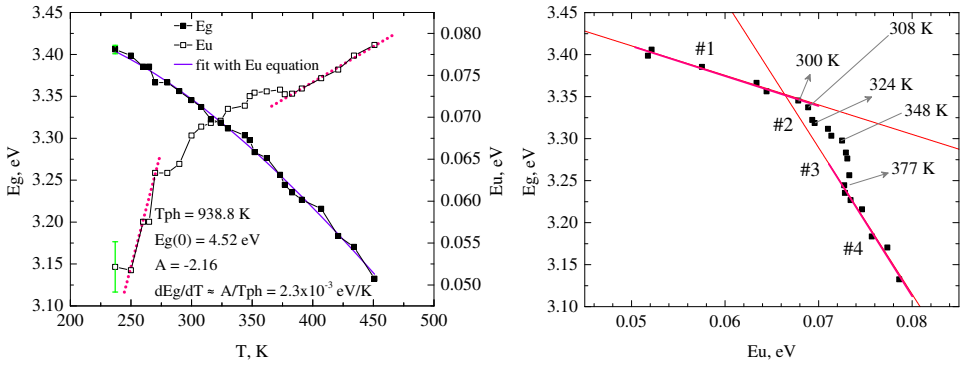

Figure 3.12: Optical absorption of $BaSn_{0.1}Ti_{0.9}O_3$ powders: (a) band gap and Urbach tail width temperature dependence (typical error bar values are shown at lowest temperatures) (b) band gap dependence on disorder

The Eu values can be separated into three parts, (a) the sharp increase of disorder between 237 and 270 K, followed by (b) the non-linear region of complicated shape and (c) the linear region above 377 K.

Plotted in Eg-Eu coordinates (fig. 3.12b), the points form four distinct regions. Region #1 corresponds to rhombohedral phase according to [33]. Then, two non-linear regions follow for temperature spans 300-324 K and 324-377 K. Above 377 K and until 450 K, there is a linear evolution of Eu.

From what is known on dielectric properties of $BaSn_{0.1}Ti_{0.9}O_3$ [43], the Td is around 485 K. Unfortunately, our measurement stops at 450 K, so we are not able to detect the difference between the relaxor ferroelectric phase and the paraelectric one. The fact that there are two regions of disorder transition might be related to the coexistence of two different dielectric relaxation processes in x(Sn)=0.15 and a broad distribution of relaxation times in x(Sn)=0.1 [97], where the dielectric losses seem asymmetric, possibly with traces of a second dielectric relaxation.

Moreover, in our data there is a trend to double relaxation in relative permittivity ε in pellets x(Sn)=0.1, which were prepared without the binding agent. There is a first lossy process peak at $\approx$ 310 K and a second one at 350 K (fig. 2.11). This is similar to 308 K and 348 K in optical data (fig. 3.12b), which are the points where there is a the largest difference between the continuation of the linear fit for #4 and each of the semi-circles of the two disorder processes.

In the sample sintered with PVA (like the one studied here by UV-VIS) there are two dielectric relaxations coexisting at one temperature for a wide

range of measurements, first peaking at 300 K and second at 315 K fig. 2.11.

The optical measurement results have critical points closer to the sample sintered without PVA, likely because the powder was previously annealed at 500°C. Thus, both the powder in optic measurements and the porous pellet in dielectric setup have the grain boundaries more exposed to the atmosphere under heating, which could change the defect concentrations. The difference in temperature between the maxima of relaxation intensity is slightly larger in these two samples, which means that the separation in temperature between the two relaxations might depend on defect densities, for instance V_O concentration. Turning back to the dielectric spectroscopy results of Chapter 1, the two relaxations in 0.1<x(Sn)<0.175 represent [44] ferroelectric and PNR contributions.

3.4.3 $BaSn_{0.2}Ti_{0.8}O_3$

For this composition, we are able to detect multiple transition temperatures, which correspond to critical temperatures of polar correlations from dielectric spectroscopy [43].

For x(Sn)=0.2 both Eg and Eu have an anomaly close to 260-270 K fig. 3.13 . The degree of disorder decreases, and starts to increase again further. Same trend is visible for the band gap. Further, Eg decreases monotonously up to the kink at 552-570 K. The Eu has additional change of slope at 324 K, and a kink close to 493-500 K.

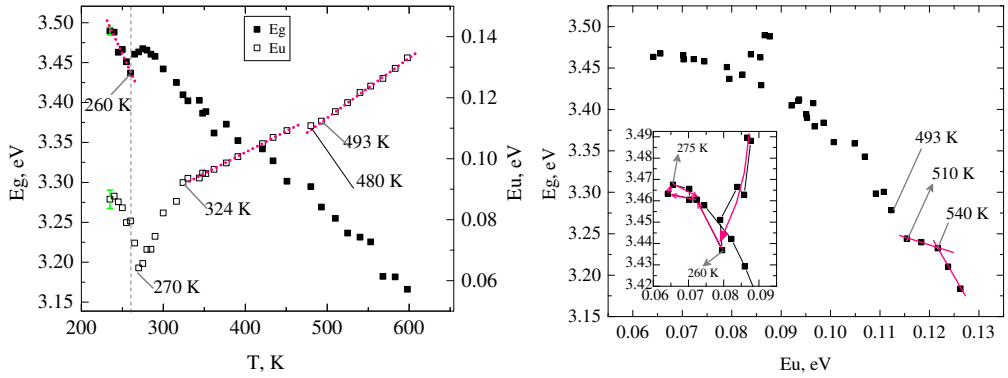

Figure 3.13: Optical absorption of $BaSn_{0.2}Ti_{0.8}O_3$: (b) temperature dependence of Eg and Eu (typical error bar is shown in green for lowest temperature) (b) dependence of Eg on Eu

In the inset of fig. 3.13, first the band gap decreases as disorder decreases until 260 K, then the disorder continues to decrease but the band gap shows opposite trend, and finally, starting from 275 K, the band gap decreases as

disorder increases, which is a standard behavior for semiconductors [81, 82]. The high-temperature transition is illustrated better in fig. 3.13b, because the range of transition itself can be determined as 510-540 K.

To compare with dielectric spectroscopy data, in the porous pellet the maximum intensity of low-frequency relaxation is 260 K (and 210 K for the high-frequency one, which is out of range of optical measurement). If compared to dielectric spectroscopy data from [43], 260 K is close to both Tm and T_{VF}. At 275 K there is T_Q, where the $\frac{1}{\varepsilon}$ at $T > Tm$ starts to deviate from a quadratic dependence on temperature and the transition to Curie-Weiss law begins. The point 324 K is close to a characteristic temperature T_{CW} (ideally, 315 K) above which the Curie-Weiss law fits the data [43] fig. 3.13. The points of 293 K and the process 510-540 K might be related the disappearance of static PNR (Td=485 K in [43]) and to the disappearance of dynamic polar correlations.

3.4.4 $BaSn_{0.5}Ti_{0.5}O_3$

For this composition, the band gap appears to decrease linearly on temperature fig. 3.14a. The Urbach tail width increases with three linear regions: below 420 K, 420-520 K, 520-610 K, and above this temperature. According to band gap linearity throughout the temperature span of measurement, no new critical points appear in the plot of fig. 3.14b.

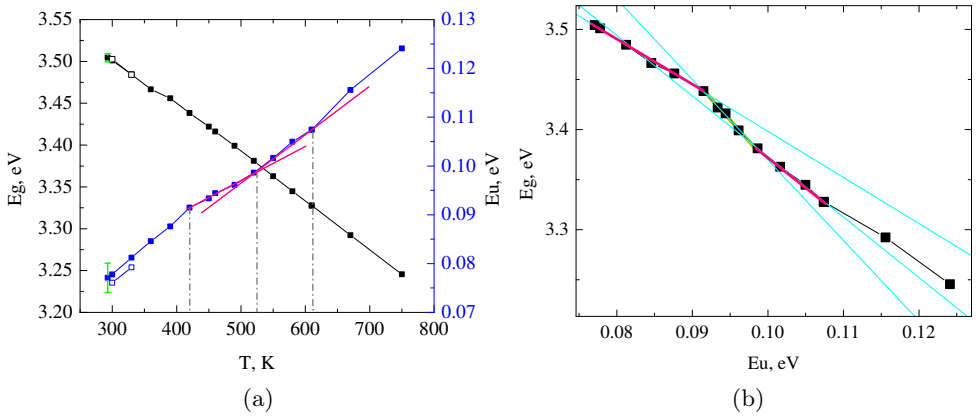

Figure 3.14: Optical absorption of $BaSn_{0.5}Ti_{0.5}O_3$: (a) temperature dependence of Eg and Eu (typical error bar values are shown at lowest temperatures) (b) dependence of Eg on Eu

3.4.5 $BaSnO_3$

The band gaps of both $BaSnO_3$ samples shown in fig. 3.15a do not show any considerable non-linearities. Between the two samples, the rate of decrease over the temperature is different. This difference is more pronounced than in two samples of $BaTiO_3$. Probably, in $BaSnO_3$ the defect disorder plays a much more important role for the properties than in $BaTiO_3$, or the defect concentrations are higher at the same conditions. Indeed, $BaSnO_3$ tends to be a good ionic conductor due to high concentrations of defects [29]. It's electronic conductivity is mainly controlled by defect-related mechanisms [98, 99].

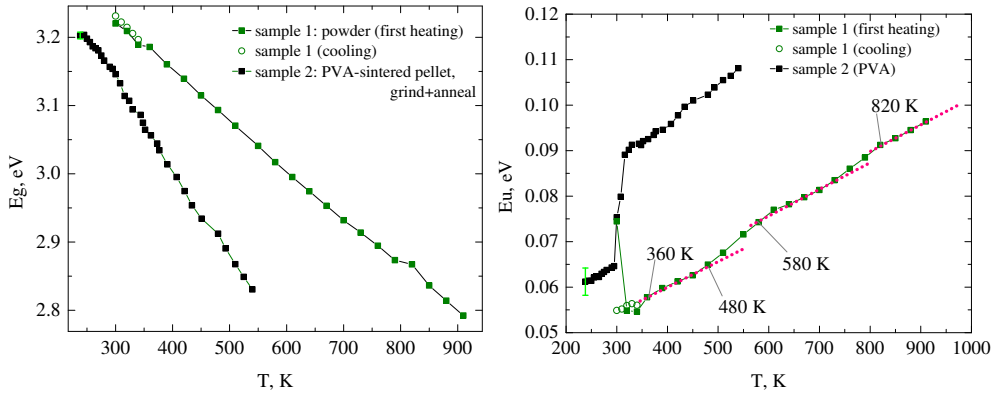

(a) (b)

Figure 3.15: Optical absorption of two $BaSnO_3$ samples: (a) temperature dependence of Eg and (b) of Eu (typical error bar values are shown at lowest temperatures)

The Eu dependence on temperature is shown in fig. 3.15b. The plots do not coincide for the two samples. Nevertheless, despite the average slope of evolution is similar starting from above 360 K. It is however evident that the data cannot be fitted by a linear dependence, since there are some small non-linear variations superimposed. Moreover, there seem to be unexpected large non-linearities at temperatures below 360 K for both samples, but nevertheless appearing different in the plot of fig. 3.15b.

To clarify this behavior, we plot the band gap dependence on disorder in fig. 3.16. In the close-up on the right of fig. 3.16, it is visible that around 300 K sample 1 does not behave in a similar way on heating and cooling, probably because it gets oxidized or reduced during heating, or there is a rearrangement of defect structure. In fact, both cooling during the processing of the sample and heating during this measurement is done in air, but the latter takes twice longer time and could act as annealing. The similarity between first heating for sample 1 and 2 is that both of them seem to change regime at 295-300 K. In fact, in both dielectric measurements of [29] and [100] there

seem to be some slight anomaly around 300 K and 324 K.

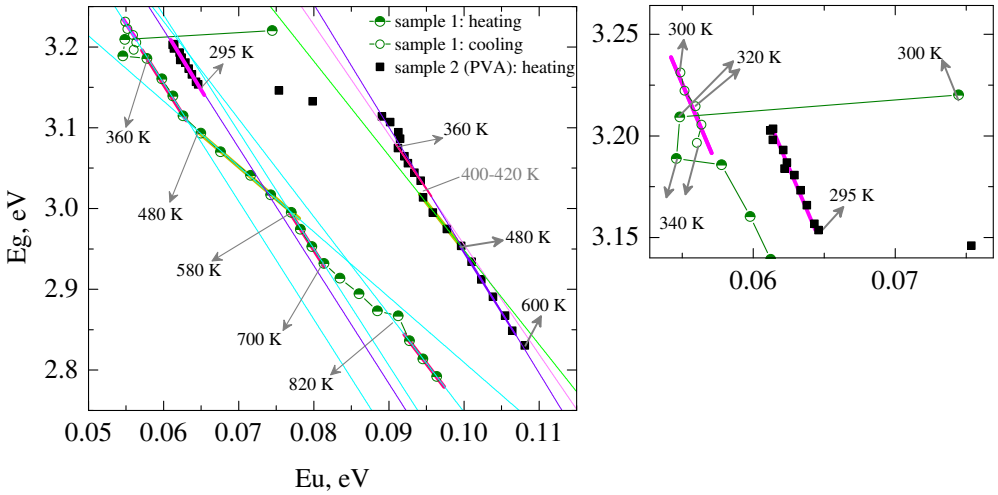

Figure 3.16: The Eg - Eu plot for the two $BaSnO_3$ samples

Further, in our fig. 3.16 there seems to be an inflection point at 360 K. This is very close to 375 K, where the change of slope in dielectric data was noticed in [100]. At the same temperature, the mass loss was detected in [101] and was tentatively ascribed to evaporation of physisorbed water.

Next, in our data there is a change of slope at 480 K. This probably corresponds to the end of the mentioned mass loss at 473 K in [101]. Moreover, in [100], at 460 K there is an end of linear region of dielectric spectrum with the following strong non-linear increase of ε.

The following change of slope in our fig. 3.16 is at 580 K. In [45] the decrease of n-type conductivity starts at this temperature, apparently caused by the beginning of oxidation in their oxygen-deficient sample which was previously quenched from 1773 K. To add to the mentioned reference, in [100] the dielectric constant decrease finishes, giving place to a horizontal plateau.

The change of slope of our plot at 700 K could correspond to the beginning of mass loss of multiple carbon species in ref. [101]. Otherwise, 650-670 K is the temperature where the oxidation of oxygen-deficient $BaSnO_3$ finishes, and the conductivity starts to increase again [45]. It is a question whether the process of oxygenation at the surface compensates the dangling bonds which are otherwise taken by carbon, and therefore the two processes are related.

There is a non-linear evolution of our plot until 820 K, and a new linear region starts after that. Despite we have no suggestions for the possible reasons, this change is not unexpected, because the mass loss which starts at around 670 K does not stop before 1173 K according to ref. [101]. In addition, as mentioned, high temperature activates the process of oxygen loss which intensifies with temperature increase [45].

As for sample 2, the critical points at 300 K, 360 K, 480 K, and the slight deviation at 600 K coincide with those ones in sample 1. The further characteristic temperatures cannot be verified since 600 K is the upper limit of the experimental temperature range.

Conclusions

The optical absorption was measured on $BaSn_xTi_{1-x}O_3$ powders by UV-visible-NIR absorption spectroscopy.

According to the shape of the measured spectra, the Eg levels of Sn and Ti exist separately, but the lower-energy levels cannot be distinguished, so probably they hybridize together. Despite the fact that the band gaps of $BaTiO_3$ and $BaSnO_3$ are very similar, the band gap increases until x(Sn)=0.8 by more than 0.35 eV, and then decreases. Since the band gap Eg plotted against Urbach energy Eu shows two separate regions as well, we deduce that the disorder should be responsible for the band gap increase. Moreover, there is a low-energy shoulder on the Urbach plot in compositions x(Sn)=0.1...0.6 which is probably due to some components of disorder.

We also studied the optical properties of some compositions in temperature. From complementary plots Eg=f(T) and Eg=f(Eu) the phase transition temperatures can be extracted, as well as the changes of the disorder state in a wider range around the phase transitions in ferroelectric and relaxor compositions (fig. 3.17). The T of phase transitions and the Td agree well with XRD and T_{CW}. For x(Sn)=0.1, there are two disorder states existing in the region of diffuse phase transition, one related to process happening below Tm, and the second one - up to T_{CW}. For x(Sn)=0.2, two characteristic temperatures are also visible, and the Td is confirmed. For $BaSnO_3$, the temperature points in fig. 3.17 characterize the changes of defect state. As for x(Sn)=0.5, unfortunately we are not able to make any hypothesis because of the non-coinciding temperature ranges of previous experiments. A deeper insight would need more experiments.

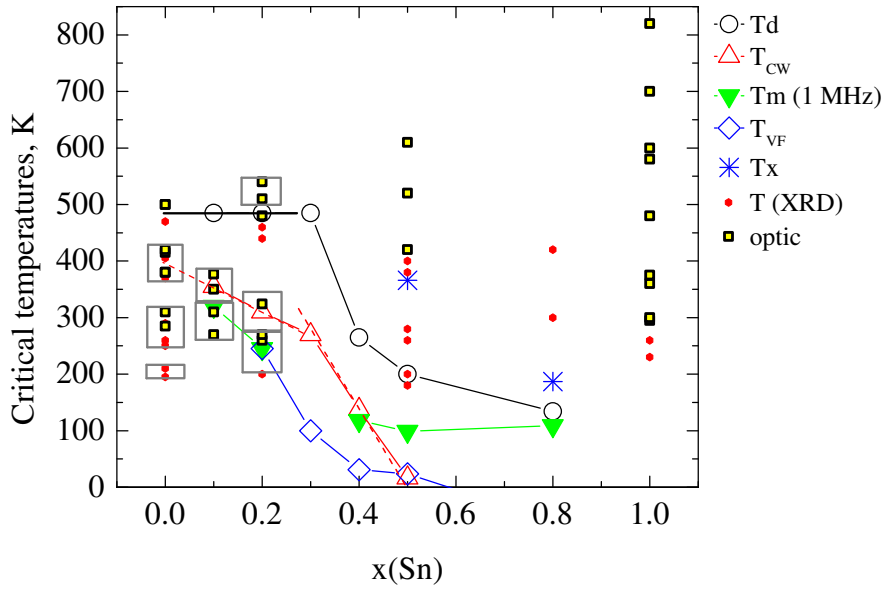

Figure 3.17: The combined plot with characteristic temperatures from dielectric, XRD, and optical characterization

Chapter 4

Chemical bonding at the atomic level

4.1 Methods and review

4.1.1 Raman spectroscopy

4.1.1.1 Introduction

This chapter presents the results of two spectroscopic techniques, Raman spectroscopy and X-ray photoelectron spectroscopy. These techniques allow to analyse local properties of matter. Raman spectroscopy, applied to crystalline materials, allows recording a phononic fingerprint of the material under study, which can lead to getting information of interatomic force constants, potentials, and local structure anisotropy. Only the phonon modes which cause the polarization of electronic clouds are active in Raman, or in other words those modes which cause the dynamic contribution to atomic charges. We make the bridge to X-ray photoelectron spectroscopy, since this technique also permits to qualitatively compare the atomic charges between different materials. Using these two techniques, we are interested to shine some light on the local chemical binding in $BaSn_xTi_{1-x}O_3$ compounds in connection to the local (static or dynamic) unit cell distortions.

In Raman spectroscopy, the sample probe is the monochromatic light of a laser. The photons can be inelastically scattered with the creation or absorption of a phonon vibration (Stokes process when the scattered photon has less energy than the incident, or Anti-Stokes processes when the scattered photon has more energy than the incident one), the former ones being measured in the present experiments. The scattered phonon, whose energy (wavelength λ_s) is different from the initial one (wavelength λ_i), has the Raman shift (wavenumber) of $\mid 1/\lambda_i - 1/\lambda_s \mid$, which is used as abscissa in Raman spectroscopy spectra representation.

For a phonon to be active in Raman, it should be characterized by a po-

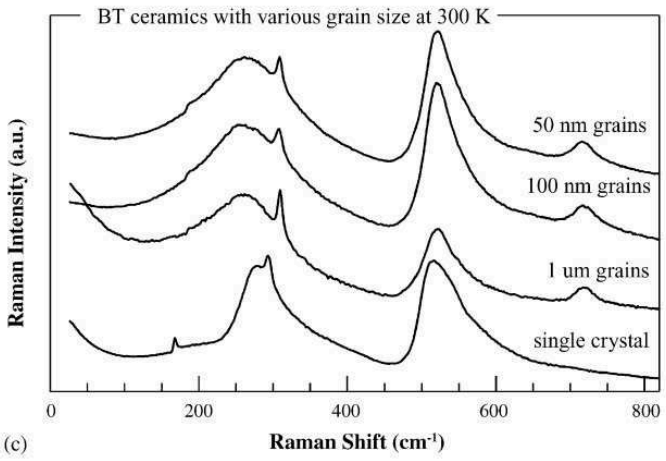

Figure 4.1: Raman spectrum of $BaTiO_3$ ceramics with different grain sizes, as indicated

larization of electronic clouds P as follows:

$$\vec{P} = \alpha \cdot \vec{E} \tag{4.1}$$

with α - tensor of electronic polarizability, and E - electromagnetic field. Only optical phonons are detected. They are separated into longitudinal (LO) or transverse (TO) modes. In LO phonons, the dipole moment is induced parallel to the propagation direction of the mode, and in TO - perpendicular to it fig. 4.2. The interaction with the induced dipole moment causes the splitting of TO and LO modes in energy.

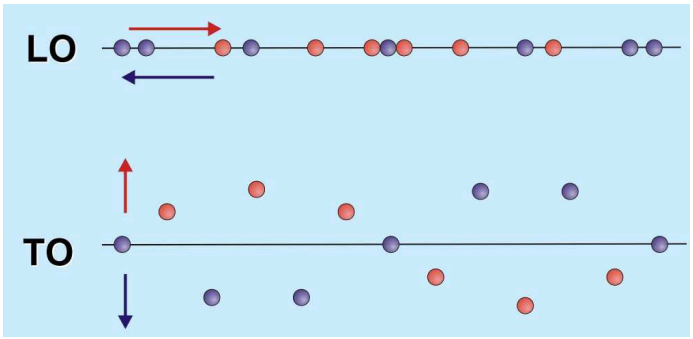

Figure 4.2: Sketch of the difference between TO and LO phonons, the arrows indicate the amplitude of vibration, horizontal lines indicate the propagation direction (time axis)

In ABO_3 perovskites, the modes can involve the vibration of different combinations of atoms fig. 4.3. The type of mode determines the index n in the mode name (LO_n or TO_n). The longitudinal Slater and Axe modes (LO_1 and

LO_3) are connected with the interaction of B-O and B-B pairs, and determine the effective dynamic charges of these atoms. In this way these modes are connected to the short-range and long-range interactions and play an important role in ferroelectricity.

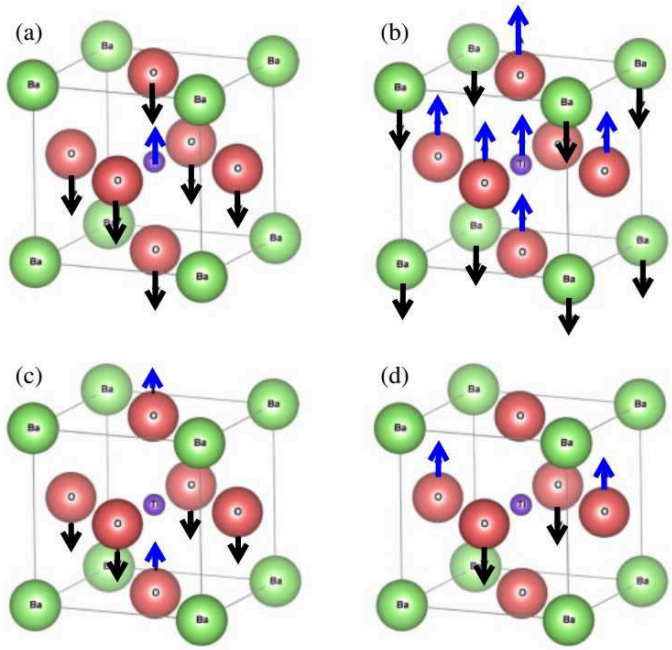

Figure 4.3: The classification of phonons in perovkites [95] depending on the involved atoms: (a) Slater n=1 (b) Last n=2 (c) Axe n=3 (d) O_4 torsional mode, n=4

4.1.1.2 $BaTiO_3$

The TO_1 mode, especially its component $E(TO_1)$ at low wavenumbers (10-50 cm^{-1}) [102, 103], is very important to the phase transitions of $BaTiO_3$. It is a so-called soft mode, whose frequency tends to zero at fully displacive phase transitions. To the contrary, in $BaTiO_3$ this mode never comes to zero at any phase transition [94], because an order-disorder component is also involved [92]. The order-disorder contribution to the phase transition is observed from dielectric experiments. Such mode arises from the hopping of Ti between the eight ground sites where it lies along the <111> directions of the unit cell [89, 92]. This mode is also called a central mode [48]. As shown in fig. 4.4a, the triple degenerate modes soften (decrease in frequency) at each phase transition, and then reappear between 200 and 300 cm^{-1}.

It is claimed that at every phase transition on cooling certain degrees of freedom of Ti hopping are frozen, so the coupling between some components

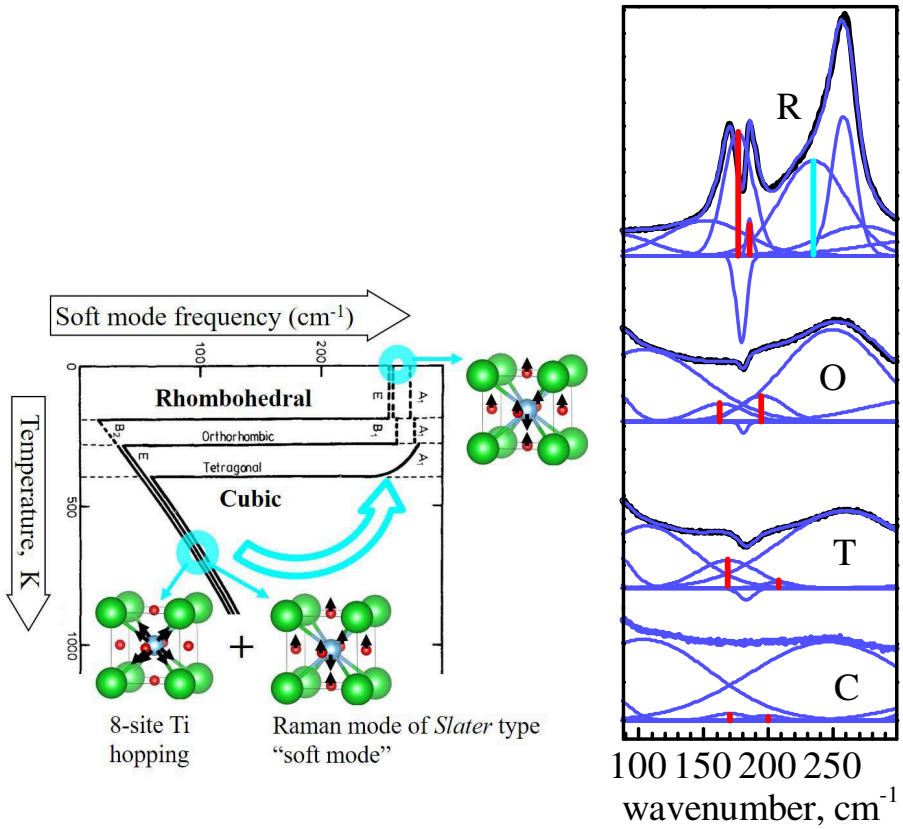

(a) (b)

Figure 4.4: The soft mode in $BaTiO_3$ (a) from neutron scattering [94], (b) in Raman spectroscopy (our data)

of soft mode and the central mode is broken. In the rhombohedral phase of $BaTiO_3$, the low-frequency Raman intensity coming from the soft mode disappears and shifts to the 200-300 cm^{-1} region (fig. 4.4).

The spectrum of $BaTiO_3$ consists of three major groups of peaks (table 4.1) which lie below 450 cm^{-1}, between 450 and 600 cm^{-1}, and 700-800 cm^{-1} (see fig. 4.10).

The low-frequency region is dominated by wide and dampened soft and central modes. Another wide mode $A_1(TO_1)$ strongly influences the shape of the spectra in the 270 cm^{-1} region.

In between those two wide modes, the spectrum is determined by the coupling of multiple modes which form the antiresonance (Breit-Wigner interference) in phases with unit cell distortions [107]. Ref. [108, 105, 109] claims there is a coupling of these modes with disorder, or with polaritons. In the latter case, the coupling with polaritons is studied for modes propagating at

Table 4.1: Raman modes of $BaTiO_3$ [102, 103, 95, 104, 105, 106]

Mode	Peak maximum, cm^{-1}
$E(TO_1)$	38-50
mode *a*: Central mode	100
mode *b*: $A_1(TO_2)$ - $E(TO_1)$	154
mode *c*: LO_2, TO_2 - $E(TO_1)$	$\sim$ 180-190
rhombohedral $E(TO_1)$	250
$A_1(TO_1)$	260-270
TO_4, TO_2	300-307
$E(LO_4)$	465
$A_1(LO_1)$	470
$E(TO_3)$	490
$A_1(TO_3)$	512
$E(LO_3)$	706
Oblique mode $A_1(LO_3)$-$E(LO_3)$	716
$A_1(LO_3)$	730

some angle to the crystallographic axes, i.e. oblique polaritons. In ref. [110] it is speculated that at slight deviations from the center of the Brillouin zone, the shape of 100-300 cm^{-1} region could be either due to large first-order coupling between electron and phonons (polaritons) or due to the interaction between first-order phonons and second-order background. The oblique Raman modes are discussed more in detail in [102, 103]. There is high probability that the modes at 150-195 cm^{-1} and 716 cm^{-1} are oblique (see table 4.1). The possibility of capturing the oblique Raman modes during the measurement is rather high for ceramics, since the grains are oriented differently. We will consider this hypothesis for the identification of modes in our samples.

The special feature of the $BaTiO_3$ spectrum is the wide asymmetric shape of $A_1(TO_1)$ at 260 cm^{-1}, A_1TO_3 at 512 cm^{-1}, and the $A_1(LO_3)$ (with possible mixture of $E(LO_3)$ character) at 716 cm^{-1}. The reason for that is the complicated coupling between the modes and the disorder.

In addition to the mentioned modes, the wide smeared mode at 600-620 cm^{-1} can appear depending on the sample. In general, it is often seen in ceramics or powders with submicron grains. In bulk $BaTiO_3$, this mode appears at the pressure of 4-6 GPa in the cubic phase. It is probably connected with the disordered paraelectric phase appearing at the grain boundaries [111, 107].

4.1.1.3 $BaSnO_3$

$BaSnO_3$ is a cubic compound, so ideally first-order Raman is not allowed by selection rules. Nevertheless, the spectrum with well defined modes is

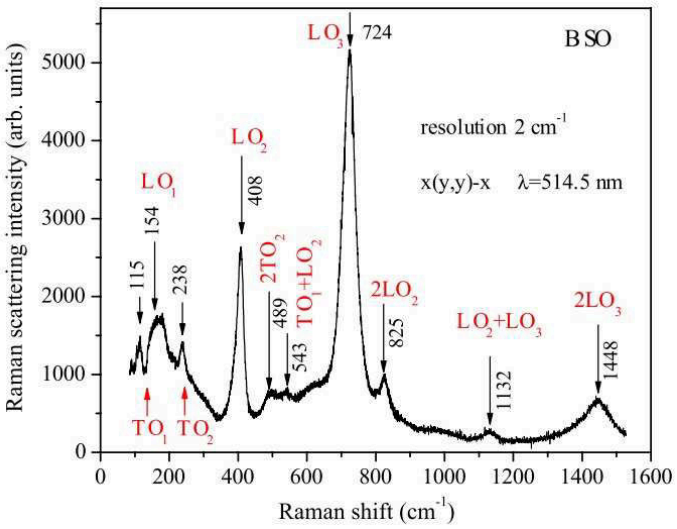

Figure 4.5: Raman spectrum of $BaSnO_3$ [59]

observed in Raman measurements, even if its intensity per second of acquisition is much lower than the $BaTiO_3$ spectrum. It was claimed that those could be second-order Raman peaks, or that the first-order effect appears due to defects locally breaking the symmetry, despite the so-called F_{2U} mode was predicted by calculations [112]. Another possible reason for that could be that in $BaSnO_3$ the $Pbnm(Pnma)$ orthorhombic structure with oxygen octahedra rotations is very close in energy to $Pm\bar{3}m$ [58, 59], so that alternative phonon modes characteristic for $Pbnm$ symmetry could exist in $BaSnO_3$. In fig. 4.5 the modes were indexed according to the changed Brillouin zone of orthorhombic phase where first-order modes are allowed.

4.1.1.4 Solid solutions

For solid solutions, the convention will be to add * symbol to mode symmetry, to note that it might be changed if the local distortions are different from tetragonal ones as in room temperature $BaTiO_3$. We keep the original symmetry notation just to distinguish between different components of same mode.

In the solid solutions $BaSn_xTi_{1-x}O_3$ the spectrum keeps the features of $BaTiO_3$, but the modes become wider, fig. 4.6 [34, 113]. The shape of the 150-200 cm^{-1} region changes: the antiresonance disappears (or moves to lower wavenumbers in the Raman spectrum with λ=514 nm) and two peaks appear instead [113]. In similar solid solutions $BaZr_xTi_{1-x}O_3$, such a shape and the appearance of mode ∼110-130 cm^{-1} is associated with the local distortions of orthorhombic or rhombohedral character [114, 115]. Except in $BaZr_xTi_{1-x}O_3$, it has been evidenced in single domain $BaTiO_3$ thin film Raman spectra with

rhombohedral nanoregions [116], disordered solid solutions (Ba,Sr)TiO_3 [117], amorphous $BaTiO_3$ [118], and is proved to be a component of $A_1(TO_1)$ mode coupled with Debye mode (Ti hopping) [119, 92]. As well, this mode is suggested to be of Slater character according to the frequency and the mass ratio of Zr/Ti [114].

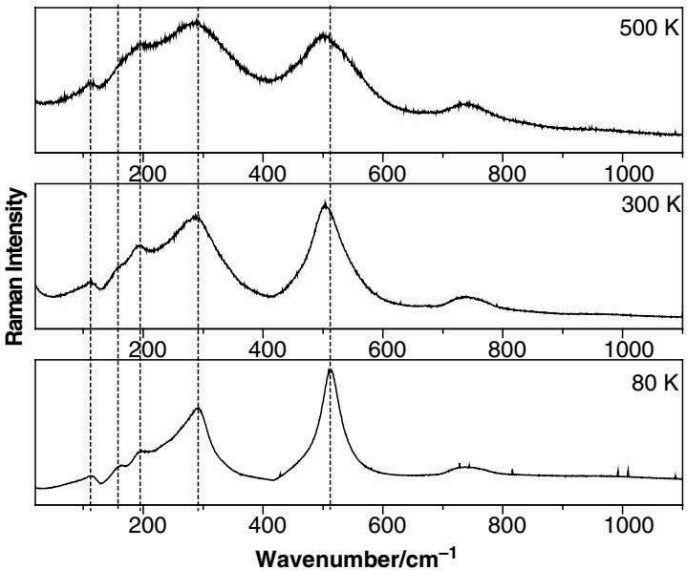

Figure 4.6: Raman spectra of $BaSn_xTi_{1-x}O_3$ with x(Sn)=0.3 [113]

The temperature studies of the $A_1^*TO_3$ peak in x(Sn)=0.3 showed that from Raman spectroscopy it is possible to find (from the presence of several linear regions in peak centers and the integrated intensity) the sequence of relaxor phases and the critical temperatures of phase transitions. The phase sequence is slightly different from the one obtained by dielectric spectroscopy in [43]. It is proposed that the phases (in the order of temperature increase) are non-ergodic relaxor, 100 K<T<200 K mature ergodic phase, 200 K<T<450 K ergodic polar cluster phase, T>450 K paraelectric phase fig. 4.7. In dielectric spectroscopy, no differentiation between mature ergodic phase and polar cluster phase was made.

In this chapter we are discussing the Raman data on other compositions of $BaSn_xTi_{1-x}O_3$ in the same frame, making references to other chapters.

4.1.1.5 Experimental details

The micro Raman spectra were acquired from ceramic pellets to reproduce XPS data using a Labram-Horiba spectrometer with He-Ne laser (632.8 nm) through an optical microscope and typically using 50X objective. Fityk software was used for fitting. For enhanced comparison of $BaTiO_3$ features with our solid solutions, $BaTiO_3$ sample was measured at temperatures 100-700 K

and fitted within the same procedure after correction for Bose-Einstein population factor. We used the mathematical correction by negative Gaussian peak for the antiresonance in the 180 cm^{-1} region.

4.1.2 X-ray photoelectron spectroscopy

In laboratory based X-ray photoelectron spectroscopy, the monochromatized X-ray beam, generated with an X-ray source (typically aluminium), illuminates and is absorbed by the material. The transition to the ground state is accompanied by different desexcitation events, among others the generation of electrons (so called photoemitted electrons) fig. 4.8.

The hemispherical analyser with potential applied to it is used to separate the photoelectrons by their kinetic energy K.E. The binding energy B.E. is then recalculated as follows:

$$B.E. = h\nu_{XR} - K.E. - \phi_{sp} \tag{4.2}$$

with $h\nu_{XR}$ - energy of X-ray, ϕ_{sp} - potential of spectrometer. Normally, the sample is electrically grounded, and the calibration is made with a standard, so that the potential of the spectrometer does not contribute to the peak position and the Fermi level is at the zero binding energy (see the red arrow in fig. 4.8b). By convention, the scale is normally inverted with "zero" on the right. If the value of the electronic level energy is small, the $h\nu_{XR}$ is enough to excite the electron to the Fermi level or to the vacuum level energy. The deeper in energy is the core level, the less will be the kinetic energy of the electron, larger than the B.E..

The semiconductor valence band (VB) appears in the spectrum at some energy below the Fermi level, and at some distance from the VB there are peaks corresponding to core levels or Auger processes which will not be discussed here.

4.1.2.1 Measurement details and framework of analysis

Because the electrons are extracted from the sample, it needs to be not only grounded but also well-conductive, otherwise it charges positively, and the peak positions and shape change. If a sample with low conductivity has to be studied, as it is the case in our work, it is possible to compensate the charging by using an electron gun. The intensity of the electron flow is chosen to shift the peak of the surface carbon C 1s close to its usual position, nevertheless the absolute values of the peak positions and the valence band maximum cannot be trusted because C 1s binding energy can be influenced by different interface charge distribution phenomena and C is not part of the perovskite unit cell.

In our study, we want to make the comparative qualitative analysis of the peaks. Since the absolute position is not available, we take the difference between the Ba 3d 5/2 and other levels, since Ba is present in all the samples

and is supposed to be least influenced by Ti substitution fig. 4.9. One of the reasons is that the Born charge of Ba in $BaTiO_3$ and $BaSnO_3$ was calculated to be very close (+2.73 in and +2.74) [88, 120]. Note that we can distinguish contributions to Ba 3d 5/2 peak from the bulk and surface carbonates.

It is clear that in a first approach in XPS the closest electronic levels to the nucleus have larger value of binding energy. Outer orbitals have smaller value of B.E., because the Coulomb interaction between them and the nucleus is screened by electrons from deeper levels. For the same bond between metal atom and oxygen M-O, metal M electronic levels which are less oxidized/equivalently, more reduced are shifted to the smaller B.E. values. In our case, cannot evaluate the absolute values of B.E. as there is no absolute Fermi edge allowing us to define the energy reference. On the other hand, we analyse the B.E. difference between Ba 3d 5/2 (with its B.E. fixed according to calibration) and core levels of other atoms. Therefore the value of this difference will account for different atomic and electronic factors, including the average charge of the metal ion M and the bond length itself. In this work in Ba-perovskites, we consider the Ba 3d 5/2 B.E. level as constant. In addition to changes of valence state, the more intricate chemical shift could come from the property of the bond itself, such as the degree at which the electrons are localized at the atoms, or the covalency/ionicity of the bond:

$$\Delta B.E.(3d) = -\Delta\epsilon - \Delta E^{XPS}_{relaxation}(3d) \tag{4.3}$$

with ϵ - the variation of Koopman's energy (energy of monoelectronic orbital), and $\Delta E^{XPS}_{relaxation}(3d)$ - variation in the extra-atomic relaxation energy corresponding to a hole in the given shell [121]. Although this dependency is deduced for monoelectronic orbitals, we can use it as a first approximation to be applied to the different core levels under study in our compounds. Therefore the extra-atomic charge has an important effect on the B.E., this effect can be imagined as outer charge screening of the core levels.

In the bond M-O the $\Delta B.E.$ is larger for a higher degree of ionicity (smaller Madelung potential) for the case of binary oxide Y_2O_3 [121]. However, in our case there are three pairs of such M-O bonds (Sn-O, Ti-O and Ba-O), so the charge transfer from one bond to another is possible, and care should be taken about the more complicated charge distribution.

The information on differences of the chemical bonding can be also extracted from Auger lines. For instance, the difference between $OKL_{23}L_{23}$ and OKL_1L_{23} is larger for the bond which is more covalent [121], because the different orbitals of the same atom are influenced in a different way by the distribution of electronic charge of the chemical bond.

In our experiment, we performed XPS on ceramic pellets, polished for ease of focusing. An axis Ultra DLD spectrometer with monochromatic Al $K\alpha$ X-ray source together with a charge compensation electron gun were used.

4.1.3 Connection between XPS, phonons, and the band gap

There is an important connection between the two techniques. we have included in the results of this chapter, i.e. XPS and Raman spectroscopy.

In theoretical works, a lot of different definitions of effective charge exists to answer the question of whether the charge of an atom is localized/delocalized, static or dynamic etc [120, 36]. Nevertheless, in general the more accepted approach is based on using a standard quantity called the Born charge. It is defined as the change of polarization P_β per unit cell along the β direction for the displacement of the atom i in direction u.

$$Z^*_{i,\alpha\beta} = \frac{\delta P_\beta}{\delta u_i, \alpha} \tag{4.4}$$

with u_i, α - the components of displacement.

The polarization P_β includes both the components of atomic rigid displacement and the charge transfer in the electronic clouds. In a crystal, this dynamic charge transfer contributes importantly to the properties of chemical bond and thus to the phonons that are related to the change in the polarizability.

The Born charge values for the different ions in $BaTiO_3$ and $BaSnO_3$ are given in table 4.2. It is remarkable that for $BaTiO_3$ the values are very much different from the chemical valence values due to the dynamic hybridization in Ti-O chains which are introduced by certain phonon modes [36, 120]. Note that the $O_\parallel$ Born charge is more different from the value of chemical valence than the corresponding one from $O_\perp$. In general, Z^* strongly depends on the electronic distribution leading to the creation of a dipole within the Ti-O bond, and thus of an atomic distortion in other words on the kind of unit cell distortion.

Table 4.2: Born charges of parent compounds of $BaSn_xTi_{1-x}O_3$ [88]

Compound	Z^*_{Ba}	Z^*_B	$Z^*_{O\parallel}$	$Z^*_{O\perp}$
$BaTiO_3$	+ 2.73	+ 7.52	-5.88	-2.15
$BaSnO_3$	+ 2.74	+ 4.38	-3.35	-1.88

Most probable phonon modes to modify the effective charge distribution are probably Slater or Axe modes, since they involve movements of Ti against O. Changing the Born or effective charges, the nature and energy position of the valence band maximum and the conduction band minimum can also be changed. As a result, there might be a connection between the Raman mode characteristics and the band gap in the different Born charges, as it will be mentioned in the discussion of the results.

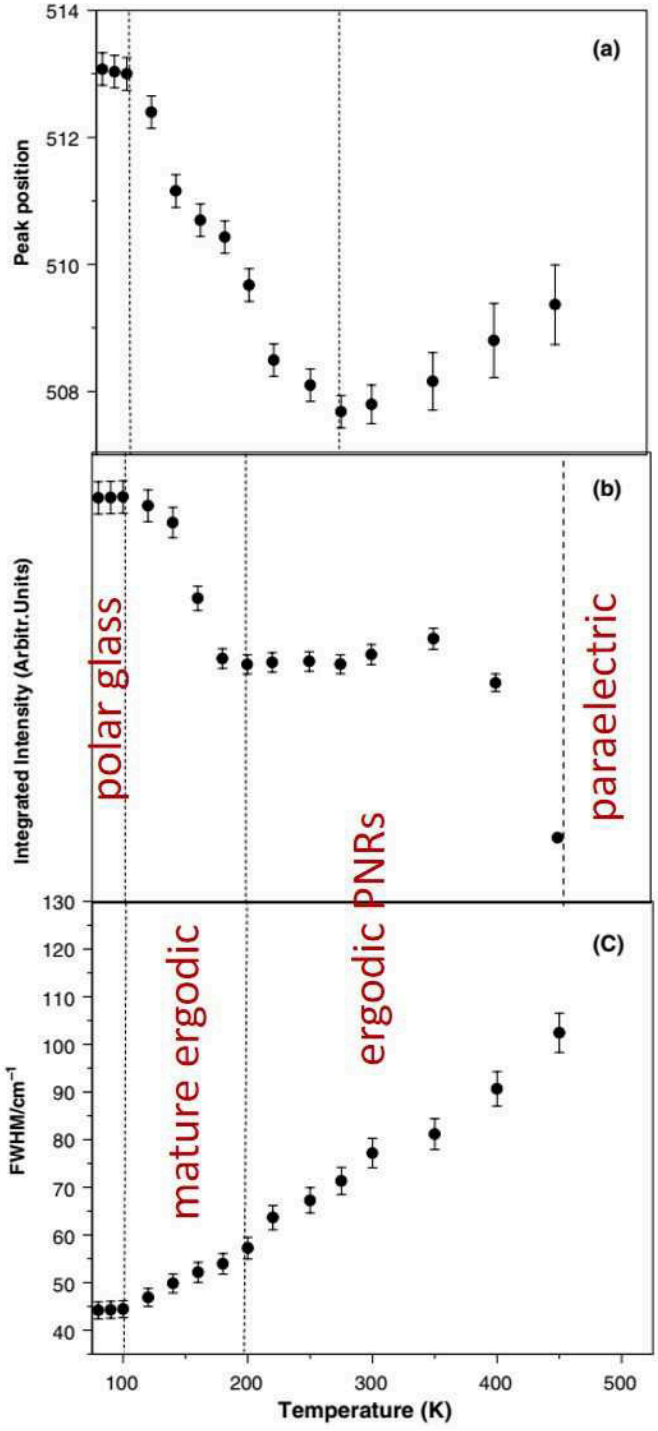

Figure 4.7: Study in temperature of $A_1^*TO_3$ mode fit parameters in $BaSn_xTi_{1-x}O_3$ with x(Sn)=0.3. Note the different critical temperatures in the peak centers and the intergrated intensity [113]

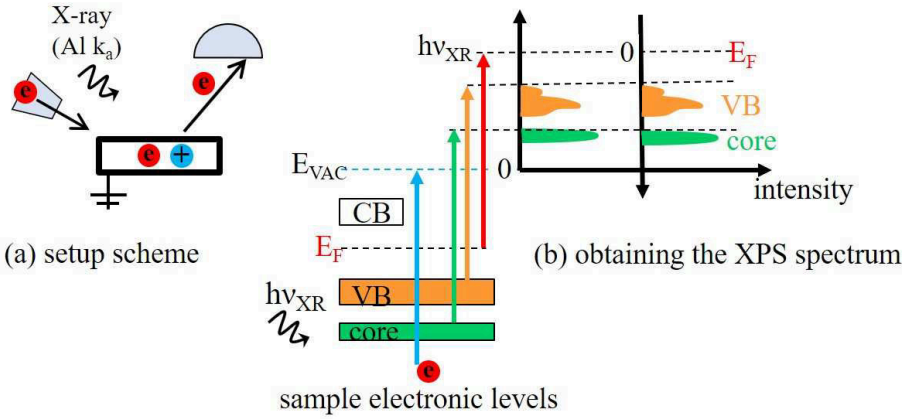

Figure 4.8: X-ray photoelectron spectroscopy: (a) measurement scheme, with $h\nu_{XR}$ - the X-ray energy; and (b) the relation between the electronic bands and the XPS spectrum

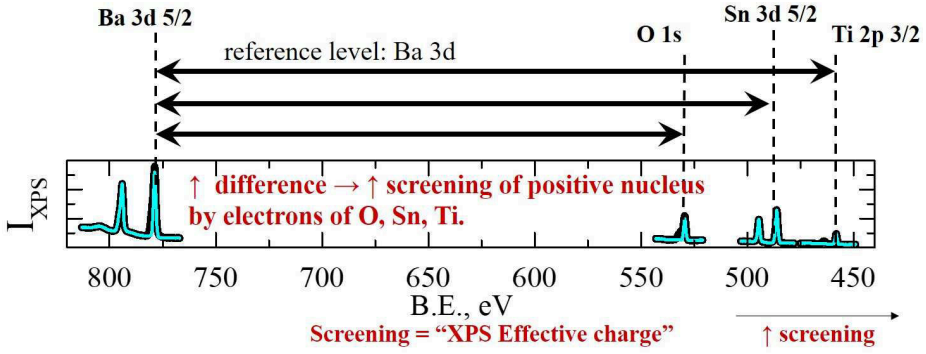

Figure 4.9: The difference between the reference energy level Ba 3d 5/2 and other levels - the parameter used for analysis of our XPS data

4.2 Results

4.2.1 Raman spectroscopy

4.2.1.1 $BaSn_xTi_{1-x}O_3$ at 293 K

The Raman spectra of $BaSn_xTi_{1-x}O_3$ collected at room temperature are represented in fig. 4.10. A first inspection of all the spectra indicates that they keep a similar shape to the one of $BaTiO_3$, and only the pure $BaSnO_3$ has a very different shape. Based on that, we propose that the Ti sublattice defines the Raman spectra for solid solutions. Additionally, for the same acquisition time, Sn-rich samples have much lower intensity than Ti-rich ones, in agreement with pure $BaSnO_3$ being a cubic phase where macroscopic first-order Raman activity is ideally not allowed.

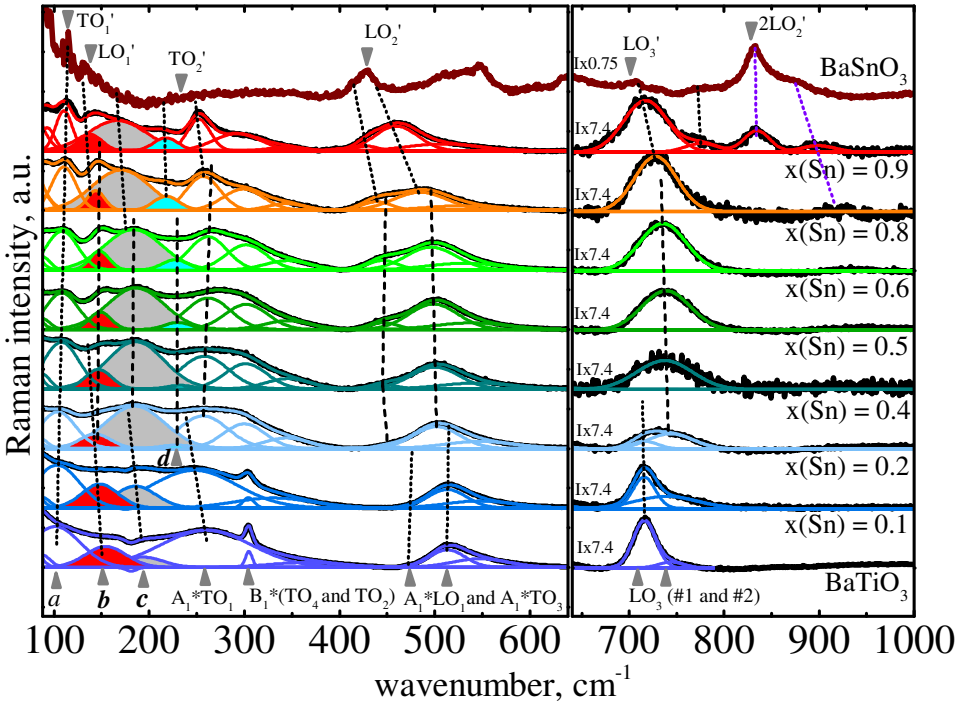

Figure 4.10: Raman spectra at room temperature for $BaSn_xTi_{1-x}O_3$ with different Sn ratio

If we concentrate on the high wavenumber region (> 650 cm^{-1}), one can see that the initial LO_3 peak, remanent of $BaTiO_3$, becomes weaker and disappears beyond x(Sn)=0.2. Meanwhile, a new hardened Axe LO_3 mode grows at larger frequency (737 cm^{-1}), next to the LO_3 (E-A_1) oblique mode characteristic of tetragonal $BaTiO_3$, which have smeared out due to the new chemical bonds and unit cell change introduced by the Sn-substitution. Remarkably, it is the only mode starting from x(Sn)=0.4 until x(Sn)=0.8. This mode is known to be

characteristic in relaxors, including the similar system $Ba(Zr,Ti)O_3$ [114, 115]. In x(Sn)=0.9, new peaks appear which are characteristic and common to some of the modes seen in pure $BaSnO_3$.

The positions of LO_3 mode(s) are plotted in fig. 4.11a. One can see that for the high-frequency mode there are two linear regions, which intercept at x(Sn)=0.75. In $Ba(Zr,Ti)O_3$, this composition corresponds to percolation limit of Ti, so that further compositions represent the separate Ti-rich clusters which are surrounded by paraelectric matrix [115]. This is in agreement with the new modes characteristic of pure $BaSnO_3$ appearing in x(Sn)=0.9, although other potential cause for this effect could be the existence of a phase separation. We cannot simply distinguish one from another from Raman spectroscopy and further experiments, including synchrotron radiation diffraction, are needed to answer to this question.

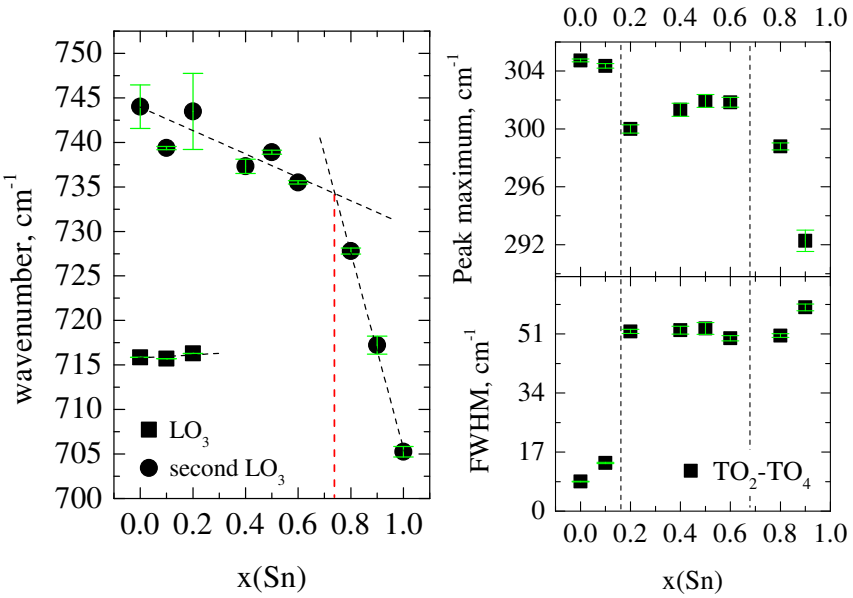

Figure 4.11: Some of the fit parameters plotted against composition: (a) peak maxima of LO_3 modes in 700 cm^{-1} region; (b) the TO_2-TO_4 mode (remanent from B_1 in $BaTiO_3$). Error bars are shown in green.

In the part of the spectra at lower frequencies (< 650 cm^{-1}) in fig. 4.10 three compositional regions of the phase diagram are as well visible.

Below x=0.2, there is a significant softening of the Slater mode $A_1^*(TO_1)$ at 260 cm^{-1} which occurs as for the soft mode of $BaTiO_3$, i.e. due to the decrease of the ferroelectric distortion and unit cell approaching quasicubic shape at around 11 % [122, 123]. Besides, modes *b* and *c*, and LO_3 are softened inside the first compositional region because of their coupling to the soft mode.

Despite the fact that the antiresonance close to mode c disappears already in x(Sn)=0.1, similarly to cubic $BaTiO_3$, the $B_1^*(TO_4\text{-}TO_2)$ mode does not disappear fully but is widened, indicating probably the simultaneous presence of differently distorted polar nanoregions in relaxors or a change in the unit cell that could be compatible to a lower symmetry unit cell. Its center and FWHM are plotted in fig. 4.11b, and can be separated into three different compositional regions. The width of this mode stays approximately similar within the relaxor region, and further increases for x(Sn)=0.8 and 0.9, changing into a wide feature fig. 4.10 which is not fitted in $BaSnO_3$.

For relaxor compositions, there is as well a change in relative intensity of modes b and c. While in tetragonal $BaTiO_3$ phase the mode b is more intense than the mode c, it is to the contrary starting from x(Sn) = 0.2, resembling the orthorhombic phase of $BaTiO_3$ (see fig. 4.4). The intensity ratio $I(b)/I(c)$ is shown in fig. 4.12a, where we can clearly separate this $I(b)/I(c)$ ratio into two regions where this ratio behaves linearly on composition - ferroelectric ones against the rest of compositions. Based on this, we can make the hypothesis that there could exist orthorhombic distortions in the Ti-rich clusters of compositions x(Sn)> 0.2. Another important characteristic of relaxor phases is

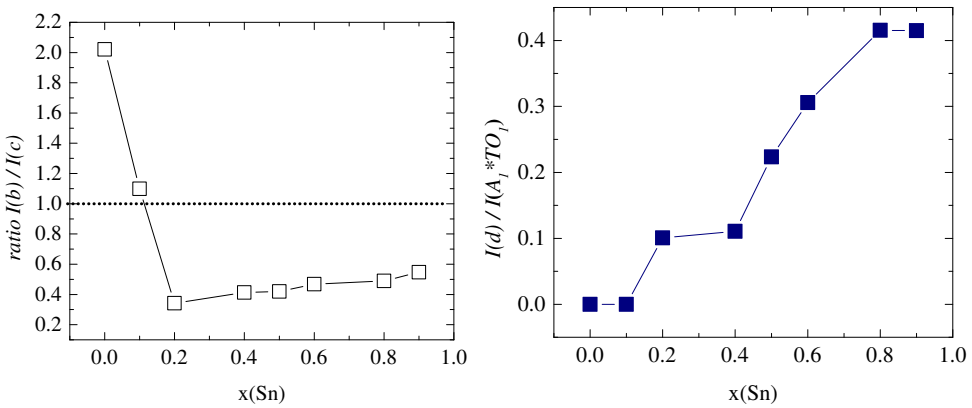

Figure 4.12: (a) the intensity ratio $I(b)/I(c)$, corresponding to different coupling of Last mode and soft mode; (b) the intensity ratio $I(d)/I(A_1^*TO_1)$

the presence of mode d, appearing at 232 cm^{-1} in x(Sn) = 0.2 and becoming stronger for Sn-rich compositions. This mode appearing in $BaTiO_3$ spectrum is the characteristic feature of rhombohedral phase (see fig. 4.4 and discussion of fig. 4.4a), evidences the de-coupling of all the components of Slater E^*TO_1 from the eight-side hopping. The fact that the coupling disappears in our spectra can be further proved by the drastic decrease of width of $A_1^*TO_1$ mode at 260 cm^{-1} fig. 4.13a. Importantly, the widening of this mode in $BaTiO_3$ is claimed to happen due to bond and/or chemical coupling to disorder. Addi-

tionally, the mode b width also decreases (fig. 4.13b). Returning to analysis of mode d and the detailed view of rhombohedral distortions, the intensity ratio $I(d)/I(A_1^*TO_1)$ is shown in fig. 4.12b.

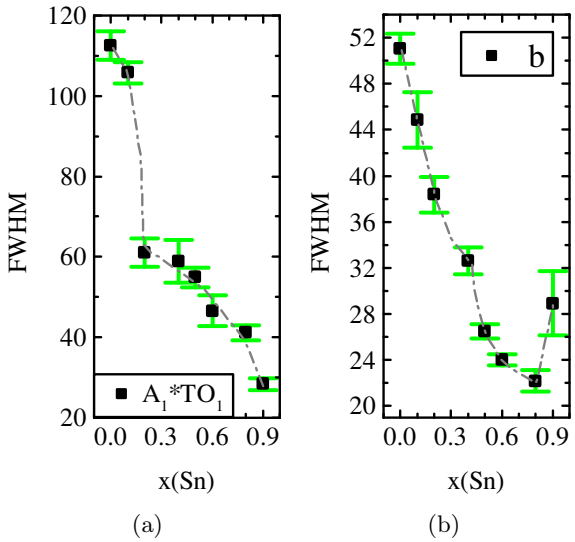

Figure 4.13: The FWHM of (a) $A_1^*TO_1$; (b) mode b. Error bars are shown in green.

There is a plateau for x(Sn)=0.2 and 0.4, and starting from x(Sn)=0.5 $I(d)/I(A_1^*TO_1)$ increases strongly until x(Sn)=0.8. This might be the indication of the further increase in rhombohedral distortion value in the relaxor compositions. This is in agreement with the trend evidenced for Sn-poor compositions x(Sn)=0.16-0.4 by [36] and our own study (see Chapter 2). The ratio stays unchanged for x(Sn)=0.8-0.9. Probably, this is because above the percolation limit the Ti concentration inside the PNR does not change, so that the chemical stress stays the same, and the Ti displacements as well.

Thus, we can conclude that compositions in the relaxor region of phase diagram demonstrate both orthorhombic and rhombohedral local distortions, with increasing tendency towards latter ones, unlike it was deduced before from Raman spectra without fitting procedure [34].

4.2.1.2 Connection between phonons and optical properties in $BaTiO_3$

It was discussed in introduction to this Chapter that certain phonon modes which cause the Ti electronic clouds polarization along Ti-O bonds (Slater or Axe modes) can participate in the creation of dynamic hybridization of bonds (corresponding to dynamic component of effective charge) and in this way to modify the band gap. The band gap change at the ferroelectric transition of

$BaTiO_3$ was measured in several references [74, 86, 84] fig. 4.14. It is speculated that phonon driving the optical response is probably not the soft mode transverse Slater phonon A_1TO_1. Here we present our Raman data acquired in temperature to analyse the changes of the polar state and the possible connection to the band gap change we have determined.

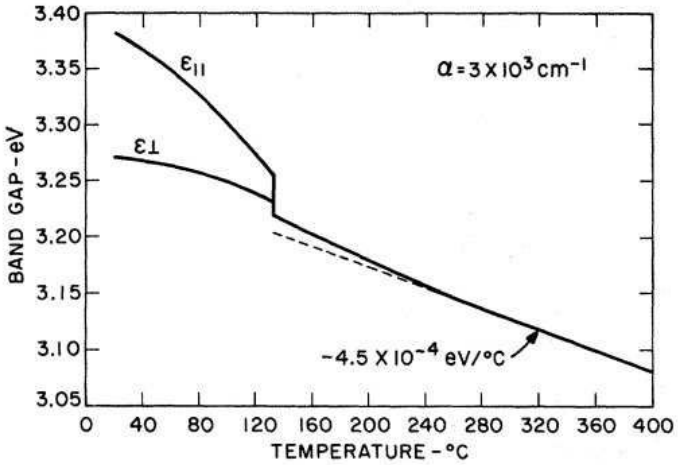

Figure 4.14: The band gap of $BaTiO_3$ at the T-C phase transition

The A_1TO_1 mode positions in temperature are plotted in fig. 4.15. The corresponding Raman spectra for $BaTiO_3$ are presented for completitude in Annex B, as well as for several other compositions. In agreement with [104], there are the discontinuities in peak centers at the phase transitions according to the mode softening close to the different phase transitions on heating, and the new hardened mode appearing above the ferroelectric transition temperature.

However, there are no discontinuities in the band gap of the $BaTiO_3$ annealed powder in fig. 4.16.

In agreement with speculations in references, there seem to be no direct connection between A_1TO_1 mode positions and the band gap. On the other hand, the A_1TO_3 mode seems to evolve in a way which is related to the band gap. All the three phase transitions are accompanied by the corresponding steps on both Raman and the band gap data. Therefore we conclude that in $BaTiO_3$ it is the Axe mode which is indicative of the change in the orbitals determining the band gap.

It is known that the static distortions cause the deviation of the Ti-O-Ti bond from 180° and the change of orbital overlap (fig. 4.17) [66, 67]. Whether the B site atom orbital is Sn 5s or Ti 3d t2g (orbital forming the conduction band minimum in parent compounds of our solid solutions), the distortion promotes the increase of antibonding character of the chemical bond. As a result, the conduction band minimum shifts to higher values in energy, and

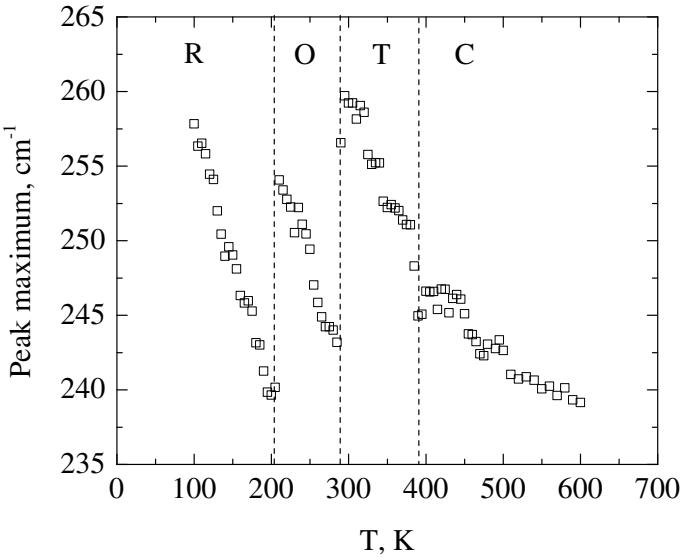

Figure 4.15: The temperature dependence of Raman A_1TO_1 mode deduced from the peak maximum position

the band gap increases.

For the atomic displacements of Axe TO_3 mode and the transverse band gap $Eg_\perp$ a very similar mechanism is involved (fig. 4.18). It is clear from fig. 4.14 that the lowest band gap we are measuring is of transverse nature and the interaction involved should be happening along the bonds parallel to XY plane. When four oxygen atoms lying in this plane vibrate against Ti, the alternation of $pd\pi$ bond overlap is happening. This is the type of bond which defines the conduction band minimum in $BaTiO_3$ according to LCAO and calculations [124], so eventually the band gap is directly connected with this type of phonon, in agreement with the prediction [74].

4.2.1.3 Connection between phonons and optical properties in x(Sn)=0.2

We try to analyse the Raman spectra in the same framework as $BaTiO_3$. In fig. 4.19 one can see the examples of fits for different temperatures. The maximum of the peak in 500 cm^{-1} region is in all compositions defined by the mode which arises from the A_1*(TO_3) in $BaTiO_3$.

In x(Sn)=0.2, at low temperature both peaks A_1*(LO_1) and E*(TO_3) are present. However, at higher temperatures ($>$ 280 K) the E*(TO_3) disappears, and simultaneously there is a steplike increase in intensity and width of a Gaussian peak at 550 cm^{-1} which models the asymmetric tail in the high frequency side due to mode coupling to disorder. These changes are similar to the ones happening in $BaTiO_3$ at the R-O phase transformation fig. 4.20, and

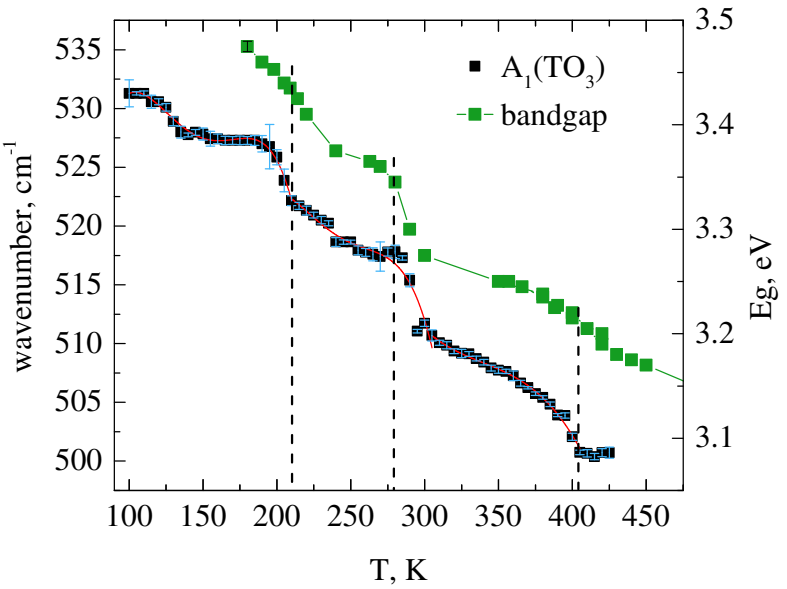

Figure 4.16: The connection between temperature dependences of A_1TO_3 Raman mode and band gap for different phases of $BaTiO_3$ (error bar for the band gap is smaller than the symbol size)

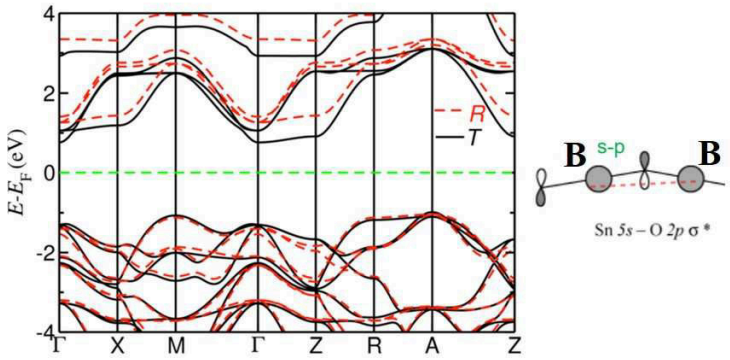

Figure 4.17: The changes of electronic structure (band gap increase) under static distortions of $BaTiO_3$ unit cell due to deviation of B-O-B bond from 180° and the change of orbital overlap (illustrated for $BaSnO_3$ on the right) [66, 67]

probably they mean that the $E^*(TO_3)$ is the indicator of a symmetry change at (R-C or R-O) transition.

In 700 cm^{-1} region of x(Sn)=0.2, the low-frequency component of LO_3 decreases its intensity at 260-280 K, and the high-frequency component which is characteristic of relaxor phase becomes more intense. These changes are illustrated in fig. 4.21 through the ratio of intensities of these two modes

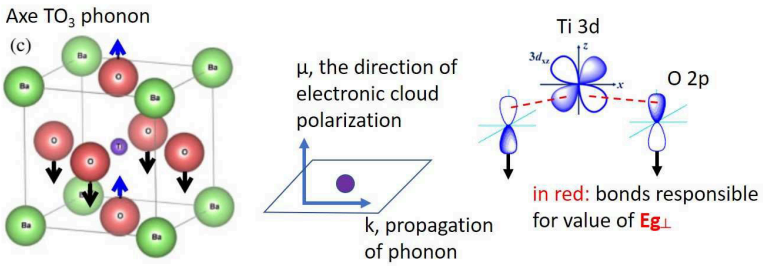

Figure 4.18: The coupling of Axe TO_3 phonon and the band gap

$I(LO_3)_{FE}/I(LO_3)_{relaxor}$.

Figure 4.22a shows the centers of all the peaks in 450-750 cm^{-1} region. Starting from the low temperatures, the first point to note is that at 200 K the decrease in frequency of the mode at 640 cm^{-1} which is associated to disorder at grain boundaries in pure $BaTiO_3$. Therefore, this critical point is probably associated with the disorder.

In parallel, at 200 K the E*(LO_1) reaches the maximum of frequency. Despite in dielectric properties no characteristic features are observed at these temperatures from the XRD patterns at 200 K, there is a change of trend of the studied d_{200} distance (fig. 2.18).

Upon the increase of temperature, the peak at 640 cm^{-1} keeps constant frequency and then disappears between 240 K and 260 K. We speculate that between 200 K and 260 K there is a continuous process happening which leads to diffuse phase transition evidenced from dielectric spectroscopy (fig. 1.13) peaking at Tm=240 K.

At Tm, according to what was discussed about the E*(TO_3) mode disappearance (fig. 4.19), the local symmetry seems to change from rhombohedral to orthorhombic. This may be in agreement with the spectrum of x(Sn)=0.2 at 293 K, where the presence of orthorhombic phase is evidenced in fig. 4.10, while the mode d appears but its intensity is low fig. 4.12b.

Between 320 K and 340 K another significant change occurs in Axe LO_3 mode in 700 cm^{-1} region. Instead of two separate LO_3 peaks, one characteristic for ferroelectric phase and another for relaxors, at 340 K there is only one component. Since the position of its center does not evolve continuously, probably this change means that the anisotropy related to certain type of distortion disappears at this temperature. From fig. 1.13, this is where the T_{CW} lies, which probably means that the diffuse phase transition is finished and the macroscopic ferroelectric phase disappeared. Nevertheless the PNRs and dynamic polar correlations could still exist.

The peak of 600 cm^{-1} (fig. 4.22) reacts to every of the dipole state changes which are visible in other peaks. At 480 K there is a new shift of this peak happening after the previous stabilization. According to dielectric data, this

must be the Td.

Thus, summarizing phonons, XRD and dielectric results from our study with local and macroscopic characterization tools, for the nominal composition x(Sn)=0.2 there is a phase which is mostly (rhombohedral) ferroelectric below 200 K, the diffuse transition until Tm=260 K with the change of local distortion to orthorhombic, the region of phase coexistence (relaxor and phase with macroscopic polarization) until T_{CW}=320-340 K, single relaxor phase until Td=480 K, paraelectric above 480 K.

Turning to optical properties of x(Sn)=0.2 (fig. 4.22b), there is a critical point for the band gap at 260 K. Despite the ranges of temperature in the experiment does not permit the measurement of Eg below 235 K, it is visible that the critical point is preceded by a fast decrease of Eg, similarly to what happens at phase transitions of $BaTiO_3$. There seems to be a correlation between the decrease in Eg until 260 K, decrease of Eu until 270 K, and the changes in Raman spectroscopy, such as the decrease in the frequency of the A_1*(TO_3) mode and the disappearance of E*(TO_3) mode.

The Eg steplike decrease at 550 cm^{-1} could correspond to full disappearance of dynamic polar correlations similar to $BaTiO_3$ [49].

The decrease of the Urbach tail characteristic energy, which is indicating the disorder of the transition (fig. 4.22) close to the Tm (fig. 2.6b) is probably associated with the disappearance of certain phonon modes which smear less the band gap edges. At $T > Tm$, the Urbach tail Eu is reactive to T_{CW}=324 K by change of slope, which is probably due to coupling with LO_3 mode, or with the 600 cm^{-1} mode, which by the way shows the change of slope for peak position. The kink and the Eu slope alternation at Td=480 K seems as well to be connected with the beginning of frequency decrease of disorder-related mode at 600 cm^{-1}.

We summarize the temperature sequence of phases in x(Sn)=0.2 in fig. 4.23.

Taking into account that the most significant changes of band gap occurs when the local symmetry is changed (FE phase transitions or Tm in x(Sn)=0.2), we do not present here the data for other compositions. It is nevertheless a prospective for future works to study the connection between Urbach tail and the phonons in relaxor compositions.

4.2.2 X-ray photoelectron spectroscopy

Figure 4.24 shows the XPS peaks for each element. The intensity of Sn 3d peak and Ti 2p is proportional to concentration, according to sensitivity factors, and there are no unidentified shoulders or satellite peaks. It is noteworthy that the Ba 3d peaks contain a contribution from both Ba-TiO_3 sublattice and surface carbonate Ba-CO_3, which we have identified and deconvoluted according to literature expected values for peak widths and relative energy positions. Similarly, the O 1s peak is formed by the contribution from the perovskite sublattice and from the surface organic bonds with H. The B site peaks are

well fitted by the single component, which confirms the correct valence state and absence of significant amounts of defects at the surface.

Table 4.3: XPS quantification results of $BaSn_xTi_{1-x}O_3$ ceramics

x(Sn)	Sn/Ba	Sn/Ba (theor)	Sn/Ti	Sn/Ti (theor)	Ti/Ba	Ti/Ba (theor)
0					0.94	1
0.1	0.17	0.1	0.17	0.11	0.99	0.9
0.2	0.28	0.2	0.39	0.25	0.7	0.8
0.4	0.58	0.4	1.05	0.67	0.55	0.6
0.5	0.65	0.5	1.39	1	0.47	0.5
0.6	0.79	0.6	2.29	1.5	0.35	0.4
0.8	1.07	0.8	5.93	4	0.18	0.2
0.9	1.25	0.9	14.96	9	0.08	0.1
1	1.44	1.00				

The quantification results are shown in table 4.3. While the ratio of Ti/Ba concentrations is very close to the nominal one, there seems to be an excess of Sn, as deduced from the ratio Sn/Ba and Sn/Ti at the surface, more significant in Sn-rich samples.

We note that the effective screening on both Ti and Sn atoms increases until x(Sn)=0.8, and then decreases after x(Sn)=0.8 (fig. 4.25). The trend and energy change are similar to those of the band gap fig. 3.4b. The former probably suggests that both B-site atoms are influenced in the similar way by local environment. Whether the latter is connected with the valence band maximum or conduction band minimum shifts, cannot unfortunately be verified with these experiments.

The difference ΔB.E.(Ba 3d - Ti 2p) and ΔB.E.(Ba 3d - Sn 2p) is larger in Sn-rich compositions, meaning that in those compositions there is more electron screening on B-site atoms. By extrapolation, the charge screening on Ti in $BaTiO_3$ is smaller than on Sn in $BaSnO_3$, which means that Ti is more oxidized than Sn (due to dynamic hybridizations induced by phonons and/or the larger unit cell provided by the Sn-rich matrix).

The values of ΔB.E.(Ba 3d - O 1s) for pure end compounds do not follow the predicted Born charges (the Born charge of O in $BaTiO_3$ is in absolute value larger than in $BaSnO_3$). On one hand, this could be caused by the surface effects due to organic bonds. Other possibility can be that the defects or local structure are usually not taken into account in the calculation of electronic structure of $BaSnO_3$. The Born charge absolute value could be unprecise because the very same calculations predicted no allowed Raman modes in $BaSnO_3$, while there are Raman active phonons that are visible and their positions seem to be in agreement with those caused by a local orthorhombic distortion [59, 58]. The difference ΔB.E. (Ba 3d - O 1s) increases linearly

for all the compositions until x(Sn)=0.8. It stays approximately constant for x(Sn)>0.8.

The possible reason of why ΔB.E.(Ba 3d - O 1s) increases instead of decrease predicted from calculations could be proposed through the shape of the valence band of different compositions in fig. 4.26. From calculations in fig. 4.26b, hybridization with Ba contributes to the larger B.E. side of the complex valence band shape [53, 67]. In our measured VB of $BaTiO_3$, the larger intensity lies as well at larger B.E. values. For x(Sn)=0.5, the maximum of intensity shifts to higher B.E., and in $BaSnO_3$ forms maximum on the low-B.E. side. This contribution is caused by hybridization with Ba levels [125]. The shift of Ba-O hybridized level to higher energy can mean that it benefits of higher electronic charge. Probably, the increase of O atom screening relative to Ba is happening for the same reason.

Special attention should be paid to the increase of electron screening for Ti and Sn levels above values of pure $BaSnO_3$ for x(Sn)=0.5-0.8. If the simple charge transfer in Ti-O bond was happening, the increase of screening for Ti and Sn would probably correspond to opposite trend for O, which depicted from our results. Within the unit cell with same characteristics, the simultaneous increase in effective charge of A- and B-site atoms in perovskites is unfavorable from the principle of Pauli repulsion between Ba-O and Ti-O hybridized orbitals [126]. We speculate that two bonds could be involved, both Ti-O and Ba-O. The A-O bond tends to strengthen when the O-B-O octahedral angle deviates from 180° [67]. Therefore the XPS data are compatible with our conclusions from the Raman spectroscopy that rhombohedral distortions increase for compositions x(Sn)=0.5-0.8, and that the amount of distorted clusters decrease for x(Sn)=0.8-1. Everything goes in line with the band gap non-linear trend.

We also note that for Sn 4d core levels (fig. 4.25) two peaks can be observed, in contrast to the single peak measured for $BaSnO_3$ compound. This result is compatible with the existence of different bonding for Sn in this composition, which can be allowed in rhombohedral or orthorhombic distortions.

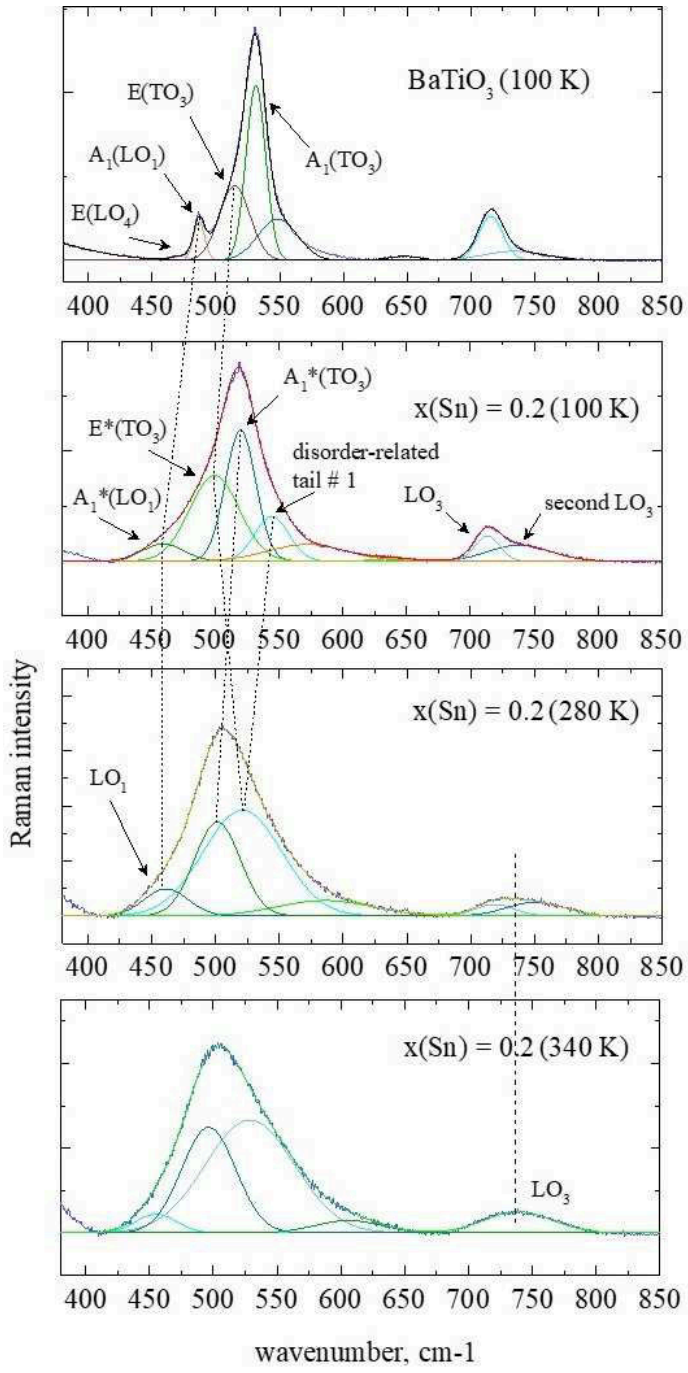

Figure 4.19: The fit of Raman spectra of x(Sn)=0.2 at different temperatures

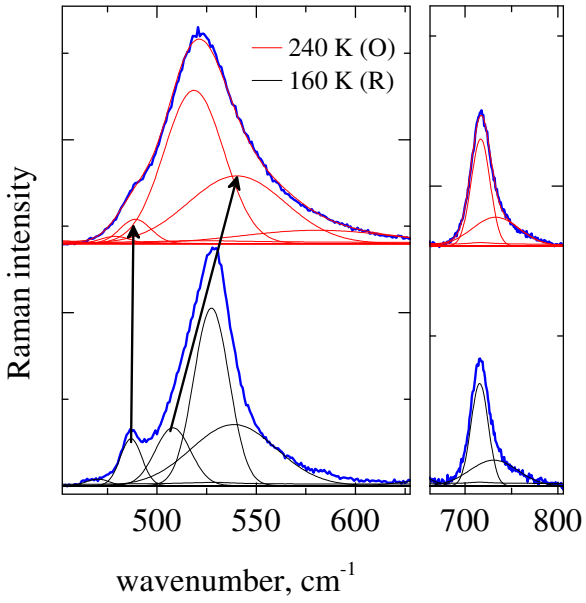

Figure 4.20: The appearance of fitted $BaTiO_3$ spectrum in high-wavenumber region in R and O phases

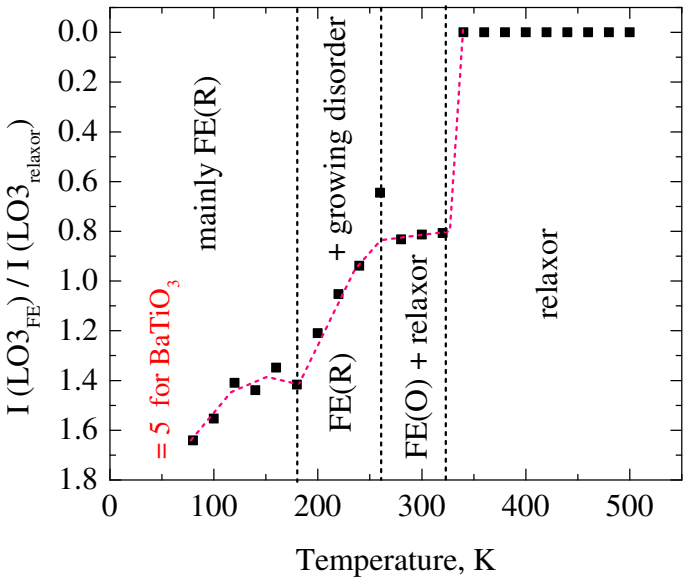

Figure 4.21: The intensity ratio $I(LO_3)_{FE}/I(LO_3)_{relaxor}$ of two LO_3 components in 700 cm^{-1} region of x(Sn)=0.2, low frequency one $(LO_3)_{FE}$, characteristic for ferroelectrics, and high frequency one $(LO_3)_{relaxor}$, which is disorder-coupled and characteristic to relaxors)

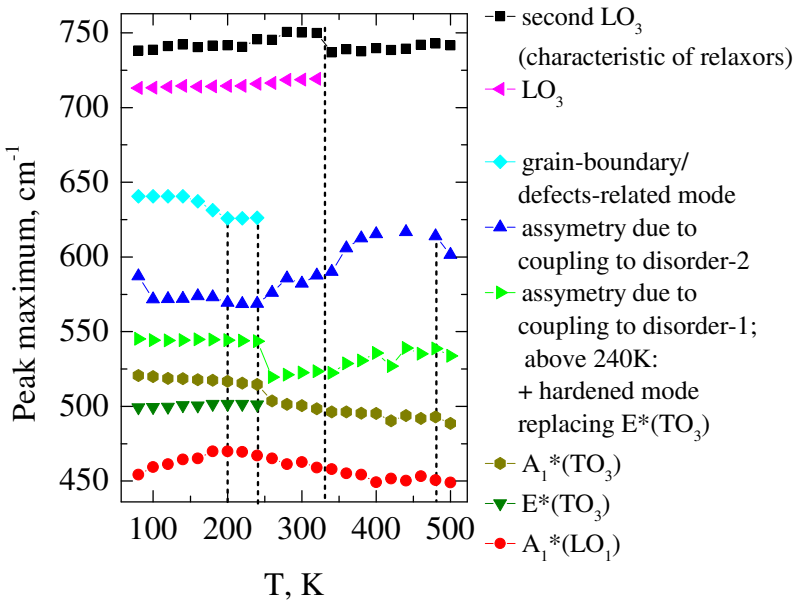

(a)

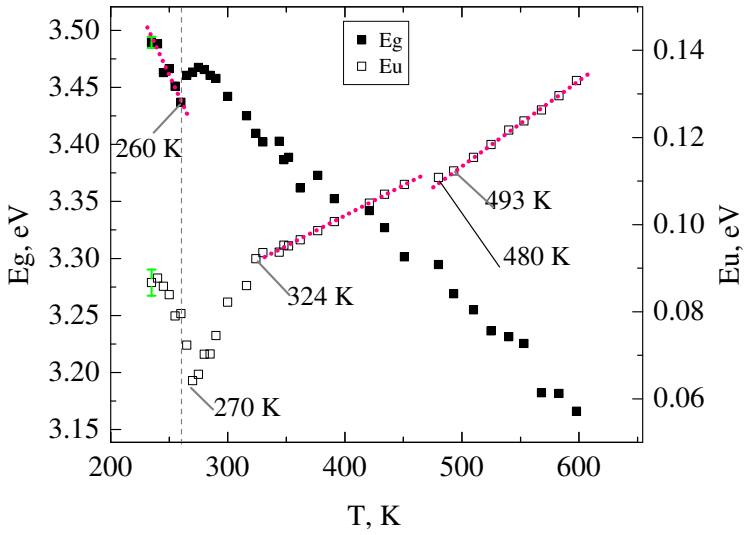

(b)

Figure 4.22: Connection between phonons and the optical absorption in x(Sn)=0.2: (a) the Raman peak maximum evolution; (b) Eg and Eu temperature dependence (reproduced from Chapter 2)

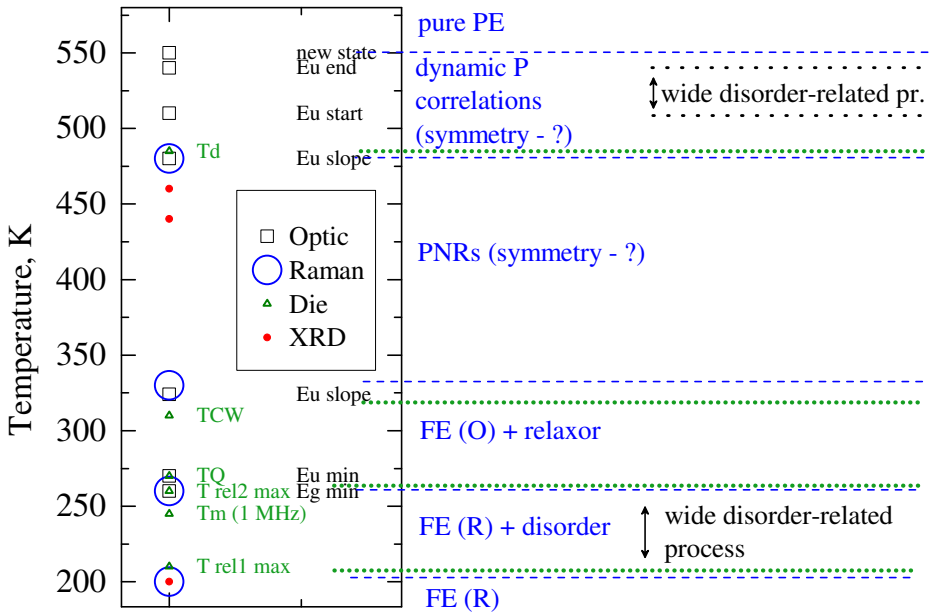

Figure 4.23: The summary on phase and disorder transitions in x(Sn)=0.2, using the data from XRD and dielectric, UV-visible-NIR, and Raman spectroscopies

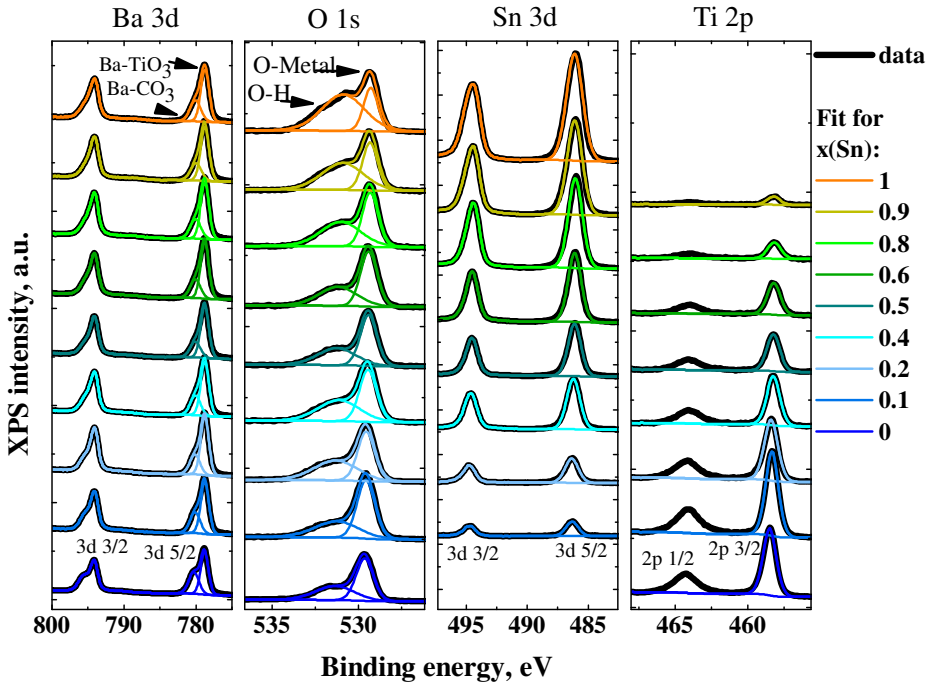

Figure 4.24: XPS spectra at room temperature for $BaSn_xTi_{1-x}O_3$ with different Sn ratio

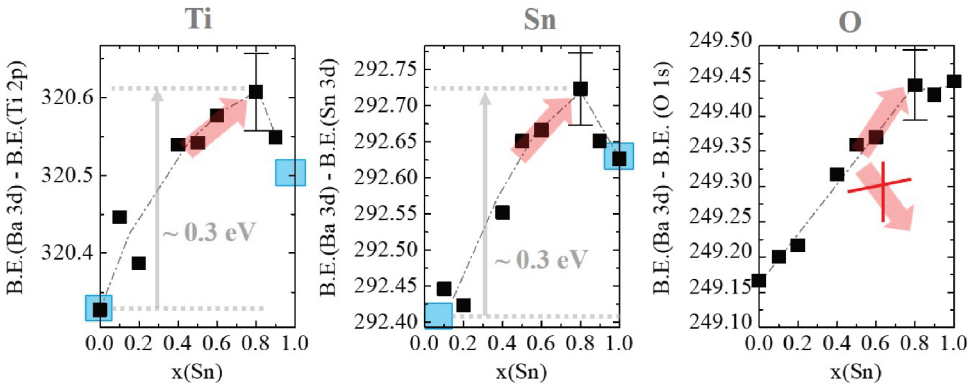

Figure 4.25: The difference between Ba 3d 5/2 and core peaks of other atoms plotted for different compositions

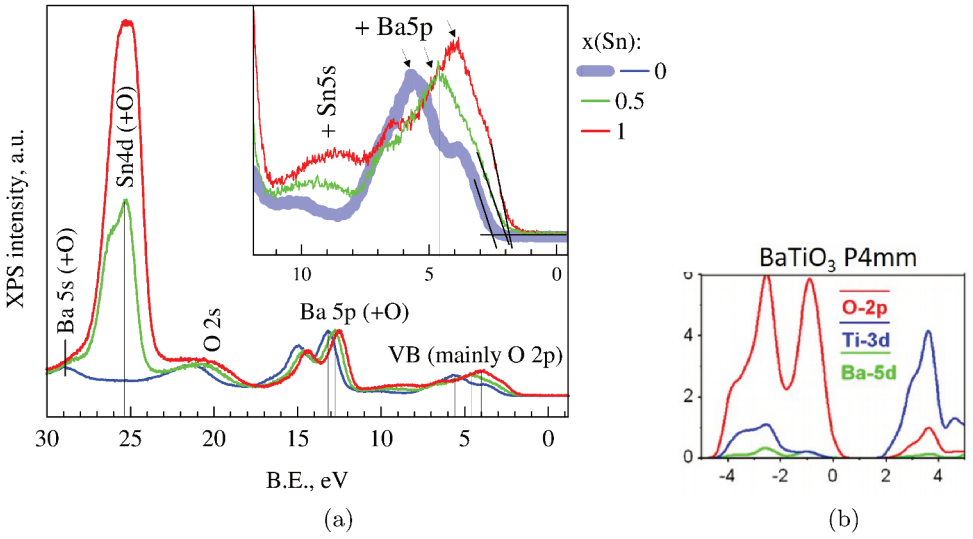

Figure 4.26: (a) The valence band of different compositions on the energy scale calibrated by Ba 3d 5/2 level; (b) the calculated shape of valence and conduction bands of $BaTiO_3$. Y-axis corresponds to the calculated DOS and X-axis to the binding energy (negative for valence band, positive for conduction band). [53]

Conclusions

Raman spectroscopy well describes the polar order and the kind of distortions. With the addition of the information from previous chapters, we can picture out the next section of the phase diagram at room temperature:

- FE-like with tetragonal distortion symmetry for $0<x(Sn)\leq 0.1$
- $x(Sn)=0.2$ as the only representative of a sample with a diffuse phase transition and the resulting phase coexistence at room temperature. Both FE and relaxor-like components are detected in Raman. Note that according to dielectric measurements, at room temperature the major phase is FE-like with very weak distortions (close to T_{CW} where the macroscopic static polarization disappears). The mixture of relaxor-like phase is evidenced only by Raman.

  The symmetry deduced from Raman spectra is mainly orthorhombic, with very weak mixture of rhombohedral distortions.
- $x(Sn)=0.4$ - the pure relaxor composition with mainly orthorhombic distortions and a small mixture of rhombohedral ones
- $0.5<x(Sn)<0.75$ relaxor compositions with both orthorhombic and growing rhombohedral distortions
- $0.75<x(Sn)\leq 0.9$ clusters containing Ti within a purely paraelectric $BaSnO_3$ matrix. The distortions preserve the same characteristics (O + R) as just below the percolation limit, probably because within the clusters the chemical stress stays similar.

In addition to giving a clear understanding of the polar state, Raman spectroscopy allows to qualitatively explain the band gap non-linear step-like changes in temperature at the phase transitions with the massive change of distortion kind (unit cell symmetry). We observe such changes both in $BaTiO_3$ (phonon mode of Axe character A_1TO_3) and $x(Sn)=0.2$ (also Axe mode E^*TO_3). The Axe mode is responsible for dynamic component of bond hybridization in $pd\pi$ (Ti-O) or $ps\pi$ (Sn-O) chemical bond, which form the conduction band minimum.

The change of unit cell symmetry and kind of distortion changes both the static and the dynamic components of the effective charge. The static component should be connected with macroscopic polarization P, however it was pointed out in [74] that the separation between transverse and longitudinal Eg was not straightly proportional to P^2 as it is supposed to

be in the static model, but rather was connected with dynamic polarization fluctuations. Similar quantitative analysis is out of the scope of this work, as it would probably require the Raman spectra to be recorded from single crystals, as well as the comparison to theoretical calculations.

We demonstrate on the example of x(Sn)=0.2 that there is a clear connection between phonons and the temperature evolution of the Urbach tail Eu. The Eu decreases at 270 K, where the phonon mode causing the band gap non-linearity dies off. Additionally, Eu changes the slope at transitions which seem to involve only the change of polar order (T_{CW}, Td).

In agreement with the distortion-Eg connection deduced from Raman spectroscopy, we also evidence the connection between the effective charge of B-site atoms and Eg through X-ray photoelectron spectroscopy. The electron screening of core levels on Ti and Sn atoms is increasing (relative to Ba) for compositions x(Sn)<0.8 and decreasing for 0.8<x(Sn)<1, the excess of electron charge originating probably from the distortions of the unit cell and the octahedral angle O-B-O deviation from 180°.

Chapter 5

Conclusions

The study of optical properties of perovskite solid solutions is of great interest in connection with their macroscopic structure and local polar order which can alternate the chemical bonding. The properties of ferroelectric solid solutions, including photovoltaic, piezoelectric, dielectric, electrocaloric etc. often show non-linear behaviour and potentially allow to reach new functionalities in applied devices. In our work, we have concentrated on solid solutions $BaSn_xTi_{1-x}O_3$ with the end members $BaTiO_3$ (ferroelectric) and $BaSnO_3$ (paraelectric). The similar valence of Ti and Sn (+4) should prevent large concentrations of defects, while Sn could potentially contribute to better electron mobility by its conduction band levels Sn 5s 5p.

In the first chapter, we have studied the compositional and temperature dependence of the crystallographic structure by X-ray diffraction and polar order by dielectric spectroscopy, and we had an insight into the atomic structure and local atomic distortions of the relaxor phase by using transmission electron microscopy. Despite the linear compositional dependence of the unit cell volume at room temperature, a range of different phases is discovered. Adding more Ti atoms introduces chemical stress which causes the decrease of ferroelectric distortion and increasing polar disorder. The sequence of phases is:

- ferroelectric (x(Sn)=0...0.1)
- material in diffuse phase transition state where ferroelectric and relaxor phases coexist, with quasicubic unit cell (x(Sn)=0.1...0.3)
- relaxor phase with average quasicubic unit cell but presence of nanoclusters of distorted phase from x(Sn)=0.3 to 0.8 or higher Sn ratio

The dielectric properties of Ti-rich compositions seem to be defined by polar order of ferroelectric origin, while the dipoles of non-ferroelectric (defect) origin play an important role for Sn-rich compositions.

The local atomic structure shows that the PNRs in the relaxor phase in x(Sn) = 0.4 seem smaller in size, but the distortion of the B-site atoms increases in comparison to compositions which are inside the diffuse phase transition region at room temperature. The distortion state is mixed, but a component along the <111> rhombohedral axis is present.

After characterization of the samples, in second chapter we tested the optical absorption of solid solutions at room temperature for compositional series, and with varying the temperature for chosen compositions for deeper insight into dependence of optical properties on the changing polar order.

In the compositional series, the band gap shows non-linear behaviour. It increases by ∼0.35 eV until x(Sn)=0.8 and decreases for Sn-rich compositions. From our data, the band gap seems to be defined by wide smeared feature where the Sn and Ti levels cannot be separated, we assume that the band gap is defined by mixed levels. We find a connection between the band gap and the type of disorder in the compositional series. Based on this, we also studied the temperature dependence of the band gap in connection with changing disorder regimes. In general, the band gap varies homogeneously within one phase, followed by a non-linear decrease on temperature increase around phase transitions, and followed by another linear regime. For $BaTiO_3$ above Tc, the slope of Eg variation differs for the phase with static polar correlations and the phase where they are absent. For Ti-rich solid solutions, the Eg and Eu react to changes of the polar state, while for $BaSnO_3$ and probably Sn-rich compositions the disorder is determined by defects which are related to oxidation/reduction of the material.

Based on the importance of local disorder for optical properties, in the last chapter of this manuscript we analysed the local structure and disorder in connection to chemical bonding. Concentrating on phase transitions, we use Raman spectroscopy to distinguish the different types of local structural distortions and their magnitude, for compositional series and in temperature. This study combined with crystallographic, dielectric, and optical data, results in our redefinition of the sequence of phases at room temperature:

- FE-like for 0<x(Sn)≤0.1

- x(Sn)=0.2 as the only representative of the sample with diffuse phase transition and the resulting phase coexistence at room temperature. Both FE and relaxor-like components are detected in Raman. Note that according to dielectric measurements, at room temperature the major phase is FE-like with very weak distortions (close to T_{CW} where the macroscopic static polarization disappears). The mixture of relaxor-like phase is evidenced only by Raman.

  The symmetry deduced from Raman spectra is mainly orthorhombic, with very weak mixture of rhombohedral distortions.

- x(Sn)=0.4 - the pure relaxor composition with mainly orthorhombic distortions and the small mixture of rhombohedral ones
- 0.5<x(Sn)<0.75 relaxor compositions with both orthorhombic and growing rhombohedral distortions
- 0.75<x(Sn)≤0.9 clusters containing Ti within pure cubic $BaSnO_3$ matrix. The distortions preserve same characteristics (O + R) as just below the percolation limit, probably because within the clusters the chemical stress stays similar.

The band gap of a single composition decreases stepwise on increase of temperature if the change of the type of local symmetry occurs (e.g. rhombohedral-orthorhombic). According to our discussion, the band gap value is in significant degree dependent on the different components of phonon $A_1^*TO_3$ of Axe type, evidenced in Raman. The phonons of this type modify the overlap of orbitals of O and B-site atoms in ABO_3 which form the π bond that defines the energy of the conduction band minimum.

The degree of overlap of the atomic orbitals also modifies the distribution of the effective electronic charge of the atoms. This effective charge can be qualitatively analysed through X-ray photoelectron spectroscopy. Since there are distortions of the unit cell, the octahedral angle O-B-O deviates from 180°, simultaneously, an increase of the effective electronic charge on the B site and on O becomes possible, which is energetically unfavorable in a non-distorted unit cell. This trend appears in our XPS results between x(Sn)=0 and 0.8, with excess of effective charge decreasing for x(Sn)=0.8...1. This proves that the band gap increase in the compositional series is caused by the increasing rhombohedral distortions, and the following decrease of the bad gap agrees well with the gradual disappearance of distorted phase clusters in Sn-rich compositions.

Outlook and perspectives

Since Sn should contribute to an increase of the electron mobility, it would be of interest to perform the measurement to evaluate the changes in comparison to $BaTiO_3$. However, because of the microscopic size of grains, it can be experimentally complicated. To the contrary, it is possible to estimate the photovoltaic response from short-circuit current measured under laser illumination. These measurements were performed at the Institut de Ciència de Materials de Barcelona, but need additional processing before being shown to a thesis committee. The measurements were performed under lasers of different energies within the band gap of $BaTiO_3$ on different compositions. The short circuit current response consists of several components, including transient behaviour which might depend on defect concentrations.

The more profound analysis of this data can be performed if compared to the analysis of photoluminescence experiments which were performed at the Institut de Nanoscience de Lyon. In those experiments the electrons are excited to the energy level in the conduction band, and then recombine with the defect levels inside the band gap. The concentration of defects, including the distortion-related polarons, and the energies of levels can be analysed for better explanation of transient components as well as shift photocurrent values which depend on defect trapping.

Bibliography

[1] William Shockley and Hans J Queisser. Detailed balance limit of efficiency of p-n junction solar cells. *Journal of applied physics*, 32(3):510–519, 1961.

[2] Eden Rephaeli and Shanhui Fan. Absorber and emitter for solar thermophotovoltaic systems to achieve efficiency exceeding the Shockley-Queisser limit. *Optics express*, 17(17):15145–15159, 2009.

[3] Peter Krogstrup, Henrik Ingerslev Jørgensen, Martin Heiss, Olivier Demichel, Jeppe V Holm, Martin Aagesen, Jesper Nygard, and Anna Fontcuberta i Morral. Single-nanowire solar cells beyond the Shockley-Queisser limit. *Nature Photonics*, 7(4):306–310, 2013.

[4] Robert T. Ross and Arthur J. Nozik. Efficiency of hot-carrier solar energy converters. *Journal of Applied Physics*, 53(5):3813–3818, May 1982.

[5] R. D. Schaller and V. I. Klimov. High Efficiency Carrier Multiplication in *PbSe* Nanocrystals: Implications for Solar Energy Conversion. *Physical Review Letters*, 92(18), May 2004.

[6] A. J. Nozik, M. C. Beard, J. M. Luther, M. Law, R. J. Ellingson, and J. C. Johnson. Semiconductor quantum dots and quantum dot arrays and applications of multiple exciton generation to third-generation photovoltaic solar cells. *Chemical Reviews*, 110(11):6873–6890, November 2010.

[7] O. E. Semonin, J. M. Luther, S. Choi, H.-Y. Chen, J. Gao, A. J. Nozik, and M. C. Beard. Peak External Photocurrent Quantum Efficiency Exceeding 100 % via MEG in a Quantum Dot Solar Cell. *Science*, 334(6062):1530–1533, December 2011.

[8] Jonathan E. Spanier, Vladimir M. Fridkin, Andrew M. Rappe, Andrew R. Akbashev, Alessia Polemi, Yubo Qi, Zongquan Gu, Steve M. Young, Christopher J. Hawley, Dominic Imbrenda, Geoffrey Xiao, Andrew L. Bennett-Jackson, and Craig L. Johnson. Power conversion efficiency exceeding the Shockley–Queisser limit in a ferroelectric insulator. *Nature Photonics*, 10(9):611–616, August 2016.

[9] Charles Paillard, Xiaofei Bai, Ingrid C Infante, Maël Guennou, Grégory Geneste, Marin Alexe, Jens Kreisel, and Brahim Dkhil. Photovoltaics with ferroelectrics: Current status and beyond. *Advanced Materials*, 28(26):5153–5168, 2016.

[10] A. M. Glass, D. Von Der Linde, and T. J. Negran. High-voltage bulk photovoltaic effect and the photorefractive process in $LiNbO_3$. *Applied Physics Letters*, 25(4):233–235, 1974.

[11] W.T.H. Koch, R. Munser, W. Ruppel, and P. Würfel. Bulk photovoltaic effect in $BaTiO_3$. *Solid State Communications*, 17(7):847 – 850, 1975.

[12] J. G. Bendoraitis and R. E. Salomon. Optical energy gaps in the monoclinic oxides of hafnium and zirconium and their solid solutions. *The Journal of Physical Chemistry*, 69(10):3666–3667, October 1965.

[13] Pakpoom Reunchan, Naoto Umezawa, Shuxin Ouyang, and Jinhua Ye. Mechanism of photocatalytic activities in Cr-doped $SrTiO_3$ under visible-light irradiation: an insight from hybrid density-functional calculations. *Physical Chemistry Chemical Physics*, 14(3):1876, 2012.

[14] Wenliang Zhou, Hongmei Deng, Tuo Zheng, Pingxiong Yang, and Junhao Chu. Pb-free semiconductor ferroelectrics: An experimental study of $Ba(Ti_{0.75}Ce_{0.125}Pd_{0.125})O_3$ thin films. *Materials Letters*, 177:1–4, August 2016.

[15] Joseph W. Bennett, Ilya Grinberg, Peter K. Davies, and Andrew M. Rappe. Pb-free semiconductor ferroelectrics: A theoretical study of Pd-substituted $BaTiO_3$. *Physical Review B*, 82(18):184106, 2010.

[16] Tingting Qi, Ilya Grinberg, and Andrew M. Rappe. First-principles investigation of the highly tetragonal ferroelectric material $Bi(Zn_{1/2}Ti_{1/2})O_3$. *Physical Review B - Condensed Matter and Materials Physics*, 79(9):1–5, 2009.

[17] Tingting Qi, Ilya Grinberg, and Andrew M. Rappe. Band-gap engineering via local environment in complex oxides. *Physical Review B - Condensed Matter and Materials Physics*, 83(22):1–6, 2011.

[18] Hungru Chen and Naoto Umezawa. Effect of cation arrangement on the electronic structures of the perovskite solid solutions $SrTiO_3(1-x) - LaCrO_3(x)$ from first principles. *Physical Review B*, 90(4), July 2014.

[19] Lu Yu, Hongmei Deng, Wenliang Zhou, Pingxiong Yang, and Junhao Chu. Structural characteristics and optical properties of lead-free $Bi(Zn_{1/2}Ti_{1/2})O_3 - BaTiO_3$ ceramics. *Ceramics International*, 43(8):6175–6179, June 2017.

[20] Woo Seok Choi, Matthew F. Chisholm, David J. Singh, Taekjib Choi, Gerald E. Jellison, and Ho Nyung Lee. Wide bandgap tunability in complex transition metal oxides by site-specific substitution. *Nature Communications*, 3:689, 2012.

[21] R. Nechache, C. Harnagea, S. Li, L. Cardenas, W. Huang, J. Chakrabartty, and F. Rosei. Bandgap tuning of multiferroic oxide solar cells. *Nature Photonics*, 9(1):61–67, 2014.

[22] Huafeng Dong, Zhigang Wu, Shanying Wang, Wenhui Duan, and Jingbo Li. Improving the optical absorption of $BiFeO_3$ for photovoltaic applications via uniaxial compression or biaxial tension. *Applied Physics Letters*, 102(7):072905, 2013.

[23] Ch. Eisenschmidt, H. T. Langhammer, R. Steinhausen, and G. Schmidt. Tetragonal-Orthorhombic Phase Transition in Barium Titanate via Monoclinic MC-Type Symmetry. *Ferroelectrics*, 432(1):103–116, January 2012.

[24] David Vanderbilt and Morrel H. Cohen. Monoclinic and triclinic phases in higher-order devonshire theory. *Physical Review B*, 63(9), January 2001.

[25] Elena Aksel and Jacob L. Jones. Advances in lead-free piezoelectric materials for sensors and actuators. *Sensors*, 10(3):1935–1954, March 2010.

[26] K. Itoh, L. Z. Zeng, E. Nakamura, and N. Mishima. Crystal structure of $BaTiO_3$ in the cubic phase. *Ferroelectrics*, 63(1):29–37, 1985-06.

[27] B. Noheda, D. E. Cox, G. Shirane, R. Guo, B. Jones, and L. E. Cross. Stability of the monoclinic phase in the ferroelectric perovskite $PbZr_{1-x}Ti_xO_3$. *Physical Review B*, 63(1), December 2000.

[28] Ajay Kumar Kalyani, Hari Krishnan, Arijit Sen, Anatoliy Senyshyn, and Rajeev Ranjan. Polarization switching and high piezoelectric response in Sn-modified $BaTiO_3$. *Physical Review B*, 91(2), January 2015.

[29] Émile Bévillon, Anthony Chesnaud, Yanzhong Wang, Guilhem Dezanneau, and Grégory Geneste. Theoretical and experimental study of the structural, dynamical and dielectric properties of perovskite $BaSnO_3$. *Journal of Physics: Condensed Matter*, 20(14):145217, 2008.

[30] R. D. Shannon. Revised effective ionic radii and systematic studies of interatomic distances in halides and chalcogenides. *Acta Crystallographica Section A*, 32(5):751–767, sep 1976.

[31] Xiaoyong Wei and Xi Yao. Preparation, structure and dielectric property of barium stannate titanate ceramics. *Materials Science and Engineering: B*, 137(1-3):184–188, 2007.

[32] R. Von Der Mühll, A. Simon, C. Elissalde, and A. Villesuzanne. Dielectric investigation of a new TKWB lead free relaxor. *Journal of Physics and Chemistry of Solids*, 65(6):1039–1043, 2004.

[33] Yonggang Yao, Chao Zhou, Duchao Lv, Dong Wang, Haijun Wu, Yaodong Yang, and Xiaobing Ren. Large piezoelectricity and dielectric permittivity in $BaTiO_3 - xBaSnO_3$ system: The role of phase coexisting. *EPL (Europhysics Letters)*, 98(2):27008, 2012.

[34] Ljiljana Veselinovic, Miodrag Mitric, Lidija Mancic, Marija Vukomanovic, Branka Hadzic, Smilja Markovic, and Dragan Uskokovic. The effect of Sn for Ti substitution on the average and local crystal structure of $BaTi_{1-x}Sn_xO_3$ (x=0...0.20) . *Journal of Applied Crystallography*, 47(3):999–1007, 2014.

[35] Tao Shi, Lin Xie, Lin Gu, and Jing Zhu. Why Sn doping significantly enhances the dielectric properties of $Ba(Ti_{1-x}Sn_x)O_3$. *Scientific Reports*, 5:8606, 2015.

[36] L. Xie, Y. L. Li, R. Yu, Z. Y. Cheng, X. Y. Wei, X. Yao, C. L. Jia, K. Urban, A. A. Bokov, Z. G. Ye, and J. Zhu. Static and dynamic polar nanoregions in relaxor ferroelectric $Ba(Ti_{1-x}Sn_x)O_3$ system at high temperature. *Physical Review B - Condensed Matter and Materials Physics*, 85(1):1–5, 2012.

[37] Tao Shi, Lin Gu, and Jing Zhu. Explanation of diffuse scattering mechanism based on the structure of polar nanoregions in $BaTi_{1-x}Sn_xO_3$. *Journal of Applied Physics*, 120(12):124103, 2016-09.

[38] Yun Liu, Ray L. Withers, Xiaoyong Wei, and John D. Fitz Gerald. Structured diffuse scattering and polar nano-regions in the $BaTi_{1-x}Sn_xO_3$ relaxor ferroelectric system. *Journal of Solid State Chemistry*, 180(3):858–865, 2007.

[39] X Zhang, L Wu, S Gao, JQ Liu, B Xu, YD Xia, J Yin, and ZG Liu. Large electrocaloric effect in $Ba(Ti_{1-x}Sn_x)O_3$ ceramics over a broad temperature region. *AIP Advances*, 5(4):047134, 2015.

[40] Zhengdong Luo, Dawei Zhang, Yang Liu, Di Zhou, Yonggang Yao, Chenqi Liu, Brahim Dkhil, Xiaobing Ren, and Xiaojie Lou. Enhanced electrocaloric effect in lead-free $BaTi_{1-x}Sn_xO_3$ ceramics near room temperature. *Applied Physics Letters*, 105(10):102904, September 2014.

[41] Mehmet Sanlialp, Zhengdong Luo, Vladimir V. Shvartsman, Xianzhu Wei, Yang Liu, Brahim Dkhil, and Doru C. Lupascu. Direct measurement of electrocaloric effect in lead-free $BaSn_xTi_{1-x}O_3$ ceramics. *Applied Physics Letters*, 111(17):173903, October 2017.

[42] Ulrich Straube, Bernd Broich, Ludwig Geske, Ralf Steinhausen, Hans Theo Langhammer, Horst Beige, and Hans-Peter Abicht. Ultrasound Investigations of $BaTi_{1-x}Sn_xO_3$ Ceramics. *Ferroelectrics*, 353(1):164–170, May 2007.

[43] C Lei, AA Bokov, and Z-G Ye. Ferroelectric to relaxor crossover and dielectric phase diagram in the $BaTiO_3 - BaSnO_3$ system. *Journal of applied physics*, 101(8):084105, 2007.

[44] V.V. Shvartsman, J. Dec, Z.K. Xu, J. Banys, P. Keburis, and W. Kleemann. Crossover from ferroelectric to relaxor behavior in $BaTi_{1-x}Sn_xO_3$ solid solutions. *Phase Transitions*, 81(11-12):1013–1021, November 2008.

[45] Ibtessam A. Alagdal and Anthony R. West. Oxygen stoichiometry, conductivity and gas sensing properties of $BaSnO_3$. *Journal of Materials Chemistry C*, 4(21):4770–4777, 2016.

[46] M Muralidharan, V Anbarasu, A Elaya Perumal, and K Sivakumar. Room temperature ferromagnetism in Cr doped $SrSnO_3$ perovskite system. *Journal of Materials Science: Materials in Electronics*, 5(28):4125–4137, 2016.

[47] Tanmoy Maiti, R Guo, and AS Bhalla. Structure-Property Phase Diagram of $BaZr_xTi_{1-x}O_3$ System. *Journal of the American Ceramic Society*, 91(6):1769–1780, 2008.

[48] Ekhard KH Salje, Michael A Carpenter, Guillaume F Nataf, Gunnar Picht, Kyle Webber, Jeevaka Weerasinghe, S Lisenkov, and L Bellaiche. Elastic excitations in $BaTiO_3$ single crystals and ceramics: Mobile domain boundaries and polar nanoregions observed by resonant ultrasonic spectroscopy. *Physical Review B*, 87(1):014106, 2013.

[49] E Dul'kin, J Petzelt, S Kamba, E Mojaev, and M Roth. Relaxor-like behavior of $BaTiO_3$ crystals from acoustic emission study. *Applied Physics Letters*, 97(3):032903, 2010.

[50] A. Bouhemadou and K. Haddadi. Structural, elastic, electronic and thermal properties of the cubic perovskite-type $BaSnO_3$. *Solid State Sciences*, 12(4):630–636, 2010.

[51] San Dong Guo and Bang Gui Liu. Electronic structures and optical dielectric functions of room temperature phases of $SrTiO_3$ and $BaTiO_3$. *Journal of Applied Physics*, 110(7):0–5, 2011.

[52] S. Sanna, C. Thierfelder, S. Wippermann, T. P. Sinha, and W. G. Schmidt. Barium titanate ground- and excited-state properties from first-principles calculations. *Physical Review B - Condensed Matter and Materials Physics*, 83(5):1–9, 2011.

[53] Qi Jun Liu, Ning Chao Zhang, Fu Sheng Liu, Hong Yan Wang, and Zheng Tang Liu. $BaTiO_3$: Energy, geometrical and electronic structure, relationship between optical constant and density from first-principles calculations. *Optical Materials*, 35(12):2629–2637, 2013.

[54] SI Shablaev, AM Danishevskij, and VK Subashiev. Band structure of oxygen-octahedral ferroelectric $BaTiO_3$, $SrTiO_3$ and $KTaO_3$ derived from two-photon spectroscopy data. *Zhurnal Ehksperimental'noj i Teoreticheskoj Fiziki*, 86(6):2158–2169, 1984.

[55] R Khenata, M Sahnoun, H Baltache, M Rerat, AH Rashek, N Illes, and B Bouhafs. First-principle calculations of structural, electronic and optical properties of $BaTiO_3$ and $BaZrO_3$ under hydrostatic pressure. *Solid state communications*, 136(2):120–125, 2005.

[56] David O. Scanlon. Defect engineering of $BaSnO_3$ for high-performance transparent conducting oxide applications. *Physical Review B - Condensed Matter and Materials Physics*, 87(16):1–5, 2013.

[57] Beom Soo Joo, Young Jun Chang, Luca Moreschini, Aaron Bostwick, Eli Rotenberg, and Moonsup Han. Evidence for indirect band gap in $BaSnO_3$ using angle-resolved photoemission spectroscopy. *Current Applied Physics*, 17(5):595–599, 2017.

[58] Émile Bevillon and Grégory Geneste. Unstable polar mode and minimum of the dielectric constant in cubic $BaSnO_3$ under hydrostatic pressure. *Physical Review B*, 75(21):214106, 2007.

[59] T. N. Stanislavchuk, A. A. Sirenko, A. P. Litvinchuk, X. Luo, and S.-W. Cheong. Electronic band structure and optical phonons of $BaSnO_3$ and $Ba_{0.97}La_{0.03}SnO_3$ single crystals: Theory and experiment. *Journal of Applied Physics*, 112(4):044108, 2012.

[60] Paul Kubelka and Franz Munk. An article on optics of paint layers. *Z. Tech. Phys*, 12(593-601), 1931.

[61] J. Tauc, R. Grigorovici, and A. Vancu. Optical properties and electronic structure of amorphous germanium. *physica status solidi (b)*, 15(2):627–637, 1966.

[62] Hong Li, Ivano E. Castelli, Kristian S. Thygesen, and Karsten W. Jacobsen. Strain sensitivity of band gaps of Sn-containing semiconductors.

Physical Review B - Condensed Matter and Materials Physics, 91(4):1–6, 2015.

[63] I-K Jeong, CY Park, JS Ahn, S Park, and DJ Kim. Ferroelectric-relaxor crossover in $BaTi_{1-x}Zr_xO_3$ studied using neutron total scattering measurements and reverse Monte Carlo modeling. *Physical Review B*, 81(21):214119, 2010.

[64] Claire Laulhé, Alain Pasturel, Francoise Hippert, and Jens Kreisel. Random local strain effects in homovalent-substituted relaxor ferroelectrics: a first-principles study of $BaTi_{0.74}Zr_{0.26}O_3$. *Physical Review B*, 82(13):132102, 2010.

[65] Igor Levin, Eric Cockayne, Victor Krayzman, Joseph C Woicik, Soonil Lee, and Clive A Randall. Local structure of $Ba(Ti, Zr)O_3$ perovskite-like solid solutions and its relation to the band-gap behavior. *Physical Review B*, 83(9):094122, 2011.

[66] Fenggong Wang, Ilya Grinberg, and Andrew M. Rappe. Band gap engineering strategy via polarization rotation in perovskite ferroelectrics. *Applied Physics Letters*, 104(15):15–19, 2014.

[67] Hiroshi Mizoguchi, Hank W. Eng, and Patrick M. Woodward. Probing the Electronic Structures of Ternary Perovskite and Pyrochlore Oxides Containing Sn^{4+} or Sb^{5+}. *Inorganic Chemistry*, 43(5):1667–1680, 2004.

[68] Yu-Seong Seo and Jai Seok Ahn. First-principles investigations on polytypes of $BaTiO_3$: Hybrid calculations and pressure dependences. *Journal of the Korean Physical Society*, 62(11):1629–1635, 2013.

[69] Keigo Suzuki and Kazunori Kijima. Optical band gap of barium titanate nanoparticles prepared by rf-plasma chemical vapor deposition. *Japanese journal of applied physics*, 44(4R):2081, 2005.

[70] Cailei Yuan, Shuangli Ye, Bo Xu, and Wen Lei. Strain induced tetragonal $SrTiO_3$ nanoparticles at room temperature. *Applied Physics Letters*, 101(7):071909, 2012.

[71] Franz Urbach. The long-wavelength edge of photographic sensitivity and of the electronic absorption of solids. *Physical Review*, 92(5):1324–1324, December 1953.

[72] V Sa-Yakanit and HR Glyde. Urbach tails and disorder. *Comments Matter Phys*, 13(1):35–48, 1987.

[73] M. Kranjčec, I.P. Studenyak, and M.V. Kurik. Urbach rule and disordering processes in $Cu_6P(S_{1-x}Se_x)_5Br_{1-y}I_y$ superionic conductors. *Journal of Physics and Chemistry of Solids*, 67(4):807–817, April 2006.

[74] S. H. Wemple. Polarization Fluctuations and the Optical-Absorption Edge in $BaTiO_3$. *Physical Review B*, 2(7):2679–2689, October 1970.

[75] Thierry Pauporté and Daniel Lincot. Electrodeposition of semiconductors for optoelectronic devices: results on zinc oxide. *Electrochimica Acta*, 45(20):3345–3353, June 2000.

[76] John D. Dow. Urbach's rule. *Plenum Press, New York 1975*, 1975.

[77] Yun Zhang, Yue Shen, Feng Gu, Mingming Wu, Yian Xie, and Jiancheng Zhang. Influence of Fe ions in characteristics and optical properties of mesoporous titanium oxide thin films. *Applied Surface Science*, 256(1):85–89, October 2009.

[78] A. V. Chadwick. High temperature transport in fluorites. *Radiation Effects*, 74(1-4):17–28, January 1983.

[79] I. P. Studenyak, M. Kranjcec, and B. M. Koperlyos. On the Urbach rule in $SbSI$ ferroelectric crystal. *Ukrainian Journal of Physical Optics*, 10(2):61–70, 2009.

[80] Charles Paillard. Photo-induced effects in multiferroics, 2016.

[81] Thierry Pauporté and Daniel Lincot. Electrodeposition of semiconductors for optoelectronic devices: results on zinc oxide. *Electrochimica Acta*, 45(20):3345–3353, June 2000.

[82] G. D. Cody, T. Tiedje, B. Abeles, B. Brooks, and Y. Goldstein. Disorder and the optical-absorption edge of hydrogenated amorphous silicon. *Physical Review Letters*, 47(20):1480–1483, November 1981.

[83] Xiaofei Bai. Size and doping effect on the structure, transitions and optical properties of multiferroic $BiFeO_3$ particles for photocatalytic applications, 2016.

[84] Vikash Mishra, Archna Sagdeo, Vipin Kumar, M. Kamal Warshi, Hari Mohan Rai, S. K. Saxena, Debesh R. Roy, Vinayak Mishra, Rajesh Kumar, and P. R. Sagdeo. Electronic and optical properties of $BaTiO_3$ across tetragonal to cubic phase transition: An experimental and theoretical investigation. *Journal of Applied Physics*, 122(6):065105, August 2017.

[85] Yangzhong Wang. Synthesis and characterisation of acceptor-doped $BaSnO_3$ compounds as proton conductors, 2009.

[86] L Hafid, G. Godefroy, A. El Idrissi, and F.M. Michel-Calendini. Absorption spectrum in the near U.V. and electronic structure of pure barium titanate. *Solid State Communications*, 66(8):841–845, 1988.

[87] V Železný, D Chvostová, and D Šimek. The variation of $PbTiO_3$ bandgap at ferroelectric phase transition. *Journal of Physics: Condensed Matter*, 025501, 2015.

[88] L Xie and J Zhu. The Electronic Structures, Born Effective Charges, and Interatomic Force Constants in $BaMO_3$ (M= Ti, Zr, Hf, Sn): A Comparative First-Principles Study, journal = Journal of the American Ceramic Society. 95(11):3597–3604, 2012.

[89] David J Singh. Electric field gradients in $BaTiO_3$ and $KNbO_3$. *Ferroelectrics*, 153(1):183–187, 1994.

[90] Henry Krakauer, Rici Yu, Cheng-Zhang Wang, Karin M Rabe, and Umesh V Waghmare. Dynamic local distortions in $KNbO_3$. *Journal of Physics: Condensed Matter*, 11(18):3779, 1999.

[91] D. Nuzhnyy, J. Petzelt, M. Savinov, T. Ostapchuk, V. Bovtun, M. Kempa, J. Hlinka, V. Buscaglia, M. T. Buscaglia, and P. Nanni. Broadband dielectric response of $Ba(Zr,Ti)O_3$ ceramics: From incipient via relaxor and diffuse up to classical ferroelectric behavior. *Physical Review B - Condensed Matter and Materials Physics*, 86(1):1–9, 2012.

[92] J Hlinka, T Ostapchuk, D Nuzhnyy, J Petzelt, P Kuzel, Ch Kadlec, P Vanek, I Ponomareva, and L Bellaiche. Coexistence of the phonon and relaxation soft modes in the terahertz dielectric response of tetragonal $BaTiO_3$. *Physical review letters*, 101(16):167402, 2008.

[93] I. Ponomareva, L. Bellaiche, T. Ostapchuk, J. Hlinka, and J. Petzelt. Terahertz dielectric response of cubic $BaTiO_3$. *Physical Review B - Condensed Matter and Materials Physics*, 77(1):1–4, 2008.

[94] Y. Luspin, J .L. Servoin, and F. Gervais. Soft mode spectroscopy in barium titanate. *Journal of Physics C: Solid State Physics*, 13:3761–3773, 1980.

[95] Hoshina Takuya, Kanehara Kazuki, Takeda Hiroaki, and Tsurumi Takaaki. Terahertz dielectric response of single-domain $BaTiO_3$ measured by far-infrared spectroscopic ellipsometry. *Japanese Journal of Applied Physics*, 53(9S):09PD03, 2014.

[96] G Shirane, JD Axe, J Harada, and A Linz. Inelastic Neutron Scattering from Single-Domain $BaTiO_3$. *Physical Review B*, 2(9):3651, 1970.

[97] V. V. Shvartsman, W. Kleemann, J. Dec, Z. K. Xu, and S. G. Lu. Diffuse phase transition in $BaTi_{1-x}Sn_xO_3$ ceramics: An intermediate state between ferroelectric and relaxor behavior. *Journal of Applied Physics*, 99(12):0–8, 2006.

[98] Koustav Ganguly, Abhinav Prakash, Bharat Jalan, and C. Leighton. Mobility-electron density relation probed via controlled oxygen vacancy doping in epitaxial $BaSnO_3$. *APL Materials*, 5(5):056102, May 2017.

[99] Shail Upadhyay, Ashok Kumar Sahu, Devendra Kumar, and Om Parkash. Probing electrical conduction behavior of $BaSnO_3$. *Journal of Applied Physics*, 84(2):828–832, July 1998.

[100] Ashok Kumar, BP Singh, RNP Choudhary, and Awalendra K Thakur. Ferroelectric phase transition in Te-modified $BaSnO_3$. *Materials Letters*, 59(14):1880–1888, 2005.

[101] S. Hodjati, C. Petit, V. Pitchon, and A. Kiennemann. Absorption/desorption of NO_x process on perovskites. *Applied Catalysis B: Environmental*, 27(2):117–126, July 2000.

[102] M D Fontana, K Laabidi, and B Jannot. Quasimodes and a central peak in $BaTiO_3$. *Journal of Physics: Condensed Matter*, 6(42):8923–8930, oct 1994.

[103] J. D. Freire and R S Katiyar. Lattice dynamics of crystals with tetragonal $BaTiO_3$ structure. *Physical Review B*, 37(4), 1988.

[104] C. CH Perry and DB Hall. Temperature Dependence of the Raman Spectrum of $BaTiO_3$. *Physical Review Letters*, 15(17):700–702, 1965.

[105] J. L. Gervais, F. Servoin, A. M. Quittet, and Y. Luspin. Infrared and Raman responses in ferroelectric perovskite crystals: Apparent inconsistencies. *Physical Review B*, 21(5):2038–2041, 1980.

[106] K. Laabidi, M.D. Fontana, and B. Jannot. Underdamped soft phonon in orthorhombic $BaTiO_3$. *Solid state communications*, 76(6):765–768, 1990.

[107] V. Buscaglia, M. T. Buscaglia, M. Viviani, L. Mitoseriu, P. Nanni, V. Trefiletti, P. Piaggio, I. Gregora, T. Ostapchuk, J. Pokorný, and J. Petzelt. Grain size and grain boundary-related effects on the properties of nanocrystalline barium titanate ceramics. *Journal of the European Ceramic Society*, 26(14):2889–2898, 2006.

[108] Scalabrin A, Craves A S, Shima D S, and Porto S P S. Temperature Dependence of the A, and E Optical Phonons in $BaTiO_3$. *Physica Status Solidi (b)*, 79:731–742, 1977.

[109] Lawrence H. Robins, Debra L. Kaiser, Lawrence D. Rotter, Peter K. Schenck, Gregory T. Stauf, and Daniel Rytz. Investigation of the structure of barium titanate thin films by Raman spectroscopy. *Journal of Applied Physics*, 76(11):7487–7498, 1994.

[110] A Chaves, RS Katiyar, and SPS Porto. Coupled modes with A 1 symmetry in tetragonal $BaTiO_3$. *Physical Review B*, 10(8):3522, 1974.

[111] R Naik, JJ Nazarko, CS Flattery, UD Venkateswaran, VM Naik, MS Mohammed, GW Auner, JV Mantese, NW Schubring, AL Micheli, and AB Catalan. Temperature dependence of the Raman spectra of polycrystalline $Ba_{1-x}Si_xTiO_3$. *Physical Review B*, 61(17):11367, 2000.

[112] Bog G. Kim, J.Y. Jo, and S.W. Cheong. Hybrid functional calculation of electronic and phonon structure of $BaSnO_3$. *Journal of Solid State Chemistry*, 197:134–138, January 2013.

[113] Ashok Kumar, I. Rivera, and R. S. Katiyar. Investigation of local structure of lead-free relaxor $BaTi_{0.70}Sn_{0.30}O_3$ by Raman spectroscopy. *Journal of Raman Spectroscopy*, 40(4):459–462, 2009.

[114] R Farhi, M El Marssi, A Simon, and J Ravez. A raman and dielectric study of ferroelectric ceramics. *The European Physical Journal B-Condensed Matter and Complex Systems*, 9(4):599–604, 1999.

[115] Tanmoy Maiti, R Guo, and AS Bhalla. Evaluation of experimental resume of $BaZr_xTi_{1-x}O_3$ with perspective to ferroelectric relaxor family: An overview. *Ferroelectrics*, 425(1):4–26, 2011.

[116] Fernando Rubio-Marcos, Adolfo Del Campo, Pascal Marchet, and Jose F Fernández. Ferroelectric domain wall motion induced by polarized light. *Nature communications*, 6, 2015.

[117] AG Razumnaya, Yu I Yuzyuk, IN Zakharchenko, Yu A Tikhonov, N Ortega, A Kumar, RS Katiyar, M El Marssi, and IA Lukyanchuk. Phase transition in ferroelectric $BaTiO_3/SrTiO_3$ superlattice: Raman spectroscopy studies. *Ferroelectrics*, 501(1):61–69, 2016.

[118] Dmitry Nuzhnyy, Přemysl Vaněk, Jan Petzelt, Viktor Bovtun, Martin Kempa, Ivan Gregora, Maxim Savinov, Radmila Krupková, Václav Studnicka, Josef Bursík, Mihail Samoylovich, and Wilfried Schranz. Properties of $BaTiO_3$ confined in nanoporous Vycor and artificial opal silica. *Processing and Application of Ceramics*, 4(3):215–223, 2010.

[119] Shuangyi Liu, Limin Huang, Jackie Li, and Stephen Obrien. Intrinsic dielectric frequency dependent spectrum of a single domain tetragonal $BaTiO_3$. *Journal of Applied Physics*, 112(1), 2012.

[120] Ph. Ghosez, J.-P. Michenaud, and X. Gonze. Dynamical atomic charges: The case of ABO_3 compounds. *Physical Review B*, 58(10):6224–6240, September 1998.

[121] Francois Jollet, Claudine Noguera, Martine Gautier, Nathalie Thromat, and Jean-Paul Duraud. Influence of oxygen vacancies on the electronic structure of yttrium oxide. *Journal of the American Ceramic Society*, 74(2):358–364, February 1991.

[122] Johannes Frantti, Y Fujioka, A Puretzky, Y Xie, Z-G Ye, and AM Glazer. A statistical model approximation for perovskite solid-solutions: A raman study of lead-zirconate-titanate single crystal. *Journal of Applied Physics*, 113(17):174104, 2013.

[123] Wen-Ku Chang, Shy-Feng Hsieh, Yuan-Haun Lee, Kuan-Neng Chen, Nan-Chung Wu, and A A Wang. X-ray diffraction studies of phase transformations between tetragonal and cubic phases in the $BaSn_xTi_{1-x}O_3$ system. *Journal of materials science*, 33(7):1765–1768, 1998.

[124] Andrzej Koleżyński and Katarzyna Tkacz-Śmiech. From the molecular picture to the band structure of cubic and tetragonal barium titanate. *Ferroelectrics*, 314(1):123–134, 2005.

[125] S. Sallis, D. O. Scanlon, S. C. Chae, N. F. Quackenbush, D. A. Fischer, J. C. Woicik, J. H. Guo, S. W. Cheong, and L. F J Piper. La-doped $BaSnO_3$ - Degenerate perovskite transparent conducting oxide: Evidence from synchrotron x-ray spectroscopy. *Applied Physics Letters*, 103(4):1–5, 2013.

[126] Joseph W Bennett, Ilya Grinberg, and Andrew M Rappe. Effect of symmetry lowering on the dielectric response of $BaZrO_3$. *Physical Review B*, 73(18):180102, 2006.

Annex

Annex A

UV-visible spectroscopy

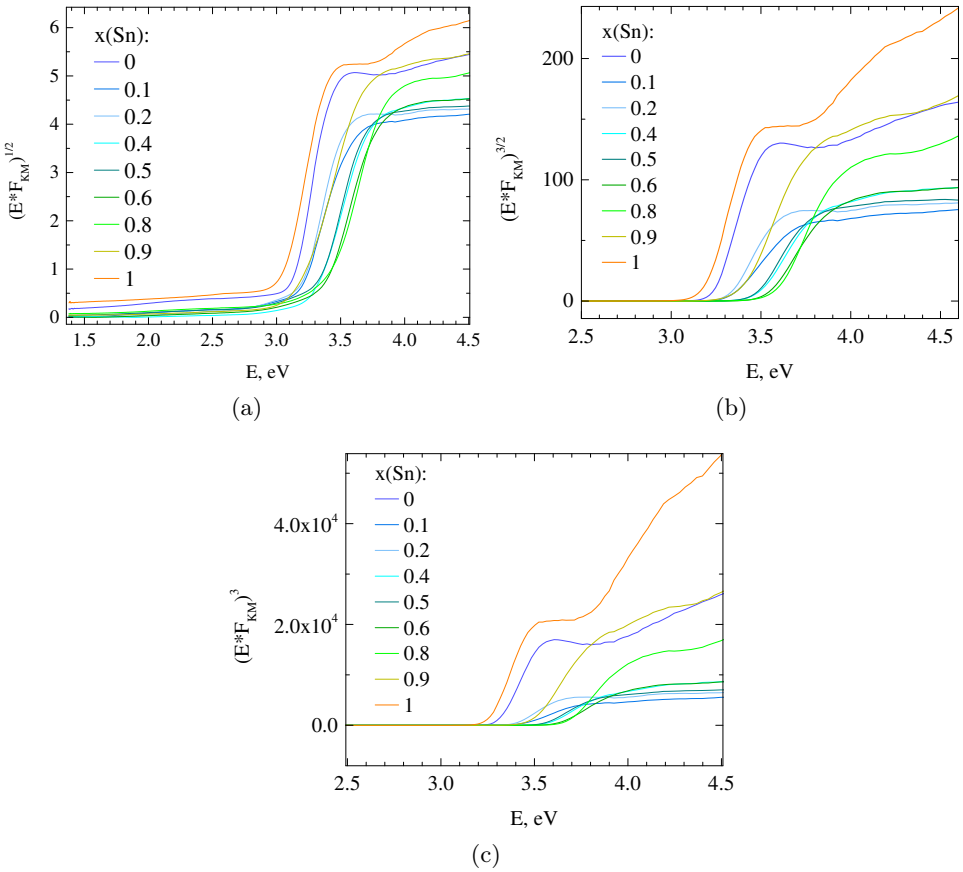

Figure A1: The Tauc plot under different assumptions of its origin: (a) allowed indirect band gap; (b) forbidden direct band gap; (c) forbidden indirect band gap

Annex B

Raman spectra recorded in temperature for certain compositions

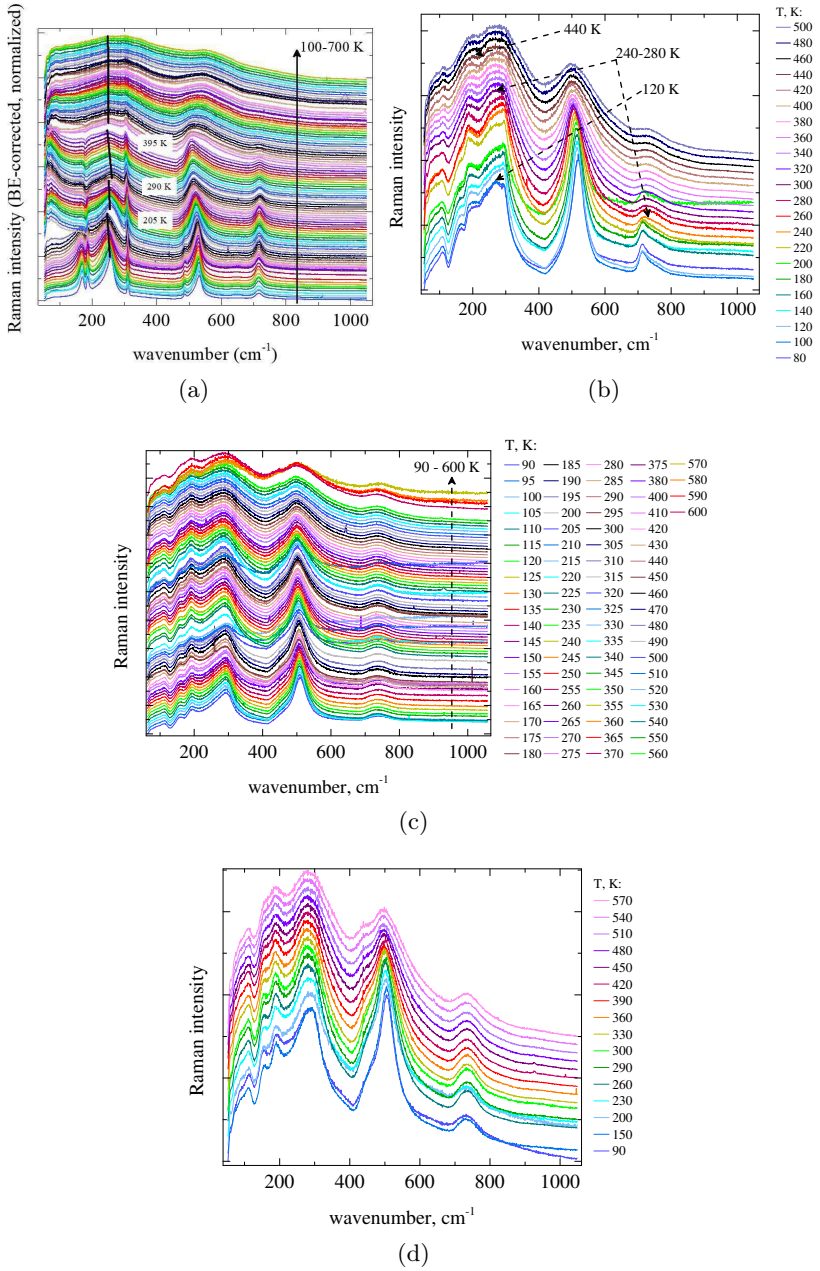

Figure B1: Raman spectra recorder in temperature for compositions x(Sn): (a) 0; (b) 0.2, (c) 0.4, (d) 0.5

Annex C

Full view of XPS spectra of different compositions

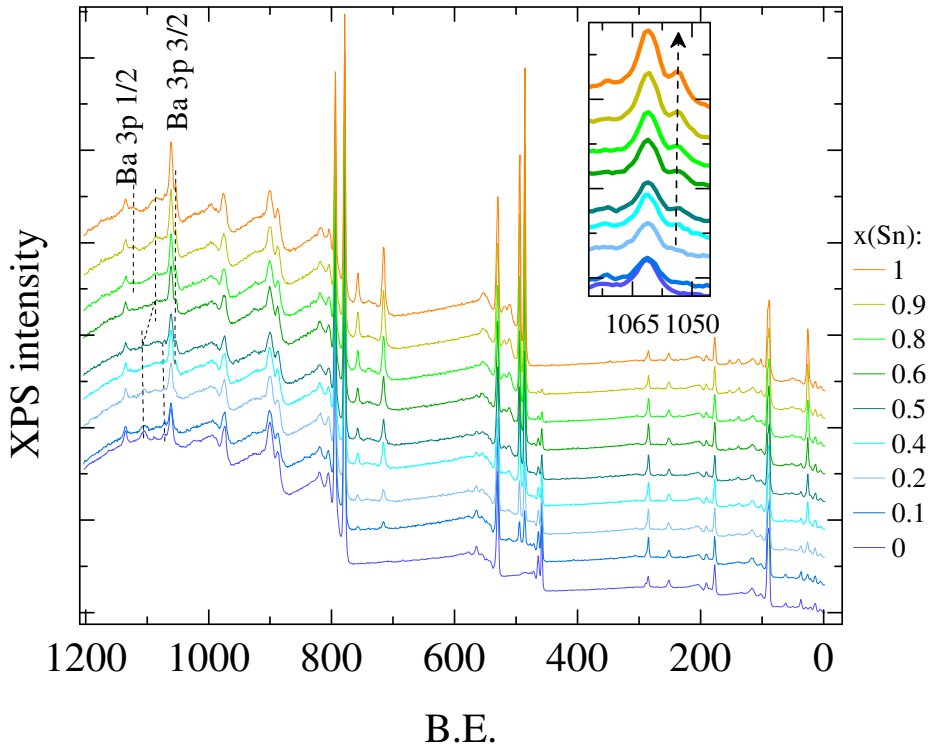

Figure C1: XPS survey spectra (inset: zoom of Ba 3p 3/2 peak)

Annex D

Le Bail profile fit of XRD data

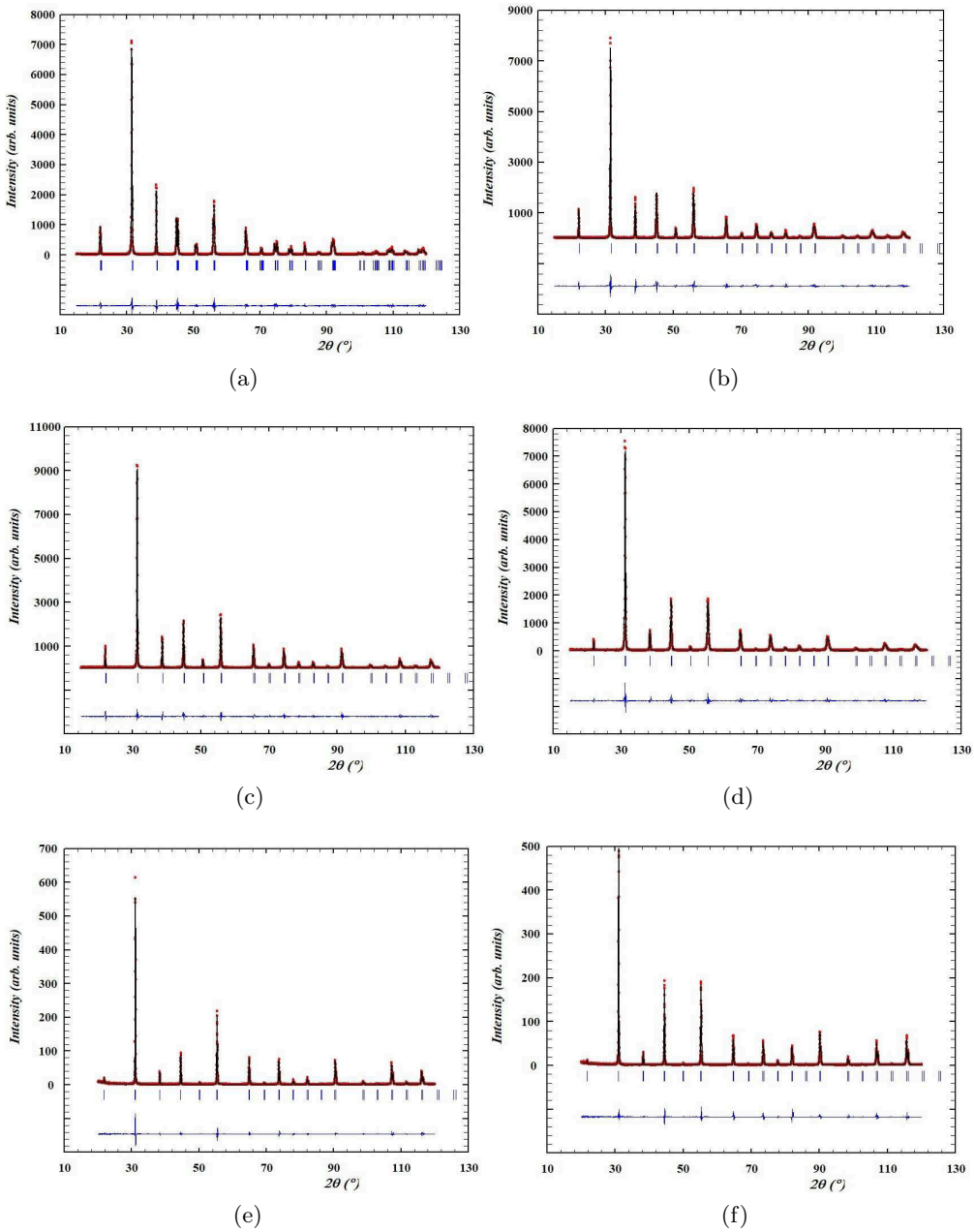

Figure D1: Fitted patterns for composition x(Sn): (a) 0; (b) 0.1; (c) 0.2; (d) 0.4; (e) 0.5; (f) 0.6;

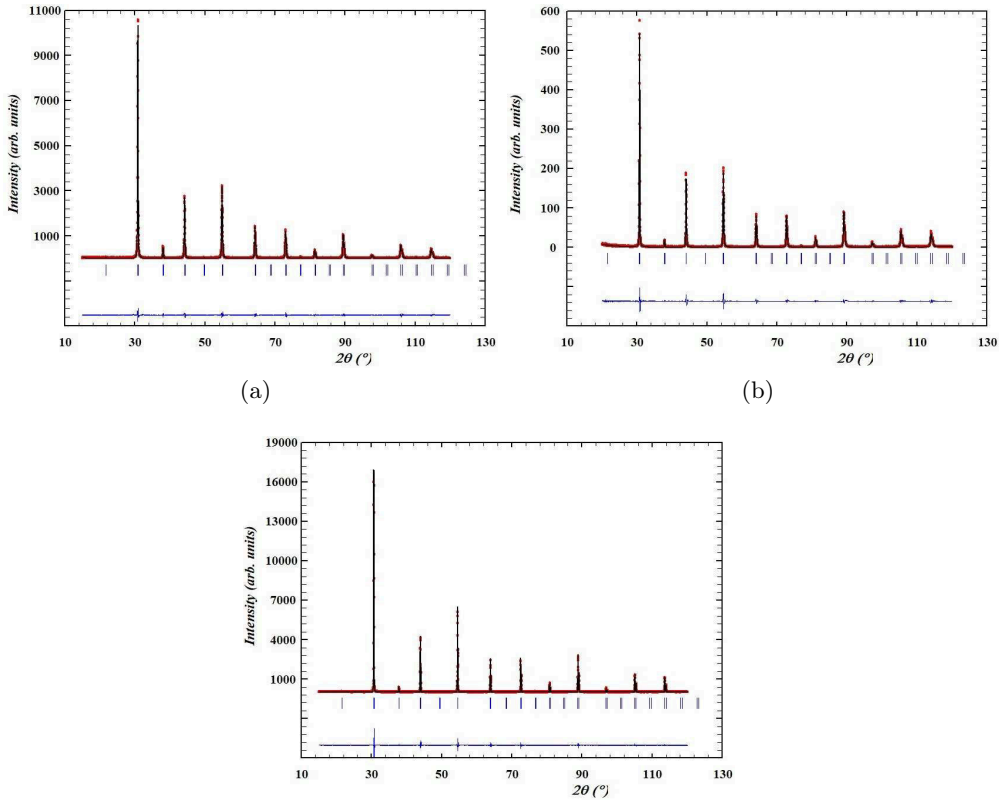

Figure D2: Fitted patterns for composition x(Sn): (a) 0.8; (b) 0.9; (c) 1

Table D1: Errors of the profile Le Bail fit for different compositions

x(Sn)	Space group	a, Å	c, Å	Rwp	GOF
0	$P4mm$	3.9965	4.0325	15.99	1.4
0.1	$Pm\bar{3}m$	4.0179	4.0179	17.56	1.5
0.2	$Pm\bar{3}m$	4.0285	4.0285	16.84	1.47
0.4	$Pm\bar{3}m$	4.0502	4.0502	16.06	1.37
0.5	$Pm\bar{3}m$	4.0587	4.0587	12.38	1.5
0.6	$Pm\bar{3}m$	4.0693	4.0693	14.62	1.88
0.8	$Pm\bar{3}m$	4.0932	4.0932	13.61	1.22
0.9	$Pm\bar{3}m$	4.1056	4.1056	11.54	1.54
1	$Pm\bar{3}m$	4.1158	4.1158	16.72	1.38

Résumé complet de thèse

Les études des solutions solides de structure pérovskite permettent d'établir une connexion entre leur structure macroscopique et l'ordre polaire qui influence les liaisons chimiques, et les propriétés optiques. Les propriétés (photovoltaïques, piézoélectriques, diélectriques, électrocaloriques etc.) sont souvent non-linéaires et peuvent permettre de nouvelles fonctionnalités. Dans notre travail, nous nous sommes concentrés sur la solution solide $BaSn_xTi_{1-x}O_3$ entre les composés chimiques purs $BaTiO_3$ (ferroélectrique) et $BaSnO_3$ (paraélectrique). Les valences similaires de Ti et de Sn (+4) doivent assurer l'absence de grandes concentrations de défauts. La présence de Sn peut contribuer à la meilleure mobilité des charges par la présence des niveaux électroniques Sn 5s 5p dans la bande de conduction.

Le diagramme de phases de $BaSn_xTi_{1-x}O_3$ contient des compositions très différentes du point de vue de l'ordre polaire. En première approximation, à partir des études détaillées pour $0<x(Sn)<0,3$ il y a les ferroélectriques, où les dipôles électriques sont ordonnés et les phases relaxeurs où il y rupture de l'ordre polaire. Nous avons également étendu l'étude des propriétés au-delà de la composition $x(Sn)=0,3$.

Le premier chapitre décrit les études de la structure cristallographique par diffraction des rayons X ainsi que de l'ordre polaire par spectroscopie diélectrique. Puis, nous avons analysé une structure atomique ($x=0,4$) et les distorsions locales de la phase relaxeur en utilisant la Microscopie Électronique en Transmission (MET). Bien que le volume de la maille unitaire évolue linéairement avec la composition, nous avons pu préciser quelle était la séquence de phases :

- ferroélectrique ($x(Sn)=0...0,1$)
- les compositions présentant une transition diffuse où l'ordre ferroélectrique et desordre coexistent, avec une maille pseudo-cubique ($x(Sn)=0,1...0,3$)
- les relaxeurs avec une maille pseudo-cubique qui incluent des clusters nanoscopiques avec les distorsions polaires ($x(Sn)>=0,3$).

Les propriétés diélectriques des compositions riches en Ti viennent des dipôles d'origine ferroélectrique. Par contre, pour les compositions riches en Sn, les dipôles de défauts peuvent jouer un rôle important.

La MET montre que les clusters polaires nanométriques des phases relaxeur x(Sn)=0,4 ont une taille plus petite que dans les compositions présentant une transition diffuse, mais les valeurs des déplacements des Ti/Sn est plus grande. On observe des distorsions complexes avec une composante rhomboédrique selon <111>.

Le deuxième chapitre présente les mesures d'absorption optique à température ambiante et en température, pour des compositions choisies, afin de relier les propriétés optiques à l'ordre polaire.

La bande interdite montre une variation non-linéaire en fonction de la composition. Elle croît d'une valeur ∼0.35 eV jusqu'à x(Sn)=0,8 et diminue pour les autres compositions. À partir de nos données, la bande interdite est définie par les états élargis où les composantes individuelles Sn ou Ti ne sont pas séparables, nous amenant à supposer une hybridation.

On trouve la connexion entre la valeur de bande interdite et le type de désordre sur x(Sn) pour les échantillons à température ambiante et en température. La bande interdite change d'une façon continue dans les limites d'une phase, puis elle diminue d'une façon non-linéaire avec l'augmentation de température près de la transition de phase, avant de reprendre une évolution linéaire. De plus, la pente de $Eg(T)$ change entre la phase avec les corrélations polaires statiques et la phase où elles sont absentes. La largeur de la queue d'absorption exponentielles (dites queue d'Urbach) est couplée au type de désordre polaire mais, pour les compositions riches en Sn, le désordre est défini par l'activation des défauts.

En raison de l'importance du désordre local pour les propriétés optiques, dans le dernier chapitre de ce manuscrit la structure locale et le désordre sont analysés en connexion avec la liaison chimique. Nous nous sommes concentrés sur la transition de phase et la spectroscopie Raman a été employée pour discerner les types différents de distorsions et les caractériser qualitativement. Cette étude, couplée avec les résultats des méthodes utilisées dans les chapitres précédents, nous a permis de redéfinir la séquence de phases à température ambiante :

- structures de type ferroélectrique 0<x(Sn)≤0,1
- x(Sn)=0,2 est la seule composition de notre étude présentant une transition diffuse amenant à une coexistence de phase. Une composante ferroélectrique est plus importante que la phase relaxeur selon les mesures diélectriques. La distorsion est très faible, comme x(Sn)=0.2 est juste au-dessous de T_{CW} où la composante de polarisation macroscopique disparaît. La distorsion est orthorhombique avec une faible composante rhomboédrique.

- x(Sn)=0,4 – relaxeur avec des distorsions identique à x(Sn)=0,2
- 0,5<x(Sn)<0,75 relaxeur avec les distorsions orthorhombique et rhomboédrique, la dernière augmentant avec la composition.
- 0,75<x(Sn)≤0,9 les clusters qui contiennent les atomes de Ti dans la matrice $BaSnO_3$ cubique. Les distorsions préservent les caractéristiques identiques à celle juste avant la limite de percolation d'atomes Ti (O + R), probablement parce que les contraintes chimiques dans les clusters ne changent pas.

Dans les études en température Eg=f(T), la bande interdite réagit à tout changement de phase où la symétrie est modifiée (e.g. rhomboédrique - orthorhombique, comme pour x(Sn)=0.2 dans la zone de transition diffuse) et pas au désordre. Le mécanisme de la variation de la zone interdite est le couplage avec les phonons de type Axe, qui sont détectés en Raman, qui modifient une degré de superposition des orbitales d'oxygène et des atomes B de la structure-type ABO_3. Ces orbitales forment la liaison chimique π, qui détermine l'énergie minimale de la bande de conduction. Le dégrée de superposition modifie aussi la distribution des charges électroniques effectives des atomes. On peut analyser ces charges qualitativement avec la Spectrométrie de photo-électrons X. Dans une maille distordue, l'angle de la liaison chimique O-B-O n'est pas exactement 180° et il y a croissance simultanée des charges électroniques des atomes O et B, ce qui est interdit dans le cas cubique parfait par le principe de Pauli. Cette tendance apparaît entre x(Sn)=0 et 0,8, puis le surplus de charge diminue pour x(Sn)=0,8...1. Ceci apporte la preuve que l'augmentation de la bande interdite est causée par l'augmentation de la distorsion rhomboédrique, et la diminution qui suit est reliée à la disparition progressive des clusters polaires dans la matrice de $BaSnO_3$.

Proceedings

of the Third Seminar on

THE MECHANICS OF MULTIFUNCTIONAL MATERIALS

J. Schröder, D.C. Lupascu, H. Wende, D. Brands (Eds.)

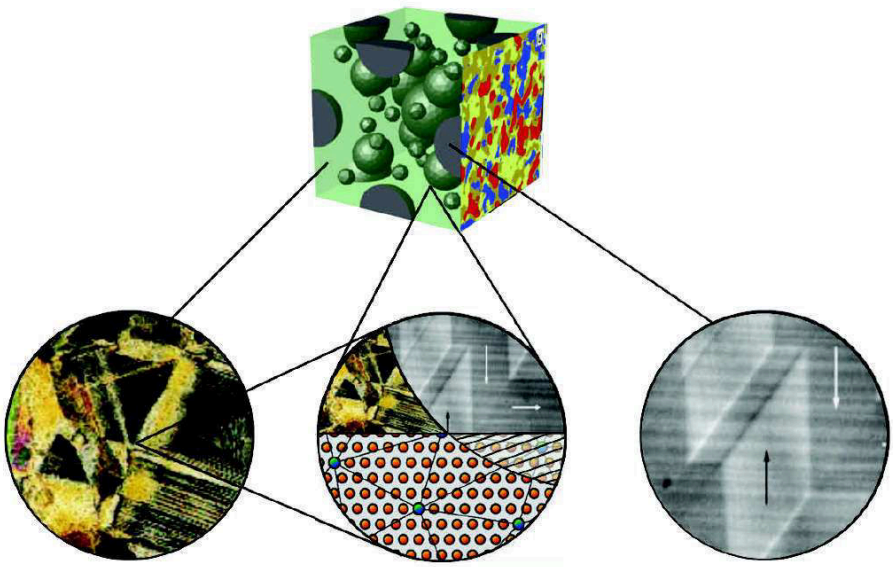

Physikzentrum Bad Honnef

June 11 - 15, 2018

Report No. 18
Institute of Mechanics
Department of Civil Engineering
Faculty of Engineering
University of Duisburg-Essen

OPTICAL AND ELECTRONIC PROPERTIES IN FERROELECTRIC BARIUM TITANATE-BASED COMPOUNDS

Halyna Volkova[1,*], Pascale Gemeiner[1], Grégory Geneste[2], Jêrome Guillot[3], Carlos Frontera[4], Nidal Banja[1], Fabienne Karolak[1], Christine Bogicevic[1], Brahim Dkhil[1], Nicolas Chauvin[5], Damien Lenoble[3], and Ingrid C. Infante[5]

[1] Laboratoire Structures, Propriétés et Modélisation des Solides, CentraleSupélec, CNRS-UMR8580, Université Paris-Saclay
8-10 rue Joliot-Curie, Gif-sur-Yvette, France

[2] CEA, DAM
DIF, Arpajon, France

[3] Luxembourg Institute of Science and Technology, Materials Research and Technology Department
41 rue du Brill, Belvaux, Luxembourg

[4] Institut de Ciència de Materials de Barcelona, Consejo Superior de Investigaciones Científicas
Campus de la UAB, Bellaterra, Spain

[5] Institut de Nanotechnologies de Lyon, CNRS-UMR5270 ECL INSA UCBL CPE, Université de Lyon
7 avenue Jean Capelle, Villeurbanne, France

Abstract. *The bandgap energy values for the ferroelectric $BaTiO_3$-based solid solutions with isovalent substitution Ba_{1-x} Sr_xTiO_3, $BaZr_xTi_{1-x}O_3$ and $BaSn_xTi_{1-x}O_3$ were determined using diffuse reflectance spectra. While the corresponding unit cell volume follows Vegard's law in accordance with the different ionic radii of the ionic substitutions, the bandgap values depict non-linear compositional dependences for all the solid solutions. The effect is considerably large for $BaZr_xTi_{1-x}O_3$ and $BaSn_xTi_{1-x}O_3$ solutions, depicting a bandgap linear compositional dependence up to $x=0.6$, for $x>0.6$ $BaZr_xTi_{1-x}O_3$ compounds present much larger bandgap values than $BaSn_xTi_{1-x}O_3$ counterparts. Electronic properties have been investigated through X-ray photoelectron spectroscopy in $BaSn_xTi_{1-x}O_3$ compounds, indicating that the Sn 3d and Ti 2p core levels shift against the Ba 3d ones within the whole compositional range with the same energy trend as that observed for the optical bandgap. Since for Ba_{1-x} Sr_xTiO_3 compounds no major bandgap variation is observed, we conclude that the bandgap compositional dependences observed for $BaSn_xTi_{1-x}O_3$ compounds and $BaZr_xTi_{1-x}O_3$ ones are originated from the structural sensitivity of the O, Ti and Sn or Zr electronic bands involved in the bandgap transition of these compounds. With this work, we underline the reliability of the bandgap determined from diffuse reflectance spectrometry experiments, as a means to non-invasively evaluate the electronic properties of powder materials.*

1 Introduction

Since the theoretical efficiency limit of single p-n junction solar cell was calculated by Shockley and Queisser [1], there is a challenge of finding new ways to bypass it. A way to intrinsically increase the efficiency could be to use alternative materials such as ferroelectrics (FEs). Unlike p-n junctions, the potential difference in ferroelectrics arises from their non-centrosymmetric unit cell providing the so-called bulk photovoltaic effect [2]. Among them, $BaTiO_3$ is a well-referenced, relatively cheap to produce, and environmentally friendly FE. In view of finding new ways to obtain FE-control of the optical properties, $BaTiO_3$-solid solutions have been studied, as potentially depicting FE-order with simultaneously enhanced photoconductive properties. Here we present the work on three solid solutions with isovalent substitutions, in view of understanding the pure structural and electronic

*Corresponding author: H. Volkova (halyna.volkova@centralesupelec.fr)

effects and minimizing the point defect contributions. With Sr^{2+} substituting Ba^{2+}, the $Ba_{1-x}Sr_xTiO_3$ is a family of solid solutions with ferroelectricity remaining at low temperature up to x_Sr~0.9 [3]. $BaZr_xTi_{1-x}O_3$ and $BaSn_xTi_{1-x}O_3$ are solid solutions with Ti^{4+} being substituted by Zr^{4+} and Sn^{4+}, respectively, thus presenting conduction band where Zr 4d and Sn 5s 5p states will be added to Ti 3d ones, which in principle will depict much different effective mass and mobility, for the potential photoconduction properties that we are seeking. The phase diagrams of $BaZr_xTi_{1-x}O_3$ [4] and $BaSn_xTi_{1-x}O_3$ [5] display rich polar features, evolving at room temperature from a pure tetragonal FE in the Ti-rich region towards a paraelectric cubic structure in the Ti-poor region. In-between, the compositions are FE-relaxors characterized by polar disorder and average cubic structure.

2 Experimental procedures

$Ba_{1-x}Sr_xTiO_3$ (x_Sr = 0, 0.25, 0.5, 1), $BaZr_xTi_{1-x}O_3$ (x_Zr = 0, 0.1, 0.2, 0.3, 0.4, 0.5, 0.6, 0.7, 0.8, 0.9, 1) and $BaSn_xTi_{1-x}O_3$ (x_Sn = 0, 0.1, 0.2, 0.4, 0.5, 0.6, 0.8, 0.9, 1) samples were synthesized by solid state reaction from starting materials, $BaCO_3$ (99.9%), $SrCO_3$ (99.9%), TiO_2 (99%), ZrO_2 (99.9%), and SnO_2 (99.9%). After homogenization in a mortar, by ultrasonic bath and by magnetic mixing, the powders were calcined at temperatures between 800°C and 1200°C, and subsequently ground with polyvinyl alcohol and pressed into pellets. Two annealing steps at 600°C and 800°C insured the evaporation of binding agent. The sintering was held at temperatures of 1280-1450°C adjusting the dwell times, resulting in pellet density of ~92-95%. Structural evaluation by X-ray diffraction (XRD) was performed using a Bruker D2 Phaser diffractometer on finely ground and annealed powders, with 0.02º step and acquisition times adjusted for different angular ranges (10 sec/step for 2θ=20-35°, 30 sec/step for 35-60°, 55 sec/step for 60-120°). Unit cell volume was determined using Le Bail analysis through devoted crystallographic software (Jana2006). The ultraviolet-visible-near-infrared spectrometry experiments were performed on a Perkin Elmer Lambda 850 spectrometer in diffuse reflectance geometry using a Harrick's Praying Mantis™ accessory, from finely grinded and annealed powders to minimize mechanical stresses. From the raw reflectance, *R*, the absorption coefficient *k* is determined according to Kubelka-Munk reemission function F_{KM} transformation [6], within the assumption the scattering coefficient *s* is independent of the photon energy:

$$F_{KM} = \frac{k}{s} = \frac{(1-R)^2}{2R}. \quad (1)$$

The optical bandgap is determined from a linear fit to the onset of the absorption edge obtained after converting the F_{KM} following Tauc formalism, which for the present study we consider as direct bandgap. X-ray photoelectron spectroscopy (XPS) studies were carried out on powder and ceramic samples. Axis Ultra DLD spectrometer with Al Kα X-ray source operated at 50W was used, together with charge neutralizer. For the analysis of the XPS data (CasaXPS), we have used the internal reference of the Ba $3d_{7/2}$ core level energy, fixed at 778.5eV, as considered to be the ion with very limited changes in its electronic state due to chemical, electronic and structural effects.

3 Results and Discussion

From the XRD collected (Figure 1a-c), we deduce the stabilization of a pure perovskite phase for each solid solution compound, with unit cell volume following Vegard's law (Figure 1d). The larger compositional slope for Zr-compounds than for Sn-ones is in agreement with the expected effect induced by the difference in ionic radius of Zr^{4+} against Sn^{4+}, depicting the Sr^{2+}-compounds a volume reduction, as expected [8].

Optical properties of the different compositions are shown in Figure 2a-d. Diffuse reflectance raw data in Figure 2a point out the large absorption differences of parent compounds. Optical absorption features are seen in the Kubelka-Munk functions F_{KM} depending of the solid solution. A large increase of F_{KM} is characteristic of the optical absorption edge at a given photon energy, being the

Zr-compounds (Figure 2c) those presenting the larger variation of the photon energy onset. No remarkable onset change is seen for Sr-compounds (Figure 2b), and weak and non-monotonic ones for Sn-compounds (Figure 2d). The chemical substitution effect on the occupied electronic states is directly investigated on Sn-based compounds through XPS core level acquisition. Using $Ba3d_{7/2}$ state as the perovskite energy reference, we plot in Figure 2e-k the different characteristic O1s, Sn3d and Ti2p occupied states. Fine analysis of these levels indicate a shift of the energy positions of Sn and Ti as a function of the Sn-content (Figure 2i and k).

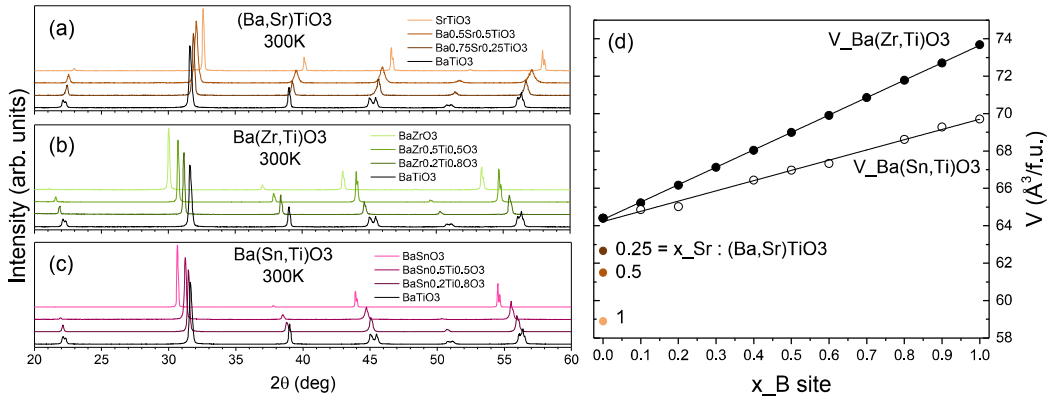

Figure 1: Room temperature X-ray diffraction [(a)-(c)] powder patterns and (d) unit cell volume determined from the XRD patterns, for different $BaTiO_3$-based compounds. [(a)-(c)]: (a) $Ba_{1-x}Sr_xTiO_3$ with x_Sr=0, 0.25, 0.5, 1 (bottom to top), (b) $BaZr_xTi_{1-x}O_3$ with x_Zr=0, 0.2, 0.5, 1 (bottom to top), and (c) $BaSn_xTi_{1-x}O_3$ with x_Sn=0, 0.2, 0.5, 1 (bottom to top); (d) Pseudocubic cell volume per formula unit as a function of x_B site (Zr or Sn) (symbols), corresponding linear fits are shown.

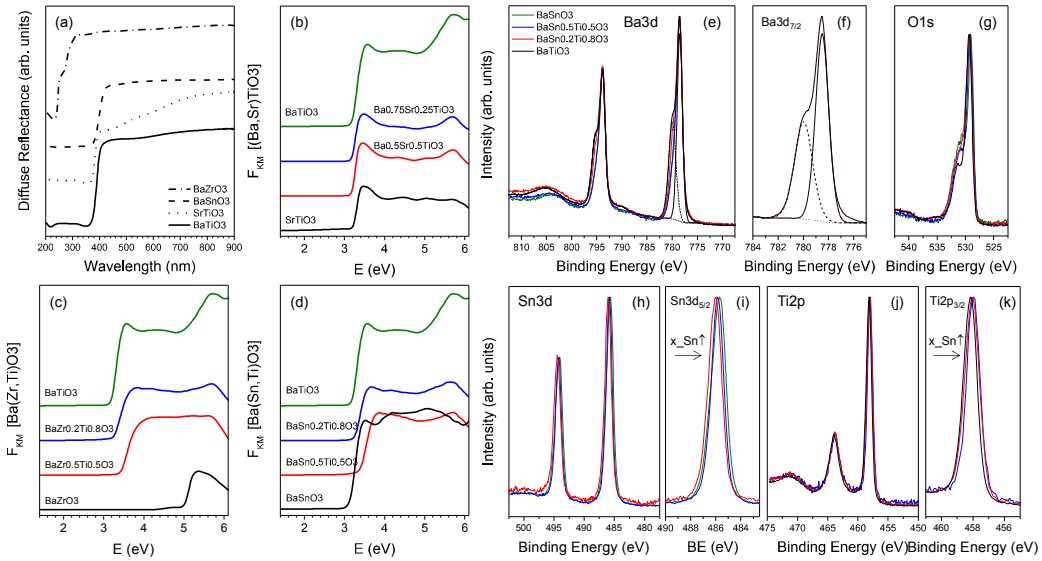

Figure 2: [(a)-(d)] Optical properties from $BaTiO_3$-solid solutions, and [(e)-(k)] X-ray photoelectron spectroscopy (XPS) core level data from $Ba(Sn,Ti)O_3$. [(a)-(d)]: (a) Diffuse reflectance spectra from parent compounds ($BaTiO_3$, $SrTiO_3$, $BaSnO_3$ and $BaZrO_3$, bottom to top), and [(b)-(d)] Kubelka-Munk F_{KM} functions *vs* photon energy E determined for (b) $Ba_{1-x}Sr_xTiO_3$ with x_Sr=0, 0.25, 0.5, 1 (top to bottom), (c) $BaZr_xTi_{1-x}O_3$ with x_Zr=0, 0.2, 0.5, 1 (top to bottom), and (d) $BaSn_xTi_{1-x}O_3$ with x_Sn=0, 0.2, 0.5, 1 (top to bottom). [(e)-(k)]: Core levels from $BaSn_xTi_{1-x}O_3$ compounds (x_Sn=0, 0.2, 0.5, 1) (a) Ba3d, (g) O1s, (h) Sn3d, (i) $Sn3d_{7/2}$, (j) Ti2p, (j) $Ti2p_{3/2}$, together with the example on $BaTiO_3$ sample of the different components used for $Ba3d_{5/2}$ fitting (Ba within $BaCO_3$, dash line, Ba within the perovskite -here, $BaTiO_3$- fill line, and background, dotted line).

Bandgap values as a function of Sn- or Zr- substitution (Figure 3a) account for the large differences previously noticed from direct analysis of the optical properties through F_{KM}. Remarkably, for x_B > 0.2, both solution compounds depict polar disorder, being relaxors at room temperature, follow the same initial trend up to x_B ~ 0.6. For x > 0.6, Zr-compounds present larger bandgap values while lower ones are determined for Sn-compounds. Comparing the obtained optical bandgap values for Sn-compounds with the energy differences of the XPS Ti2p and Sn3d electronic bands (Figure 3b-c), we notice a similar substitution dependence. Moreover, these XPS energy differences are fully in agreement with the observed bandgap variation, being for optical and XPS results this energy difference of ~ 0.35eV between $BaTiO_3$ and x_Sn = 0.8. Investigations are ongoing to determine the precise origin of this behavior and its coupling to the relaxor properties.

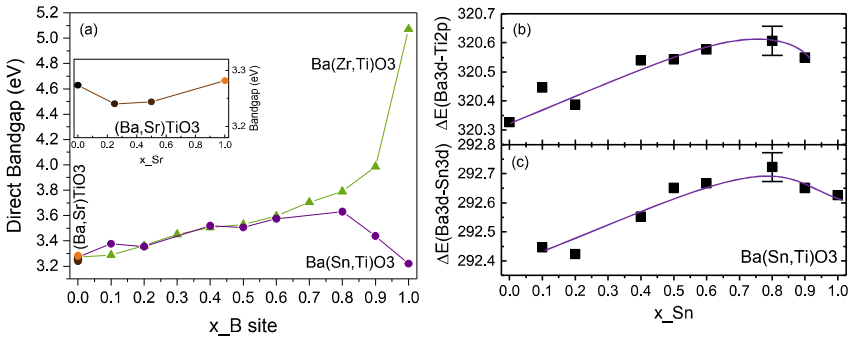

Figure 3: (a) Bandgap values as a function of the x_B site substitution for different $BaTiO_3$-solid solutions, determined using F_{KM} and Tauc plot linear fits, assuming direct bandgap. Inset: Bandgap for the $Ba_{1-x}Sr_xTiO_3$ compounds *vs* x_Sr substitution. [(b),(c)]: B-site core level energy difference (ΔE) relative to the perovskite $Ba3d_{7/2}$ core level position for different $BaSn_xTi_{1-x}O_3$ compounds and as a function of the x_Sn substitution, being (b) $Ti2p_{5/2}$ and (c) $Sn3d_{7/2}$ (lines are a guide for the eye).

4 Conclusions

Combining structural, optical and electronic characterization tools on pure perovskite $Ba_{1-x}Sr_xTiO_3$, $BaZr_xTi_{1-x}O_3$ and $BaSn_xTi_{1-x}O_3$ solid solutions, we proved that we can precisely determine their bandgap values. We have successfully presented the potential of diffuse reflectance spectrometry for the determination of the optical and electronic properties of single phase perovskite oxides, and similar approaches can be exploited for investigating the optical transitions of other materials.

REFERENCES

[1] W. Shockley and H. J. Queisser. Detailed Balance Limit of Efficiency of p-n Junction Solar Cells, *Journal of Applied Physics*, 32, 510. 1961.

[2] A. M. Glass et al. High-voltage bulk photovoltaic effect and the photorefractive process in $LiNbO_3$, *Applied Physics Letters*, 25, 233. 1974.

[3] C. Ménoret et al. Structural evolution and polar order in $Sr_{1-x}Ba_xTiO_3$, *Physical Review B*, 65, 224104. 2002.

[4] T. Maiti, R.Guo and A. S. Bhalla. Structure-Property Phase Diagram of $BaZr_xTi_{1-x}O_3$ System, *Journal of the American Ceramics Society*, 91, 1769. 2008.

[5] X. Wei and X. Yao. Preparation, structure and dielectric property of barium stannate titanate ceramics, *Materials Science and Engineering: B*, 137, 184. 2007.

[6] B. Philips-Invernizzi, D. Dupont and C. Cazé. Bibliographical review for reflectance of diffusing media, *Optical engineering*, 40, 1082. 2001.

[7] J. Tauc, R. Grigorovici, and A. Vancu. Optical Properties and Electronic Structure of Ge, *Physica Status Solidi*, 15, 627. 1966.

[8] R. D. Shannon. Revised Effective Ionic Radii and Systematic Studies of Interatomic Distances in Halides and Chaleogenides, *Acta Crystallographica*, A32, 751. 1976.